

Bi-directional AC-DC Matrix Converter with Unity Power Factor for Electric Vehicle Chargers

by

Saeeda Sana

A Thesis Submitted in Partial Fulfillment
of the Requirements for the Degree of

Master of Applied Science

in

The Faculty of Engineering and Applied Sciences

Electrical and Computer Engineering

University of Ontario Institute of Technology

January, 2016

© Saeeda Sana, 2016

Abstract

Automobile industries are striving to meet growing demands of producing electric vehicles for a sustainable environment. Rising number of EVs pose many challenges including increased number of charging stations to meet the needs of EVs. EV chargers are recognized to impact the power quality of the grid when used in large quantities. This challenge is addressed in this thesis work to reduce the impact on the grid.

First, this thesis reviews two rectifier configurations under steady state, dynamic state and fault conditions. Implementation of IGBT rectifier using SPWM with a feedback controller and a matrix converter rectifier using SV-PWM modulation are carried out in MATLAB Simulink.

Second, the matrix converter when used with reduced switch count to be used in a rectifier configuration, the simulation results show that a unity power factor and bi-directional power flow are achievable without sophisticated controls and can benefit in V2G operation.

Keywords: *Electric vehicles, EV, Electric vehicle chargers, Matrix Converter, AC DC Matrix converter, Unity power factor, vehicle to grid, V2G, three phase rectifier, AC-DC Converter, 3x1 Matrix Converter, Space vector modulation, SVPWM, SPWM, Regenerative operation, bi-directional switch, power converters, power quality, THD.*

Acknowledgments

Most importantly, I would like to thank Allah (SWT), without His blessings and guidance I would have never completed this research work.

I would like to take this opportunity to thank my supervisor DR. Vijay. K. Sood for all his suggestions, patience and continuous support. I feel honored to have the opportunity of working with him and gaining crucial knowledge throughout the course of the degree.

I cannot possibly submit this thesis without thanking my parents who have always been there as a constant support in every way, never ceasing to believe in my capabilities. I would like to extend my gratitude towards my best friend and colleague Saadia Gauhar, for being there as a constant anchor.

Lastly, this thesis is a dedication to my dearest mother, Surriya Begum, who continues to be with me in my heart, providing constant spiritual support. I love you!

Table of Contents

Abstract	i
Acknowledgments	ii
Nomenclature	v
List of Figures	vi
List of Tables	viii
Chapter 1 General Background and Research Objectives	1
1.1 Background	1
1.2 Literature Review	3
1.3 Research Scope and Objectives	12
1.4 Thesis Outline	14
Chapter 2 EV Chargers and Power Converters	15
2.1 Introduction	15
2.2 System Description	15
2.3 Uncontrolled Diode Rectifiers	17
2.4 Partially Controlled Thyristor Rectifiers	21
2.5 Fully Controlled Insulated-Gate Bipolar Transistor (IGBT) Rectifier	26
2.5.1 Sinusoidal Pulse Width Modulation (SPWM)	29
2.6 DC/DC Buck Converters.....	31
Chapter 3 Matrix Converter and Control Schemes	35
3.1 Introduction	35
3.2 Matrix Converter	36
3.3 Controlled Single-Ended AC/DC Rectifier using Matrix Converter	45
3.4 Space-Vector Pulse Width Modulation (SVPWM).....	49
3.4.1 Indirect SVM for Rectifier	50
Chapter 4 System Modelling	58
4.1 Three-Phase IGBT Rectifier System Modelling.....	58
4.2 Three-Phase AC-DC Matrix Converter System Modelling	64

Chapter 5 Simulation Results and Analysis	70
5.1 Introduction	70
5.2 Steady State Analysis.....	70
5.2.1 Three-Phase IGBT Rectifier	71
5.2.2 Three-Phase Matrix Converter	74
5.3 Dynamic Analysis	77
5.3.1 Three-Phase IGBT Rectifier	77
5.3.2 Three-Phase Matrix Converter	82
5.4 Harmonic Analysis.....	87
Chapter 6 Fault Analysis	90
6.1 Introduction	90
6.2 Three-Phase IGBT Rectifier	91
6.2.1 Single-Line-to-Ground Fault	91
6.2.2 Double-Line-to-Ground Fault.....	94
6.2.3 Triple-Line-to-Ground Fault	96
6.3 Three-Phase AC-DC Matrix Converter	99
6.3.1 Single-Line-to-Ground Fault	99
6.3.2 Double-Line-to-Ground Fault.....	102
6.3.3 Triple-Line-to-Ground Fault	105
Chapter 7 Conclusion and Future Work.....	108
7.1 Conclusion	108
7.2 Future Work	112
References	114
Appendix A.....	118
Appendix B.....	119
B.1 Per-Unit System Calculation	119
B.2 Battery Model	120

Nomenclature

EV	Electric Vehicle
PQ	Power Quality
AC	Alternating Current
DC	Direct current
PF	Power Factor
IGBT	Insulated Gate Bipolar Transistor
MOSFET	Metal Oxide Field Effect Transistor
P	Active power
Q	Reactive power
PWM	Pulse Width Modulation
V2G	Vehicle-to-Grid
MC	Matrix Converter
HEV	Hybrid Electric Vehicle
ICE	Internal Combustion Engine
PHEV	Plug-in Hybrid Electric Vehicle
THD	Total Harmonic Distortion
SPWM	Sinusoidal Pulse Width Modulation
SVPWM	Space Vector Pulse Width Modulation
DMC	Direct Matrix Converter
IMC	Indirect Matrix Converter
PI	Proportional Integral
SLG	Single Line to Ground
DLG	Double Line to Ground
TLG	Triple Line to Ground
PFC	Power Factor Correction
RMS	Root Mean Square
RC	Resistor-Capacitor
PID	Proportional Integral Derivative
pu	Per unit
P	Active Power
Q	Reactive Power
V_{dc}	DC Voltage
I_{dc}	DC Current
P_{dc}	DC Power

List of Figures

Figure 1.1: Transportation model for sustainability [4].....	4
Figure 1.2: Three phase system topology of DC Charger of an EV [12].....	8
Figure 2.1: Single line system block diagram [30]	16
Figure 2.2: Three-phase diode bridge rectifier [32].....	18
Figure 2.3: Three-phase partially controlled thyristor rectifier [34].	21
Figure 2.4: Three-phase thyristor Converter Waveforms [12].	23
Figure 2.5: Voltage source rectifier operation [35]	27
Figure 2.6: Resultant PWM with varying <i>V_{MOD}</i> [35].....	27
Figure 2.7: Voltage controlled PWM voltage source rectifier for unity PF [35].	28
Figure 2.8: SPWM method [35].	30
Figure 2.9: Buck Converter [12]	32
Figure 2.10: Inductor current always positive	32
Figure 3.1: Three phase MC simplified structure [45]	37
Figure 3.2: 3-phase AC-AC matrix converter architecture [26]	41
Figure 3.3: Matrix converter maximal available input voltage [26].	41
Figure 3.4: Output voltage reduction waveform [26].....	42
Figure 3.5: Operation of MC as a rectifier [27].	45
Figure 3.6: Bi-directional AC-DC matrix converter with one DC output [27].	48
Figure 3.7: Space vector diagram for rectifier current with sectors [45].	51
Figure 3.8: Depiction of the converter states [28].....	54
Figure 3.9: Reference current vector	54
Figure 3.10: Basic Switching Sequence Principle	56
Figure 4.1: IGBT Rectifier Model	59
Figure 4.2: SPWM Generator.	60
Figure 4.3: Decoupled control of active and reactive power.	62
Figure 4.4: Three-Phase IGBT Rectifier System Model.	63
Figure 4.5: Matrix Converter Rectifier Block	64
Figure 5.1 (a-e): Steady state response of the system at the AC side with three phase IGBT rectifier.	72
Figure 5.2 (a-c): Steady state response of the system at the DC side with three phase IGBT rectifier.	73
Figure 5.3 (a-f): Steady state response of the system at the AC side with three phase MC rectifier.....	74
Figure 5.4 (a-c): Steady state response of the system at the DC side with three phase MC rectifier.....	75
Figure 5.5 (a-c): Bi-directional power flow response of the system with three-phase MC based rectifier.	76
Figure 5.6 (a-f): System response to a step change applied to DC output voltage.	78

Figure 5.7 (a-f): System response to a step change applied to the DC output Power.	80
Figure 5.8 (a-f): System response to a step change applied to the reactive power Q.	81
Figure 5.9 (a-d): System response to a step change applied to DC output voltage.	83
Figure 5.10 (a-d): System response to a step change applied to DC output current.	85
Figure 5.11 (a-f): V2G operation using MC based rectifier configuration.	87
Figure 5.12 (a) & (b): Harmonic spectrum of V_{sec} (Voltage at the secondary side of the transformer) & V_{dc} (Output DC voltage) for IGBT rectifier respectively.....	88
Figure 5.13 (a) & (b): Harmonic spectrum of V_{sec} (Voltage at the secondary side of the transformer) & V_{dc} (Output DC voltage) for MC rectifier respectively.....	89
Figure 6.1 (a-h): System response to SLG fault introduced for 6 cycles with IGBT based rectifier.....	93
Figure 6.2 (a-h): System response to DLG fault introduced for 6 cycles with IGBT based rectifier.....	95
Figure 6.3 (a-f): System response to TLG fault introduced for 6 cycles and 12 cycles with IGBT based rectifier.....	98
Figure 6.4 (a-h): System response to SLG fault introduced for 6 cycles with MC based rectifier.....	101
Figure 6.5 (a-h): System response to DLG fault introduced for 6 cycles with MC based rectifier.....	104
Figure 6.6 (a-h): System response to TLG fault introduced for 6 cycles and 12 cycles with MC based rectifier.....	107
Figure B.1: Equivalent circuit of a battery [61].....	120
Figure B.2: Typical charge characteristics of a Li-ion battery [61].....	122

List of Tables

Table 2.1: Current harmonics and THD variations with varying firing angle [34].	25
Table 3.1: Switching combination of three-phase to three-phase MC [45]	38
Table 3.2: Commutation combinations of the converter [28]	52
Table 3.3: Four-quadrant switches state combinations [28]	57
Table A: Parameters of the system model [30]	118

Chapter 1 General Background and Research Objectives

1.1 Background

In the future, fossil fuels will become scarce heavily impacting the automobiles that depend on them. Electric vehicles (EVs) are now starting to appear in our cities and are recognized as a solution to sustain a cleaner environment as well as reduce the dependence on finite fossil fuel resources. As EVs increase in number, more charging facilities would be required to assist with consumers growing demand for electric transportation. Utility companies have also realized the potential of EVs and the need for more charging stations. However, the future impact on the grid power quality (PQ) of using these charging stations on a larger scale has also been noted and measures are being taken for improving these charging systems to reduce the impact on the grid.

The system for EV chargers mainly comprises of three-phase AC-DC rectifiers, filters, buck converter and snubbers. Among these, an AC-DC rectifier stage is considered as the key part of the battery charger. Uncontrolled devices such as diodes are quite cheap and easily implemented but do not have any control over the output DC voltage and current. The result gives a distorted waveform, adding harmonics and poor power factor (PF) that adversely affects the PQ of the grid. Increased input filter size

could be used to achieve a smoother DC output at the expense of added bulk on the system and higher cost.

Partially controlled switches such as thyristors uses current and/or voltage control techniques to improve PF and PQ issues compared to diodes. However, these switches have limitations over the full range of control that can be achieved. For a complete control over the switch, fully controlled IGBTs or MOSFETs are implemented for use in AC-DC rectifiers. Various pulse-width-modulation (PWM) techniques and control strategies can be used for a complete control over the full range of current and voltage to improve PQ of the grid [7]. Furthermore, components of active power (P) and reactive power (Q) can be individually controlled to achieve a unity PF. This increases system complexity but that can be suited to meet specifications and the overall bulk of the passive components used in the system can be reduced with use of modulation techniques and control strategies.

The issues of PQ on the grid can also be improved with an add-on vehicle-to-grid (V2G) power transfer capability by using a new type of converter known as matrix converter (MC), which has recently been recognized as an all type converter depending on its configuration. MCs are more efficient offering a simpler design and reduced converter size with bi-directional power flow achieved by IGBT switches with back-to-back connection in their configuration. Space vector pulse width (SVPWM) modulation technique can be used for MC that offers many advantages like unity power factor and high quality DC output over other rectifier configurations.

1.2 Literature Review

Modern society is heavily dependent on automobiles that utilize fossil fuels for social and economic development. According to the US Department of Transportation, it is estimated that there are 800 million cars in the world out of which 250 million automobiles are on the road in the United States [1]. With rapid increase in globalization and industrialization, a further rise in automobile numbers on the road is inevitable. This brings a lot of issues related to automobiles burning finite resources like oil that adversely affects the environment due to carbon emissions.

There is a serious challenge with supply and demand of energy in the world today. Approximately 85 million barrels of oil is consumed in the world everyday but only 1300 billion barrels of proven oil reserves have been identified which will run out in about 42 years at the current rate of consumption [2]. Increase in global warming is another challenge scientists have been working on to lower the impact on the Earth's atmosphere. The rising level of CO₂ emissions from fossil fuels is leading to a global temperature rise which has long term consequences of rising sea levels and instability of ecosystems. In order to sustain a clean environment, vehicles using electricity and/or renewable resources are essential.

EVs use high efficiency electric motors and controllers producing a cleaner, efficient and more environmentally friendly transportation system [3]. Major issues with battery powered EVs are high cost, long charging times and limited driving range. Hybrid Electric Vehicle (HEVs) uses both internal combustion engine (ICE) and an electric motor

to drive the vehicle. They eliminate the issues of high cost and range of a pure EV.

Compared to HEVs, plug-in hybrid electric vehicles (PHEVs) comprises of larger motor size and battery pack [4].

Figure 1.1 depicts different types of energy sources, energy carrier and vehicle types. Conventional gas/diesel powered vehicles are dependent on oil that is produced from fossil fuels. HEVs are comparatively more efficient but rely mainly on fossil fuels as their main energy source for power. PHEVs have many advantages over conventional vehicles such that they reduce dependence on fossil fuels, emission levels are lower than regular hybrids and they provide convenience of re-charging directly from a standard wall outlet (e.g. homes). EVs and fuel cells vehicles depend on electricity and hydrogen respectively and like PHEV, they are the future for sustainability.

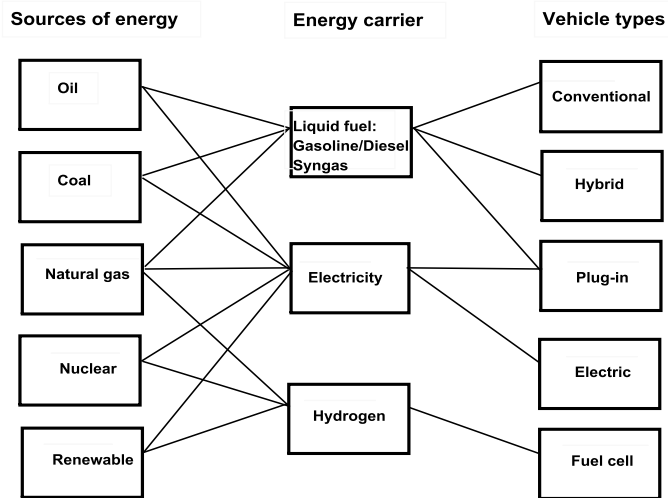


Figure 1.1: Transportation model for sustainability [4].

Invented in 1834, EVs were discovered 60 years prior to the invention of gasoline powered cars. The world's first HEV built in 1898 by Dr. Ferdinand Porche in Germany, used an ICE that powered the electric motors situated at the wheel hubs [5]. Using a gasoline engine to compensate for the power of an electric motor, another hybrid vehicle was developed in 1903 by Krieger Company and both these hybrids are similar to modern HEVs [6].

In the 1900s, Pieper - a Belgian car-maker introduced a 3.5 hp "voiturette" where a gasoline engine was merged with an electric motor under the seat that helped the car to perform as a generator when cruising and the engine to drive when the car was climbing a slope [4]. By 1930, both HEVs and EVs were slowly fading from the market and many reasons accounted for their failure:

- As large battery packs were needed, HEVs and EVs were more expensive than gasoline cars.
- They were less powerful compared to cars using fossil fuels owing to the limited power from the onboard battery.
- Both types of EVs required several hours to fully recharge the battery.
- Rural areas provided reserved accessibility to electricity for charging the HEVs and EVs.

As the gasoline price soared in 1973, research and development recommended using EVs to reduce oil dependency in 1976. Major automobile industries started developing

EVs and fuel cell vehicles during this period. Many EVs were produced including GM's EV1, Ford's Ranger pickup EV, Honda's EV Plus, Nissan's Altra EV and Toyota's RAV4 EV.

In 1997, world's first modern HEV, the Toyota Prius was sold in Japan; taking the EV technology to another level. Prius as well as Honda's Insight and Civic HEVs are available in the US since 2000 [4]. This radical change has continued to grow since the 2000s, where Tesla Roadster appeared as the first fully electric sports car available in the market. Tesla's second vehicle, Model S, which is a fully electric luxury sedan, has brought EVs right back in the market, helping to create a sustainable future [8].

PHEV's were previously designed keeping in mind the daily user feasibility requirements with small capacity batteries of around 5kWh that can be fully charged in 1h30m with 230V/16A outlet. The problem arises with increased charging times for the present range of EVs that relies completely on battery capacity. To resolve this issue, Nissan Leaf 2011 EV models integrated a 24 kWh battery and this concept was followed by many automobile manufacturers like Mitsubishi and Renault among others. Battery technology faces issues relating to power density, charging current, quantity of charging cycles and the overall cost.

At present, lithium-ion batteries in combination with a high power charger achieves 80% of maximum battery capacity of a vehicle similar to Nissan Leaf in about 30 minutes. Charging infrastructures need to be widely available until future advancements are made in the battery capacity sector of the EVs. SAE International J1772 committee

has recently shown new developments in the battery charging systems that can be divided with regards to different power levels and charging times [9].

EV chargers are generally divided into three types:

- **Level 1 EV Chargers** – Typical use of a 120 Volt AC outlet used in households. EVs come with an on-board equipment and the vehicle can be charged in the garage of the house or driveway. From a fully discharged battery to full capacity charge, this type of charger can be relatively slow in charging the battery to full capacity in about 10-20 hours.
- **Level 2 EV Chargers** – Used in businesses, the charging stations can be located in car parks, workplaces, or at the malls. This type of charger uses 240 Volt AC outlet like the Charge Point CT4000 EV charging stations and is faster compared to Level 1 charging. It takes 3-8 hours for a full recharge and can also be used by home users benefitting them from receiving tax credit from the purchase and installation of the charger.
- **Level 3 EV chargers** – Also known as DC charging station and used in commercial sectors such as airports etc., this is the most powerful and fastest charging available today. It bypasses the on-board chargers on the EV charging the battery directly and chargers such as Blink DC Fast Charger can be fully charged in less than 30 minutes [10].

DC fast charging systems have higher power ratings and can be specified in two levels:

- **Level 1 DC Fast Charging systems** – Directly charges the car battery using an off-board DC charging framework. Maximum power rating of 40 kW can be supplied using the DC fast charger with a supply of 200-500 V DC voltage and a current rating of up to 80A.
- **Level 2 DC Fast Charging systems** - Directly charges the car battery using an off-board DC charging framework. Maximum power rating of 100 kW can be supplied using the DC fast charger with a supply of 200-500 V DC voltage and a current rating of up to 200A [11].

A typical charging system topology is shown in Figure 1.2.

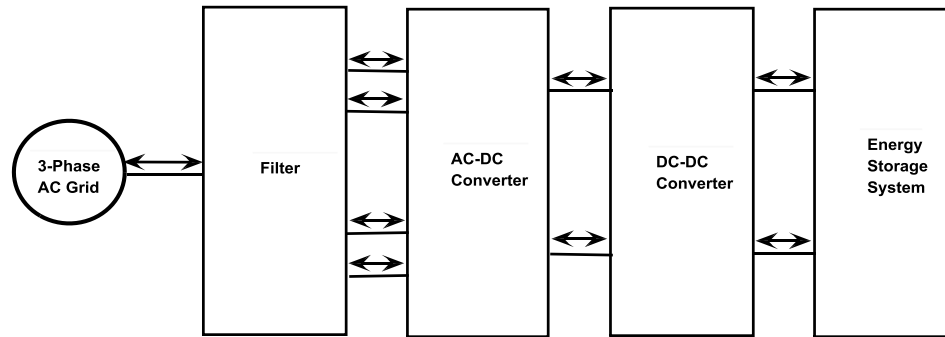


Figure 1.2: Three phase system topology of DC Charger of an EV [12].

Reference [12] covers an overview of fundamental components that make up the system that includes three-phase AC-DC rectifier, filters, buck converter and snubbers.

Understanding how these high power demanding systems when used in large quantities, will impact the existing grid infrastructure and its quality, considering

harmonic distortion and the power factor are of paramount importance [11]. As outlined in [13], the impact of PHEVs on regional electricity supplies is explored depending on different battery sized vehicles with varying charging rates.

Reference [14] divides charger systems into off-board and on-board types that can use either unidirectional or bidirectional power flow. Vehicle to grid (V2G) technology uses stored energy in EV battery that can be controlled while charging and discharging for bidirectional power flow [15]. Benefits and challenges of the V2G technology are highlighted in [67]. V2G has gained interests from the grid operators and owners of the vehicle and benefit the environment as well. The reference discussed the benefits of the V2G systems with regards to ancillary services such as voltage and frequency regulations, load shifting as well as they support and balance system employing renewable energy resources. The paper further discusses the challenges to the concept of V2G focusing on the degradation of the battery and highlights effects on distribution equipment such as losses in transformers, voltage deviation, harmonic distortion and peak demand. This will have a negative impact on the performance of the power grid and needs to be addressed when using V2G concept. Energy losses needs to be accounted for and using PHEVs that support V2G, investment costs involved with electrical networks needs to be a significant consideration. In reference [16], technical solutions are presented that integrate EVs to the power grid system. Reference [17] shows reduction in power losses in the system and how efficiency of the grid can be increased by proposing charging of several PHEVs in residential areas.

Power electronic converters comprising of AC-DC rectifiers and DC-DC converters make up the battery chargers [18]. Reference [19] offers a review of different techniques for Power Factor Correction (PFC) with their respective control schemes together with their pros and cons for the system. In [18] a simple AC-DC power converter is presented that charges the batteries of an EV using uncontrolled devices (diodes). It shows the converter has easier implementation, is cheaper to produce and rugged, but cannot regulate the output voltage and the current. The consumed current has a distorted waveform and contributes to PQ issues on the grid. Reference [20] presents the harmful effects of harmonics. Reference [21] states that input filter size requirements increase for smoothing the DC output, increasing the system cost.

Reference [18] discusses that with the use of controlled power electronic devices such as thyristors, IGBT, MOSFETS, the current waveform can be controlled, reducing the impact on the grid and a unity PF can be achieved. However, the cost of implementing this control system, power circuits and the entire system is more complex compared to the uncontrolled devices. According to [22], the use of new design configurations has resulted in lower harmonic distortion with power factor improvements. A report confirmed that actual current Total Harmonic Distortion (THD) between 2.36% and 5.26% at the start of charging reached up to 28% at the end of the charging period. On average the THD value has been suggested to be around 30% as the charger is considered to be a highly polluting load.

References [23] and [24] propose even more sophisticated converter configurations using current source rectifiers after an inverter stage that results in good PQ but require large electrolytic capacitors. In a current source rectifier, the diodes in series with the switches can increase power losses. Other concepts involving active power filters, line commutated rectifiers as well as multiple single phase PFC stages in the system have been reviewed [25]. However, it has been noted that using these controls for the converters increases system size, complexity, and overall system efficiency is reduced [21].

Reference [21] further reviews a new matrix converter (MC) that can support V2G power transfer. It is proposed that this new MC can overcome the issues presented by existing high power PHEV battery charging power systems. MCs are recognized as being more efficient, simple to design and can be implemented using fast switching power devices. MCs offer wide range of advantages to overcome the existing limiting configurations for EV chargers:

- V2G bidirectional power flow
- MCs are direct converters that do not need a capacitor at the converter side, reducing the bulk of components present in the system.
- Unity input power factor can be achieved
- High quality DC output voltage can be obtained resulting in smaller DC-link filter size

- Battery current is high quality and regulated in current control mode

References [26] and [27] cover the theories of AC-AC Matrix converter and present a configuration with reduced switches to make the converter work as an AC-DC rectifier. These papers also cover the MC capabilities of achieving unity power factor and control over output voltage using Space Vector PWM technique (SVPWM). Reference [28] uses SVPWM modulation technique for a three-phase MC rectifier with bi-directional power flow and power factor correction capabilities that regulates the output voltage in a wide range and this thesis focuses on using MCs to improve the power quality of the grid.

1.3 Research Scope and Objectives

This research focuses on modulation techniques of power converters for use in EV chargers. Conventional diode rectifiers with no control add a lot of harmonics into the grid. An increased number of such chargers would result in overall poor PQ of the grid.

Integrated AC-DC rectifiers using IGBT switches are presented in this thesis to study the PQ issues this converter adds on the grid. Matrix converter (MC) based rectifier configuration has been proposed to overcome many of the PQ issues with additional advantage of bidirectional power flow for V2G operation. MATLAB Simulink software is used for simulation of models used in this research work.

The major objectives of this thesis are:

- To develop an IGBT based rectifier with voltage and current controllers using SPWM technique
- To develop a matrix converter (MC) based three-phase rectifier using space-vector modulation technique
- To study the operational performance of these two rectifiers with the grid system regarding the steady state and dynamic responses.
- To study the PQ issues caused by the modelled rectifiers
- To study the system behavior under different fault conditions in case of small and large signal system disturbances
- To achieve a unity power factor in the modelled systems
- To achieve V2G operation using bi-directionality feature of the MC in the system

1.4 Thesis Outline

This thesis is comprised of seven chapters. Chapter 1 is an introduction including background, literature review, research scope and objectives and thesis outline.

Chapters 2 provides the system description and information regarding uncontrolled and controlled switches that can be used in the rectifier stage of an EV charger. This chapter also provides information on SPWM modulation technique used for generating gate pulses for IGBT switches. Chapter 3 covers the use of AC-AC matrix converter configuration and provides an in-depth look into using this converter as AC-DC rectifier.

The SVPWM modulation technique is used to provide gate signals for the switches to MC based rectifier is also covered in this chapter. Chapter 4 presents the MATLAB Simulink models for the three phase IGBT based rectifier and MC based rectifier with their respective controls. Chapter 5 provides simulation results for the two rectifier configurations modelled in chapter 4. This chapter also analyzes the behaviors of two models under steady state and dynamic conditions. Chapter 6 further analyzes the two modelled rectifier configurations responses under single-line-to-ground (SLG), double-line-ground (DLG) and triple-line-to-ground (TLG) faults. Finally, Chapter 7 summarizes the thesis with conclusions and recommends future work.

Chapter 2 EV Chargers and Power Converters

2.1 Introduction

This chapter covers a brief description of major stages that make up an EV charger; AC/DC rectifier stage and a DC/DC converter stage [29].

2.2 System Description

Charging times of the charging stations needs to be in realistic range catering to different criteria of consumers. For example, Nissan Leaf requires about 30 minutes of charging time with a level 3 quick charger DC 50kW, about 8 hours with home use charging dock and about 22 hours with level 1 charging stations. As more chargers appear in the market, they need to be regulated to avoid overload and other disturbances on the power grid that may cause power outages in local distribution systems. At present, much work is needed to increase reliability of these chargers that affect the PQ of the grid and feasible solutions are to be presented. This thesis looks into various problems encountered during charging of electric vehicles, and proposes a system with improved power quality.

Simulations are carried out for the power converters using MATLAB Simulink software. Figure 2.1 represent the system single line diagram depicting EV charger system connected to the grid. A fully controlled IGBT switch can be used in rectifiers to convert AC into DC for use in the charger. Passive filters are used to filter any harmonics

coming from rectifiers to reduce harmonic distortion on the grid. There is a wide range of voltage control when using IGBTs as switches in these converters therefore eliminating the requirement of using step down DC-DC Buck converters. Using SPWM technique, the three phase IGBT rectifiers have good control over the output voltage, active and reactive power as the two power components are decoupled to be controlled individually using vector control. Unity power factor can also be achieved using this control technique.

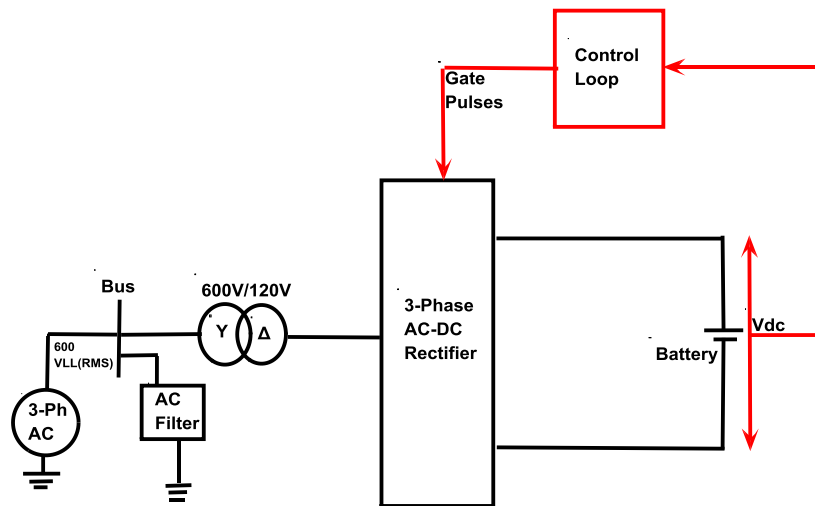


Figure 2.1: Single line system block diagram [30]

Matrix converter (MC) has obtained extensive attention because it is a single stage all-in-one converter, where the power losses can be reduced and a direct AC/DC

converter can be achieved. As discussed in section 1.2, MC has many advantages over the conventional converter topologies.

MATLAB Simulink software is used to depict how the use of MC using indirect space-vector modulation control technique can be used to improve the PF and PQ issues that EV chargers add on the grid. Also, MC offers additional benefit of bidirectional power flow capability that can be used in V2G technology.

2.3 Uncontrolled Diode Rectifiers

Diodes can be used in rectifiers but allow only one-way current flow. As there is no control over the diode switch, output voltage and current obtained are distorted and contain harmonics that affects the grid. Input filters can be used to reduce these harmonics but cannot eliminate the problem. Bulky capacitors and inductor components add to the size and cost of the rectifier. Diodes are best utilized in power converters by connecting them antiparallel to other components such as IGBT and MOSFET switches [31].

Figure 2.2 represents a three phase diode bridge rectifier where the phase voltages v_a , v_b , and v_c and their phase voltage amplitude V_m equals:

$$v_a = V_m \cos(\omega_0 t) \quad (2.1)$$

$$v_b = V_m \cos \left[\omega_0 t - \frac{2\pi}{3} \right] \quad (2.2)$$

$$v_c = V_m \cos \left[\omega_0 t - \frac{4\pi}{3} \right] \quad (2.3)$$

$$V_m = V_{PRMS} \sqrt{2} \quad (2.4)$$

Where V_{PRMS} is the phase voltage root-mean-square (RMS) value.

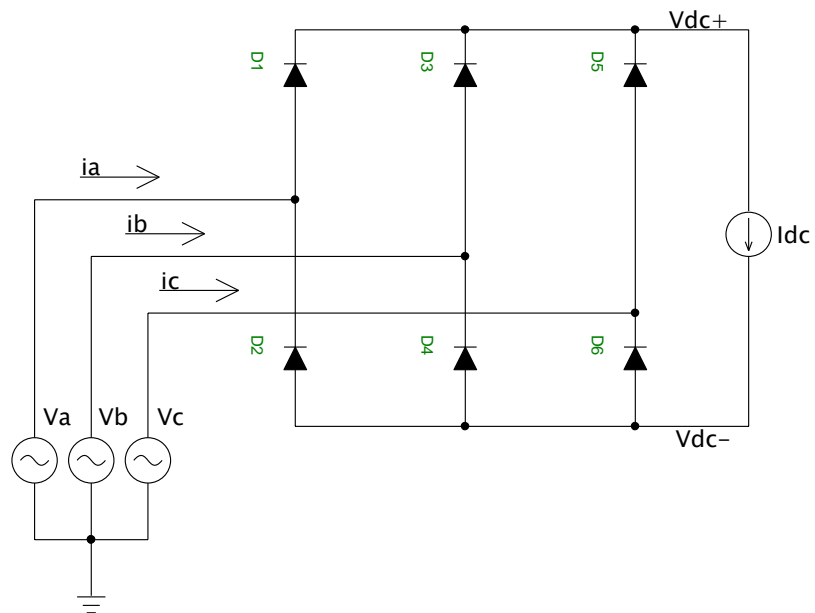


Figure 2.2: Three-phase diode bridge rectifier [32].

The DC component of the output voltage equals:

$$V_{dc} = \frac{3\sqrt{3}}{\pi} V_m \approx 1.65V_m \approx 2.34V_{PRMS} \quad (2.5)$$

All of the diode current waveforms have same average value and the input currents have the same RMS value that equals:

$$I_D = \frac{1}{3} I_{OUT} \quad (2.6)$$

$$I_{RMS} = \frac{\sqrt{6}}{3} I_{OUT} \quad (2.7)$$

Output power P_{out} , apparent power S_{in} and the Power Factor (PF) of the rectifier is obtained as:

$$P_{OUT} = V_{OUT} I_{OUT} = \frac{3\sqrt{3}}{\pi} V_m I_{OUT} = P_{IN} \quad (2.6)$$

$$S_{IN} = 3V_{PRMS} I_{RMS} = \sqrt{3} V_m I_{OUT} \quad (2.7)$$

$$PF = \cos\theta = \frac{P_{IN}}{S_{IN}} = \frac{3}{\pi} = 0.9549 \quad (2.8)$$

Power factor is a measure of effectiveness of the current being converted into useful output work and indicator of the effects of the load current on the supply system overall efficiency. Poor PF leads to an increase in load current causing additional losses in the supply and distribution systems. Hence, a PF close to unity is an important feature for any power system.

The total harmonic distortion (THD) is calculated from the input current, the RMS of the input current fundamental harmonic I_{1RMS} is:

$$I_{1RMS} = \frac{\sqrt{6}}{\pi} I_{OUT} \quad (2.9)$$

$$THD = \frac{1}{3} \sqrt{\pi^2 - 9} = 31.08\% \quad (2.10)$$

THD is relatively high in the three-phase diode rectifier and the use of this in the EV charger would significantly affect the power grid. These rectifiers are robust and cost less but draw reactive power from the source extremely affecting the power system quality [33].

2.4 Partially Controlled Thyristor Rectifiers

By using thyristor switches in the rectifier, firing angle α can be controlled within 0° to 90° to achieve a partial control over the switch. This type of thyristor operates at line frequency and is turned off by commutation using angle α . Conduction starts towards a forward direction when a trigger pulse is passed from gate to cathode. It then latches rapidly onto full conduction mode with a small drop in forward voltage. Natural behaviour of the circuit makes the current come back to zero as the gate signal cannot do this action. If continuous gate pulses are applied to the switch and the line inductance is kept zero then the circuit will behave like a three phase diode bridge rectifier. Snubber circuits are required to protect from high $\frac{di}{dt}$ and $\frac{dv}{dt}$.

A three phase partially controlled thyristor rectifier is represented in Figure 2.3.

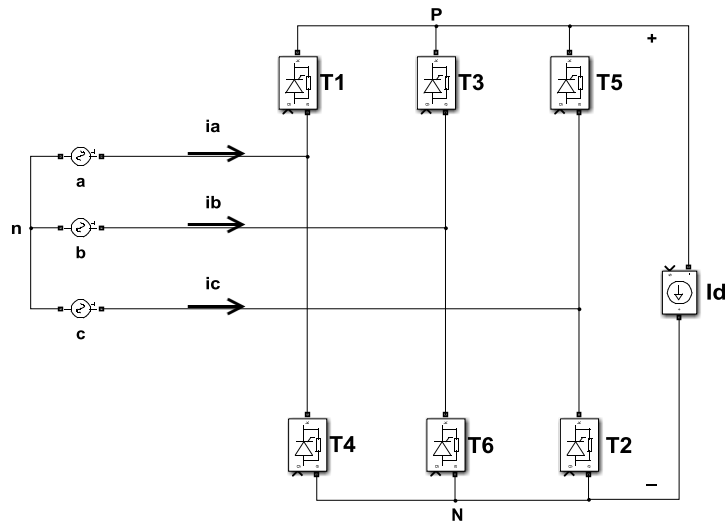


Figure 2.3: Three-phase partially controlled thyristor rectifier [34].

The balanced three-phase power supply consists of phase voltages:

$$v_a = \sqrt{2}V_{PH}\sin(\omega t)(a_n^2 + b_n^2)^{1/2} = \frac{2\sqrt{2}I_a}{n\pi} \sin \frac{n\pi}{3} \quad (2.11)$$

$$v_b = \sqrt{2}V_{PH}\sin(\omega t - \frac{2\pi}{3}) \quad (2.12)$$

$$v_c = \sqrt{2}V_{PH}\sin(\omega t - \frac{4\pi}{3}) \quad (2.13)$$

With their corresponding line to line voltages:

$$v_{ab} = \sqrt{2}V_{PH}\sin(\omega t + \frac{\pi}{6}) \quad (2.14)$$

$$v_{bc} = \sqrt{2}V_{LL}\sin(\omega t - \frac{\pi}{3}) \quad (2.17)$$

$$v_{ca} = \sqrt{2}V_{LL}\sin(\omega t - \frac{7\pi}{6}) \quad (2.15)$$

Where V_{PH} is the RMS value of the phase voltage, V_{LL} is the RMS value of the line to line voltage, and ω is the angular frequency of the input voltage. Current I_d flows through

one thyristor of the top group and one of the thyristor in the bottom groups. The converter voltage and current waveforms can be observed in Figure 2.4.

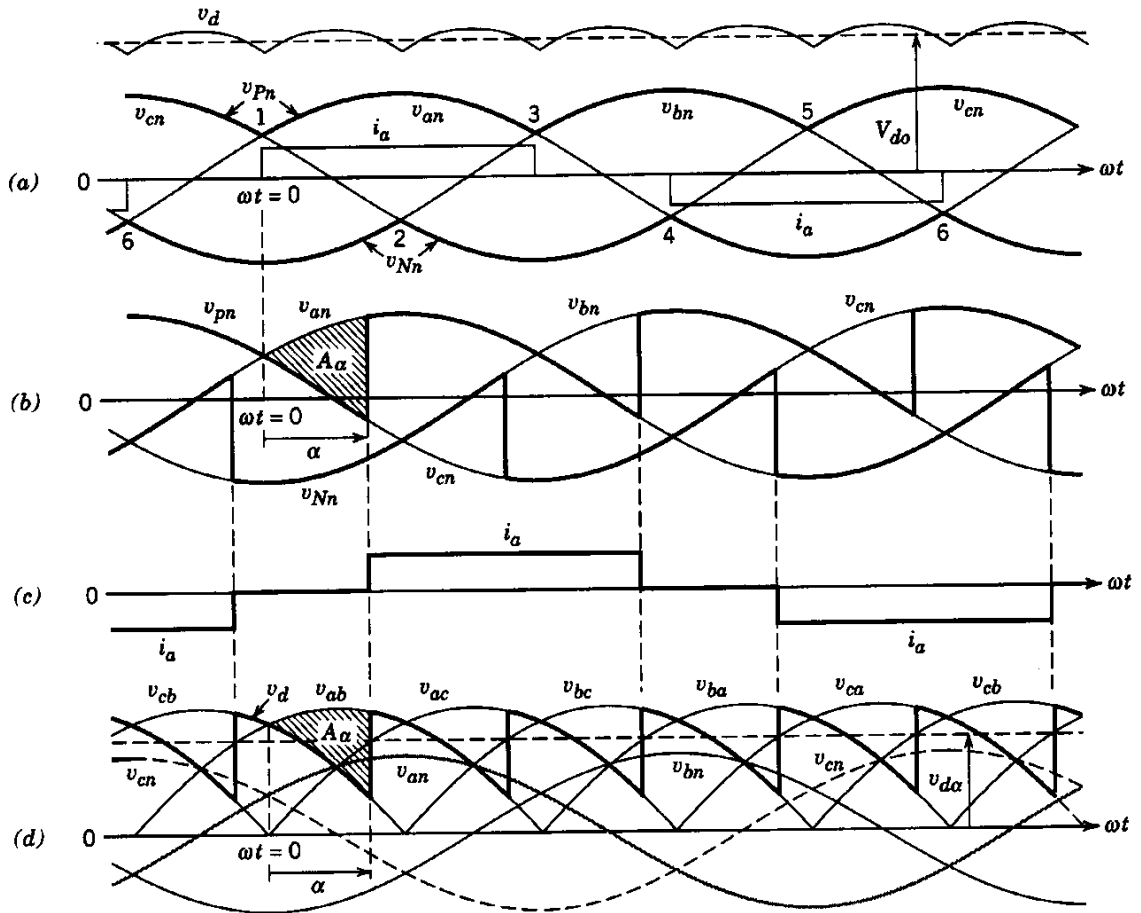


Figure 2.4: Three-phase thyristor Converter Waveforms [12].

The average output DC Voltage is given by:

$$V_{d\alpha} = V_{d0} - \frac{A_{\mu}}{\pi/3} \quad (2.16)$$

$$V_{ac} = \sqrt{2}V_{LL} \sin(\omega t) \quad (2.20)$$

The reduction in the average DC voltage due to the delay angle α is:

$$A_{\mu} = \int_0^{\alpha} \sqrt{2}V_{LL} \sin(\omega t) d(\omega t) \quad (2.21)$$

$$\begin{aligned} V_{d\alpha} &= V_{d0} - \frac{A_{\mu}}{\pi/3} = 1.35V_{LL} - \frac{\sqrt{2}V_{LL}(1 - \cos\alpha)}{\pi/3} = 1.35V_{LL}\cos\alpha \\ &= 1.35V_{d0} \end{aligned} \quad (2.22)$$

Average power is given by:

$$P_{d\alpha} = V_{d\alpha}I_d = 1.35V_{LL}I_d\cos\alpha \quad (2.23)$$

Reference [34] investigates a statistical method for calculating the THD and harmonic currents with various firing angles. Nth harmonic input current RMS (I_{nRMS}) and the total RMS current (I_{rms}) value can be obtained by:

$$I_{nRMS} = \frac{1}{\sqrt{2}}(a_n^2 + b_n^2)^{1/2} = \frac{2\sqrt{2}I_a}{n\pi} \sin \frac{n\pi}{3} \quad (2.24)$$

The THD is obtained using:

$$THD = \frac{(I_{1(rms)}^2 + I_{2(rms)}^2 + I_{3(rms)}^2 + \dots + I_{n(rms)}^2)^{1/2}}{I_{1(rms)}} \quad (2.26)$$

Table 2.1: Current harmonics and THD variations with varying firing angle [34].

α	0	15	30	45	60	90	110	130
THD	23.59	220.4	54.01	65.64	37.34	28.56	26.6	210.1
I₃/I₁	0.03	0.43	7.09	58.52	35.94	0.02	0.03	1.18
I₅/I₁	18.89	125.69	6.15	12.34	0.18	21.2	20.23	83.94
I₆/I₁	0.11	0.84	4.34	0.07	14.82	0.11	0.12	0.74
I₇/I₁	11.69	105.48	4.99	16.42	0.15	12.57	12.72	81.5
I₉/I₁	0.02	0.66	3.77	9.752	9.52	0.04	0.03	1.15
I₁₁/I₁	5.95	102.48	2.58	7.65	0.17	8.7	7.88	74.8

It can be seen in Table 2.1 that at $\alpha = 0$, the THD is 23.59% which is comparatively lower than that of a three phase diode bridge rectifier. By increasing the load inductance value the output current waveform could be smoothed out reducing current harmonics. Thyristor converters inject large harmonics into the utility system. PF is poor as the displacement power factor is $\cos \alpha$ and the distortion power factor is high due to increasing order of harmonic currents in the rectifier. Due to low PF, high current appears and the harmonic currents are increased compared to a three phase diode rectifier.

2.5 Fully Controlled Insulated-Gate Bipolar Transistor (IGBT) Rectifier

With the use of IGBT switches in the rectifier, full control over the converter can be achieved as precise gate-turn ON and OFF times can be controlled using PWM techniques compared to the thyristors where they are switched ON or OFF only once per cycle. The output voltage can be controlled over a wide range. Resultant waveforms of voltages and currents have fewer harmonics content and a unity PF can be achieved. IGBT based rectifiers can be used either as voltage source rectifier or current source rectifiers [35].

A voltage source rectifier with feedback loop control block is shown in Figure 2.5 the DC-link voltage is regulated at required value with the use of feedback control loop. The DC-link voltage is measured and compared with the reference voltage, V_{REF} and the error signal obtained is used to turn the gate signals of the six IGBT switches in three phase rectifiers. While in rectification mode, the capacitor C_D is discharged as long as the I_D current is positive. PWM signals are generated from the control block while more current flows to DC side from the AC side. Active and reactive power (P and Q) can be decoupled using direct-quadrature (d-q) control method in the controller for improving the PF. AC quantities become DC quantities in dq domain using dq method. This provides advantage where no tracking error is present when using PI controllers for regulating input AC currents. In order to prevent diodes conducting and behaving like a regular diode rectifier bridge, all the diodes needs to be negatively polarized for values of instantaneous AC voltage supply.

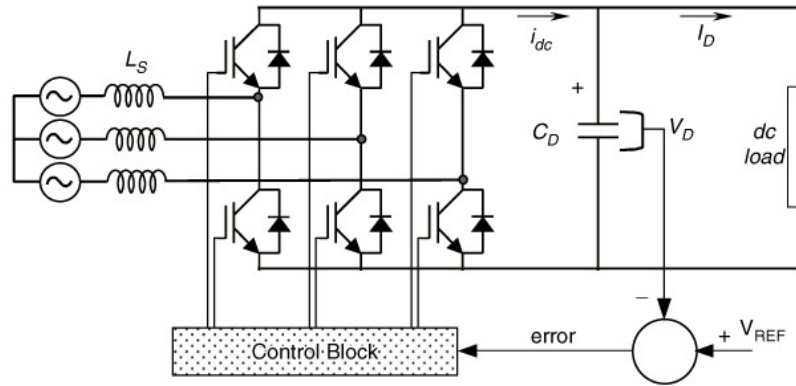


Figure 2.5: Voltage source rectifier operation [35]

A sinusoidal waveform of the voltage or current with PWM technique and the amplitude of the fundamental of this waveform (V_{MOD}) can be seen in Figure 2.6. Changing V_{MOD} affects the PWM signals applied on the switch to control their ON-OFF states.

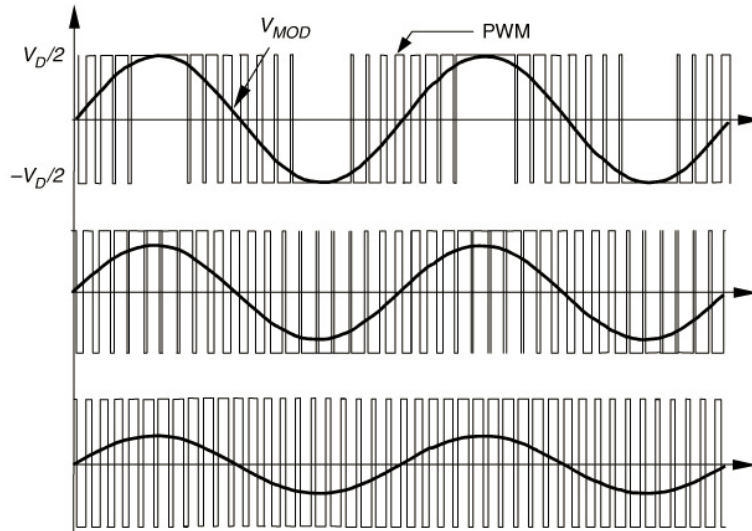


Figure 2.6: Resultant PWM with varying V_{MOD} [35].

$$v_{MOD}(t) = \left(V\sqrt{2} - RI_{max} - L_S \frac{dI_{max}}{dt} \right) \sin \omega t - X_S I_{max} \cos \omega t \quad (2.27)$$

Where V is the mains voltage, R is the input resistance, I_{max} is the input current amplitude, X_S is ωL_S and L_S is the source inductance. Using this equation (2.27) in implementation as shown in Figure 2.7, a voltage source voltage controlled PWM rectifier can be formed that can achieve unity power factor.

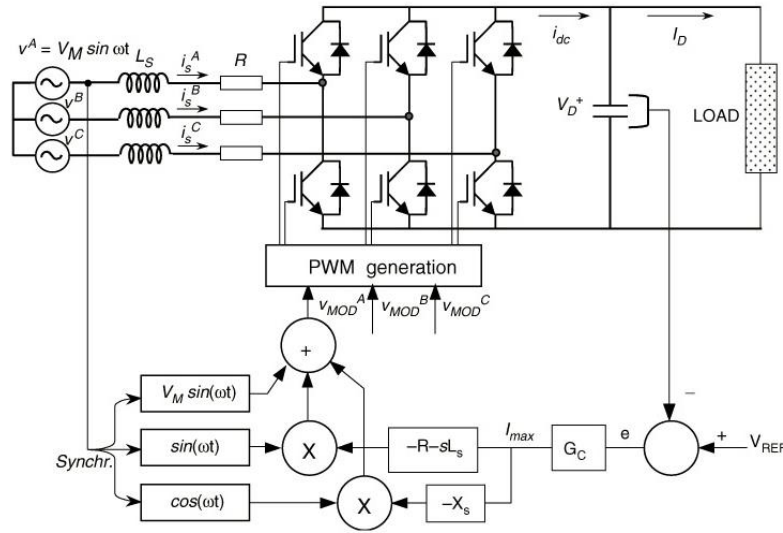


Figure 2.7: Voltage controlled PWM voltage source rectifier for unity PF [35].

2.5.1 Sinusoidal Pulse Width Modulation (SPWM)

Power converters and their applications are vast due to the semiconductor technology improvements offering increased voltage and current ratings and better switching techniques. Modern power electronic converters provide advantages of high efficiency, fast operation, small sizes among others with the help of switch mode control where operation of switching the devices ON or OFF are controlled [36]. Different types of PWM techniques are used by the power converters to suit application requirements.

PWM is a technique that controls the duty ratio of a pulsating waveform with the use of another input waveform. The intersection of the reference voltage waveform and the carrier waveform provide the switches specific ON and OFF timings. PWM is used in various applications such as converters, amplifiers, motor speed control etc. PWM strategy plays a very important role in reducing the harmonics and switching losses in three-phase converters. Various PWM techniques have been developed depending on application requirements one of which is a carrier-based PWM know as sinusoidal PWM (SPWM). Sinusoidal pulse width modulation (SPWM) control technique as shown in Figure 2.8 uses the modulation index (m) and the frequency modulation ratio (p).

$$m = \frac{V_{MOD}^{max}}{V_{TRIANG}^{max}} = \frac{V_{control}}{V_{tri}} \quad (2.28)$$

$$p = f_T / f_s \quad (2.29)$$

Where V_{MOD}^{max} and V_{TRIANG}^{max} , are the amplitudes of V_{MOD} and V_{TRIANG} .

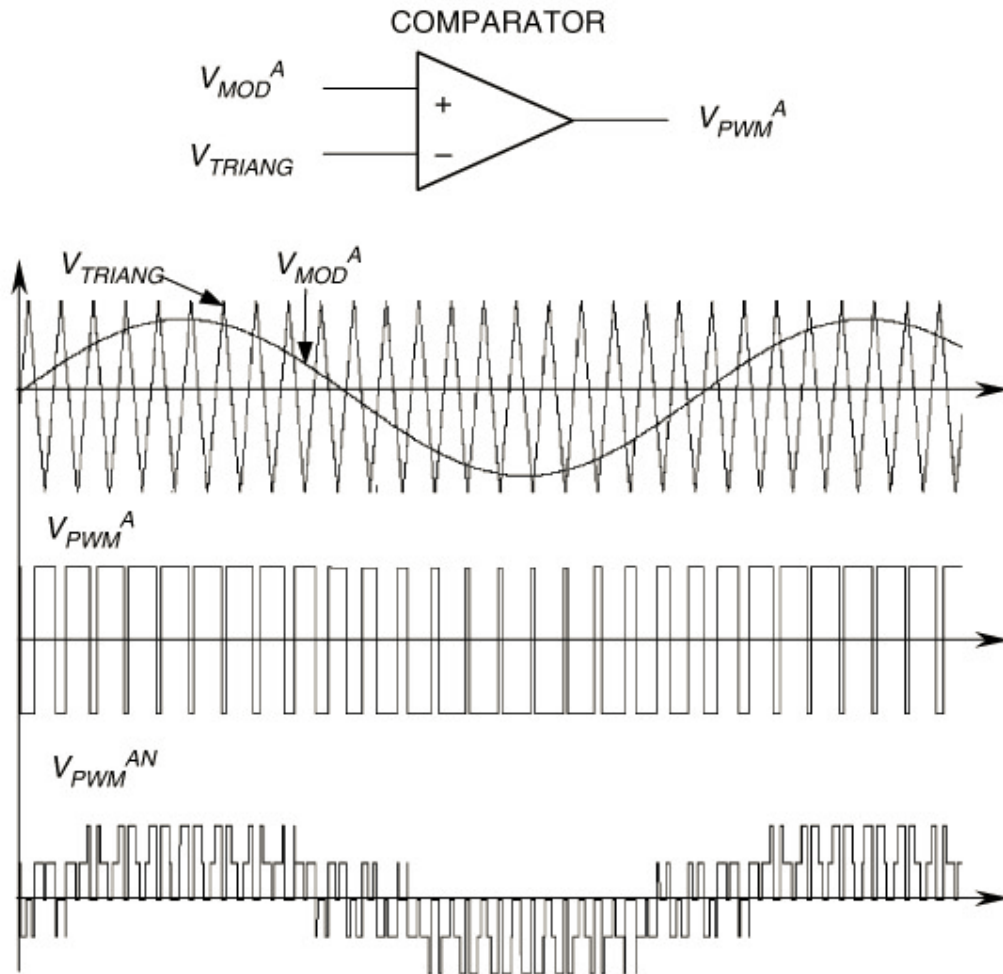


Figure 2.8: SPWM method [35].

In SPWM technique, high frequency triangular carrier signal is compared with a reference sinusoidal signal. As shown in Figure 2.8, the comparison of the two waves forms, when the sine wave is greater than the triangular wave, a PWM signal results that is applied as gate signal to the IGBT switch.

Any amplitude of the output voltage can be achieved by changing the PWM pattern. In power transmission this is very good for controlling the active and reactive power thus improving PF. For achieving unity PF each sinusoidal reference must be in phase with the supply phase voltage. The output voltage switches between $-\frac{V_{dc}}{2}$ and $+\frac{V_{dc}}{2}$ and V_{dc} is the total output DC voltage.

2.6 DC/DC Buck Converters

After the rectifier stage, the output DC voltage may need to be stepped further down to be used for EV chargers (typically $12V_{dc}$ or $24 V_{dc}$).

The DC-DC converter functions include regulation of output voltage (V_{dc}) against load and line variations and protect the source input from electromagnetic interference.

A typical buck converter can be seen in Figure 2.9 that comprises of an input source V_S , a controllable switch S , a diode D , an inductor L acting as a filter, C , a capacitor and the load resistance R . The converter is operated in continuous conduction mode where the inductor current is never zero. When the switch is off, the diode conducts allowing continuous current to flow through the inductor. When the switch is ON, the diode D is reverse biased and the waveforms where inductor current is always positive can be seen in Figure 2.10.

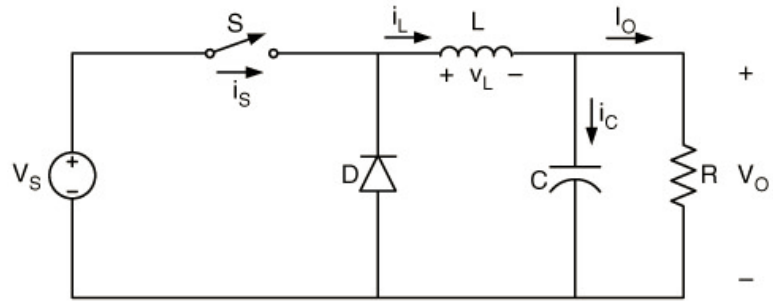


Figure 2.9: Buck Converter [12]

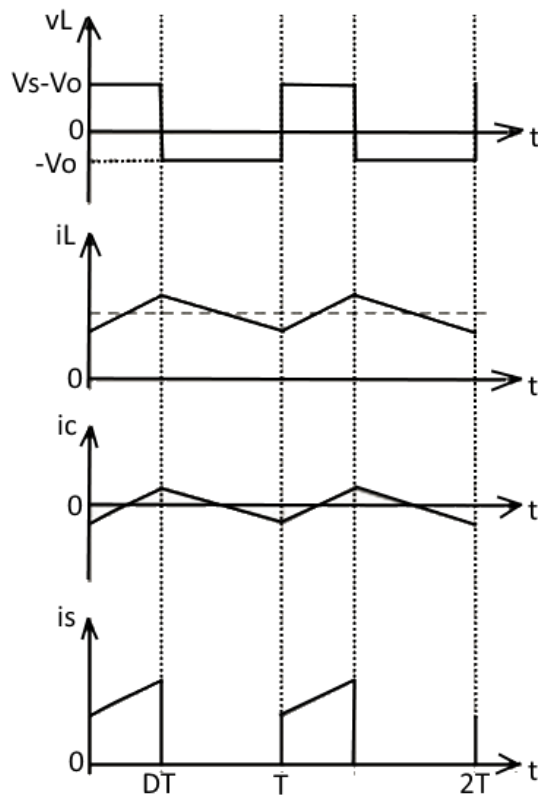


Figure 2.10: Inductor current always positive

The figure 2.10 shows DC-DC converter operation in continuous conduction mode where current in the inductor is always more than zero. The continuous conduction mode is better than discontinuous conduction mode for use in high frequency and makes better use of the passive components used in the converter. The boundary between these two modes is defined by:

$$L_b = \frac{(1 - D)R}{2f} \quad (2.30)$$

$$C_b = \frac{(1 - D)}{16Lf^2} \quad (2.31)$$

In continuous conduction mode, the inductor current has AC and DC components that flow through the capacitor that acts as a filter. A voltage ripple is produced across the output voltage because of this current. To limit this voltage ripple the capacitance value must be kept more than:

$$C_{min} = \frac{(1 - D)V_o}{8V_rLf^2} \quad (2.32)$$

The duty ratio D for the buck converter is:

$$D = \frac{V_o}{V_s} \quad (2.33)$$

Equation 2.33 confirms that the input voltage V_s is always more than output voltage V_o .

Inductor L and capacitor C values can be calculated from the equations below:

$$L = \frac{V_a(V_s - V_a)}{fV_s\Delta I} \quad (2.34)$$

$$C = \frac{\Delta I}{8f\Delta V_c} \quad (2.35)$$

Where ΔI the peak-to-peak is ripple current and ΔV_c is the peak-to-peak ripple voltage of the capacitor.

For low conduction losses of a converter and compactness, small passive components are used in the circuit. High frequency switches can reduce conduction losses while switching losses must be considered.

The buck converter is used to bring down the DC voltage to a level that is required by the charger battery for EV charging. In this thesis work, the IGBT and MC based rectifiers do not require the buck converter as their control covers a wide range for output voltage V_{dc} .

Chapter 3 Matrix Converter and Control Schemes

3.1 Introduction

Matrix Converter (MC) topology was initially introduced by Gyugi in 1976 [37]. MC has a capability of rectifying [38], inverting [39], and chopping [40]. In other words it can be used in direct AC-DC-AC conversion without any physical presence of a DC-link energy storage.

It is used in AC drive applications, to obtain compact voltage source converters to provide sinusoidal voltages at the output with different frequencies as well as amplitudes whilst consuming input currents with unity input PF.

MC is an emerging topology and have become very popular due to its various benefits such as sinusoidal input and output currents, improved power factor that is controllable and the fact that it has no bulky DC-link passive components present in its system topology [41] [42]. Except the use of small AC filters for eliminating ripples due to switching, MCs require no energy storage components. MC and its topology as a rectifier using indirect space vector modulation (SVM) technique forms a major part of this thesis. This chapter covers a typical AC-AC MC that is reduced in switch count to enable it to perform as an AC-DC rectifier.

3.2 Matrix Converter

Alesina and Venturini also used matrix converters in 1980's [43] and came up with a model and mathematical theory behind high-frequency synthesis converter. They also offered a modulation and controlled implementation of the MC using feed-back controller. In addition, they concluded that the maximum input-output transformation ratio that is possible for MC is 0.866 [44].

As part of the AC-AC converters, MCs can be divided into direct matrix converter (DMC) and indirect matrix converter (IMC). A simplified topology of the MC is shown in Figure 3.1 contains nine bi-directional switches where connections can be made between any of the input phase with any of the output phase. In principle, any of the voltages at the output can be generated through careful selection of the switches in the matrix converter. IGBTs are used as the switches and the MC module uses both IGBTs and diodes since IGBTs has a drawback of not blocking reverse voltages.

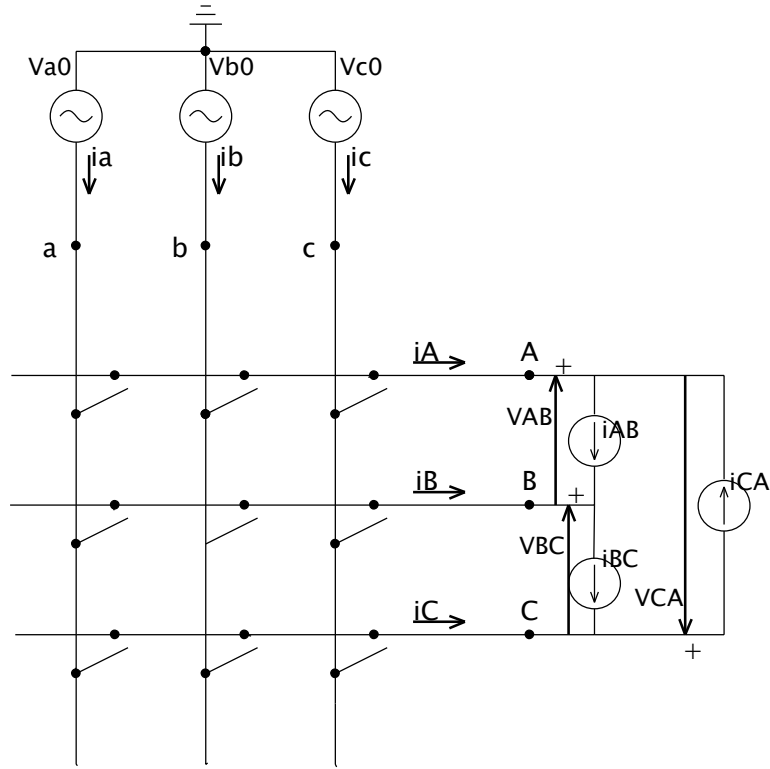


Figure 3.1: Three phase MC simplified structure [45] .

The switching function of a switch S_{jk} in Figure 3.1 can be defined as

$$S_{jk}(t) = \begin{cases} 1, & S_{jk} \text{ closed} \\ 0, & S_{jk} \text{ open,} \end{cases} \quad j \in \{A, B, C\}, k \in \{a, b, c\} \quad (3.1)$$

$$S_{ja} + S_{jb} + S_{jc} = 1, j \in \{A, B, C\} \quad (3.2)$$

With the constraints mentioned in equation 3.2, 27 combinations can be allowed using the switching pattern as shown in Table 3.1.

Table 3.1: Switching combination of three-phase to three-phase MC [45]

Group	A	B	C	v_{AB}	v_{BC}	v_{CA}	i_a	i_b	i_c	S_{Aa}	S_{Ab}	S_{Ac}	S_{Ba}	S_{Bb}	S_{Bc}	S_{Ca}	S_{Cb}	S_{Cc}
I	a	b	c	v_{ab}	v_{bc}	v_{ca}	i_A	i_B	i_C	1	0	0	0	1	0	0	0	1
	a	c	b	$-v_{ca}$	$-v_{bc}$	$-v_{ab}$	i_A	i_C	i_B	1	0	0	0	0	1	0	1	0
	b	a	c	$-v_{ab}$	$-v_{ca}$	$-v_{bc}$	i_B	i_A	i_C	0	1	0	1	0	0	0	0	1
	b	c	a	v_{bc}	v_{ca}	v_{ab}	i_C	i_A	i_B	0	1	0	0	0	1	1	0	0
	c	a	b	v_{ca}	v_{ab}	v_{bc}	i_B	i_C	i_A	0	0	1	1	0	0	0	1	0
	c	b	a	$-v_{bc}$	$-v_{ab}$	$-v_{ca}$	i_C	i_B	i_A	0	0	1	0	1	0	1	0	0
II-A	a	c	c	$-v_{ca}$	0	v_{ca}	i_A	0	$-i_A$	1	0	0	0	0	1	0	0	1
	b	c	c	v_{bc}	0	$-v_{bc}$	0	i_A	$-i_A$	0	1	0	0	0	1	0	0	1
	b	a	a	$-v_{ab}$	0	v_{ab}	$-i_A$	i_A	0	0	1	0	1	0	0	1	0	0
	c	a	a	v_{ca}	0	$-v_{ca}$	$-i_A$	0	i_A	0	0	1	1	0	0	1	0	0
	c	b	b	$-v_{bc}$	0	v_{bc}	0	$-i_A$	i_A	0	0	1	0	1	0	0	1	0
	a	b	b	v_{ab}	0	$-v_{ab}$	i_A	$-i_A$	0	1	0	0	0	1	0	0	1	0
II-B	c	a	c	v_{ca}	$-v_{ca}$	0	i_B	0	$-i_B$	0	0	1	1	0	0	0	0	1
	c	b	c	$-v_{bc}$	v_{bc}	0	0	i_B	$-i_B$	0	0	1	0	1	0	0	0	1
	a	b	a	v_{ab}	$-v_{ab}$	0	$-i_B$	i_B	0	1	0	0	0	1	0	1	0	0
	a	c	a	$-v_{ca}$	v_{ca}	0	$-i_B$	0	i_B	1	0	0	0	0	1	1	0	0
	b	c	b	v_{bc}	$-v_{bc}$	0	0	$-i_B$	i_B	0	1	0	0	0	1	0	1	0
	b	a	b	$-v_{ab}$	v_{ab}	0	i_B	$-i_B$	0	0	1	0	1	0	0	0	1	0
II-C	c	c	a	0	v_{ca}	$-v_{ca}$	i_C	0	$-i_C$	0	0	1	0	0	1	1	0	0
	c	c	b	0	$-v_{bc}$	v_{bc}	0	i_C	$-i_C$	0	0	1	0	0	1	1	0	0
	a	a	b	0	v_{ab}	$-v_{ab}$	$-i_C$	i_C	0	0	0	1	0	0	1	0	1	0
	a	a	c	0	$-v_{ca}$	v_{ca}	$-i_C$	0	i_C	1	0	0	1	0	0	0	1	0
	b	b	c	0	v_{bc}	$-v_{bc}$	0	$-i_C$	i_C	0	1	0	0	1	0	0	0	1
	b	b	a	0	$-v_{ab}$	v_{ab}	i_C	$-i_C$	0	0	1	0	0	1	0	1	0	0
III	a	a	a	0	0	0	0	0	0	1	0	0	1	0	0	1	0	0
	b	b	b	0	0	0	0	0	0	0	1	0	0	1	0	0	1	0
	c	c	c	0	0	0	0	0	0	0	0	1	0	0	1	0	0	1

Using this Table 3.1 and Figure 3.1, output line voltages and input phase currents can be achieved [45]:

$$\mathbf{v}_{oL} = \begin{bmatrix} v_{AB} \\ v_{BC} \\ v_{CA} \end{bmatrix} = \begin{bmatrix} S_{Aa} - S_{Ba} & S_{Ab} - S_{Bb} & S_{Ac} - S_{Bc} \\ S_{Ba} - S_{Ca} & S_{Bb} - S_{Cb} & S_{Bc} - S_{Cc} \\ S_{Ca} - S_{Aa} & S_{Cb} - S_{Ab} & S_{Cc} - S_{Ac} \end{bmatrix} \cdot \begin{bmatrix} v_{a0} \\ v_{b0} \\ v_{c0} \end{bmatrix} = \mathbf{T}_{PhL} \cdot \mathbf{v}_{iPh} \quad (3.3)$$

$$\mathbf{i}_{iPh} = \begin{bmatrix} i_a \\ i_b \\ i_c \end{bmatrix} = \mathbf{T}_{PhL}^T \cdot \begin{bmatrix} i_{AB} \\ i_{BC} \\ i_{CA} \end{bmatrix} = \mathbf{T}_{PhL}^T \cdot \mathbf{i}_{oL} \quad (3.4)$$

Where T denotes a transpose and \mathbf{T}_{PhL} is the input-phase to output line transfer function matrix of the MC. The output phase voltages and the input phase currents can be seen as [45]:

$$\mathbf{v}_{oPh} = \begin{bmatrix} v_{A0} \\ v_{B0} \\ v_{C0} \end{bmatrix} = \begin{bmatrix} S_{Aa} & S_{Ab} & S_{Ac} \\ S_{Ba} & S_{Bb} & S_{Bc} \\ S_{Ca} & S_{Cb} & S_{Cc} \end{bmatrix} \cdot \begin{bmatrix} v_{a0} \\ v_{b0} \\ v_{c0} \end{bmatrix} = \mathbf{T}_{PhPh} \cdot \mathbf{v}_{iPh} \quad (3.5)$$

$$\mathbf{i}_{iPh} = \begin{bmatrix} i_a \\ i_b \\ i_c \end{bmatrix} = \mathbf{T}_{PhPh}^T \cdot \begin{bmatrix} i_A \\ i_B \\ i_C \end{bmatrix} = \mathbf{T}_{PhPh}^T \cdot \mathbf{i}_{oPh} \quad (3.6)$$

Where matrix \mathbf{T}_{PhPh} is the input phase to output phase matrix. For this three phase MC, the three-phase input voltages can be given as [26]:

$$[V_i(t)] = \begin{bmatrix} V_{i1}(t) \\ V_{i2}(t) \\ V_{i3}(t) \end{bmatrix} = \begin{bmatrix} V_i \cos(\omega_i t) \\ V_i \cos(\omega_i t - 2\pi/3) \\ V_i \cos(\omega_i t + 2\pi/3) \end{bmatrix} \quad (3.7)$$

That produces the three-phase output voltages and gives the switching function $M(t)$ [26]:

$$[V_o(t)] = \begin{bmatrix} V_{o1}(t) \\ V_{o2}(t) \\ V_{o3}(t) \end{bmatrix} = [M(t)] \cdot \begin{bmatrix} V_{i1}(t) \\ V_{i2}(t) \\ V_{i3}(t) \end{bmatrix} = \begin{bmatrix} V_o \cos(\omega_o t + \theta_o) \\ V_o \cos(\omega_o t + \theta_o - 2\pi/3) \\ V_o \cos(\omega_o t + \theta_o + 2\pi/3) \end{bmatrix} \quad (3.8)$$

Where θ_o =output voltage phase angle [26].

The use of direct matrix converter (DMC) in the MC module is quite restricted due to its power rating [41] [46].

Indirect (two-stage) matrix converter (IMC) comprises of separated line and load bridges providing direct power conversion thus resolving the issue of high energy losses in passive components used in other power converter configurations. Also referred as “indirect MC” (IMC), “dual bridge MC” or “sparse matrix converter” which comprises of a current source type rectifier stage linked directly with a voltage source type inverter stage. IMC also offers an added benefit of reducing the number of switches of the supply bridge if the four quadrant operation of the MC is not required [47].

IMC offers a possibility of building more complex structures of the converter with multiple input and output ports [48]. IMC overcomes the disadvantages posed by DMC and is analyzed in [49] [50] [51] [52] [47] [53].

The maximum possible voltage ratio that can result from an AC-AC matrix converter in Figure 3.2 as seen from the Figure 3.3 and Figure 3.4 is [26]:

$$\frac{V_o}{V_{in}} = \frac{0.75}{0.866} = 0.866 \quad (3.9)$$

And the target output voltages to achieve this maximum transfer ratio then becomes [26]:

$$[V_o(t)] = \begin{bmatrix} V_{o1}(t) \\ V_{o2}(t) \\ V_{o3}(t) \end{bmatrix} = \begin{bmatrix} V_o \cos(\omega_o t + \theta_o) + \frac{V_i}{4} \cos(3\omega_i t) - \frac{V_o}{6} \cos(3\omega_o t + 3\theta_o) \\ V_o \cos(\omega_o t + \theta_o - 2\pi/3) + \frac{V_i}{4} \cos(3\omega_i t) - \frac{V_o}{6} \cos(3\omega_o t + 3\theta_o) \\ V_o \cos(\omega_o t + \theta_o + 2\pi/3) + \frac{V_i}{4} \cos(3\omega_i t) - \frac{V_o}{6} \cos(3\omega_o t + 3\theta_o) \end{bmatrix} \quad (3.10)$$

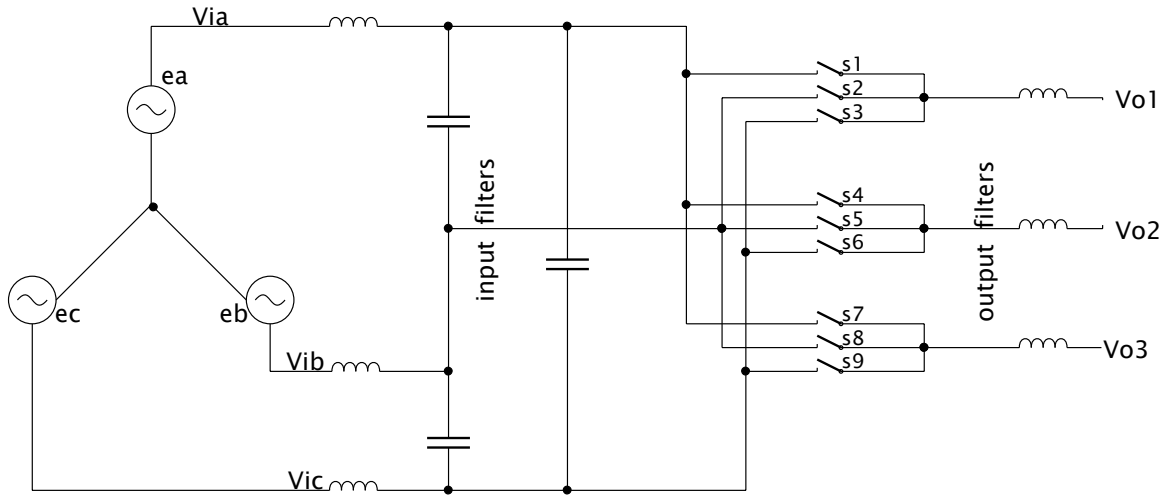


Figure 3.2: 3-phase AC-AC matrix converter architecture [26]

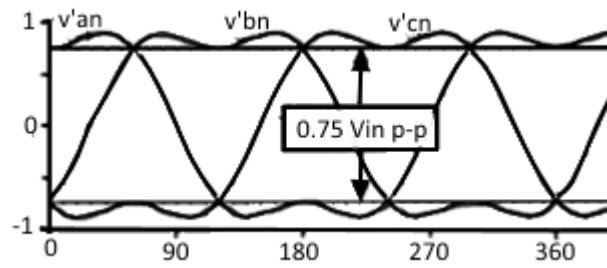


Figure 3.3: Matrix converter maximal available input voltage [26].

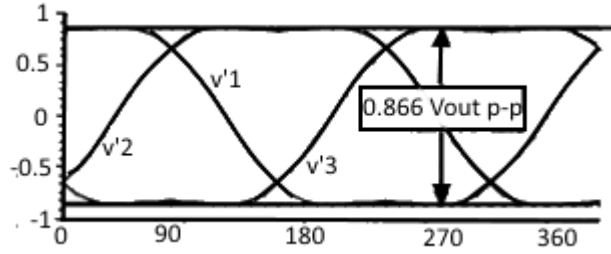


Figure 3.4: Output voltage reduction waveform [26].

For an AC-AC matrix converter, the modulation strategy $[m(t)]$ with a low frequency is required such that [27]:

$$[V_o(t)] = [m(t)] \cdot [V_i(t)] = V_o \cdot \begin{bmatrix} \cos(\omega_o t + \theta_o) \\ V_o \cos(\omega_o t + \theta_o - 2\pi/3) \\ V_o \cos(\omega_o t + \theta_o + 2\pi/3) \end{bmatrix} + \frac{V_o}{2\sqrt{3}} \begin{bmatrix} \cos(3\omega_i t) \\ \cos(3\omega_i t) \\ \cos(3\omega_i t) \end{bmatrix} - \frac{V_o}{6} \begin{bmatrix} \cos(3\omega_o t + 3\theta_o) \\ \cos(3\omega_o t + 3\theta_o) \\ \cos(3\omega_o t + 3\theta_o) \end{bmatrix} \quad (3.11)$$

$$= \quad [A] \quad + \quad [B] \quad + \quad [C]$$

Where $[V_i(t)]$ defined by equation 3.7 and $[m(t)]$ elements are limited by existence constraint and current continuity constraint [27]:

$$0 \leq m_{ij} \leq 1 \text{ for } 1 \leq i \leq 3 \text{ } 1 \leq j \leq 3 \quad (3.12)$$

$$\sum_{j=1}^3 m_{ij} = 1 \text{ for } 1 \leq i \leq 3$$

The output voltage set [A] in equation 3.11 is achieved through multiplication of the input voltage with $(\omega_o + \omega_i)$ for positive sets or by $(\omega_o - \omega_i)$ for negative sets to become [27]:

$$[m]_A = \frac{\beta_1}{3} \cdot \begin{bmatrix} m_+(1) & m_+(2) & m_+(3) \\ m_+(2) & m_+(3) & m_+(1) \\ m_+(3) & m_+(1) & m_+(2) \end{bmatrix} + \frac{\beta_2}{3} \cdot \begin{bmatrix} m_-(1) & m_-(3) & m_-(2) \\ m_-(2) & m_-(1) & m_-(3) \\ m_-(3) & m_-(2) & m_-(1) \end{bmatrix} \quad (3.13)$$

Where,

$$m_+(i) = \cos(\omega_o + \omega_i)t + \theta_o - (i - 1) 2\pi/3$$

$$m_-(i) = \cos(\omega_o - \omega_i)t + \theta_o - (i - 1) 2\pi/3$$

Power balance considerations give [27]:

$$\beta_1 = \frac{V_o}{V_i} \left(1 - \frac{\tan(\text{input pf angle})}{\tan(\text{output pf angle})} \right) \quad (3.14)$$

$$\beta_2 = \frac{V_o}{V_i} \left(1 + \frac{\tan(\text{input pf angle})}{\tan(\text{output pf angle})} \right)$$

Sets [B] and [C] in equation 3.11 gives [27]:

$$[m]_B = \frac{Y_1}{3} \cdot \begin{bmatrix} n_+(1) & n_+(2) & n_+(3) \\ n_+(1) & n_+(2) & n_+(3) \\ n_+(1) & n_+(2) & n_+(3) \end{bmatrix} + \frac{Y_2}{3} \cdot \begin{bmatrix} n_-(1) & n_-(3) & n_-(2) \\ n_-(1) & n_-(3) & n_-(2) \\ n_-(1) & n_-(3) & n_-(2) \end{bmatrix} \quad (3.15)$$

Where ,

$$n_+(i) = \cos[4\omega_i t - (i - 1) 2\pi/3]$$

$$n_-(i) = \cos[2\omega_i t - (i - 1) 2\pi/3]$$

$$Y_1 + Y_2 = \frac{1}{\sqrt{3}} \cdot \frac{V_o}{V_i}$$

$$[m]_C = \frac{\delta_1}{3} \cdot \begin{bmatrix} q_+(1) & q_+(2) & q_+(3) \\ q_+(1) & q_+(2) & q_+(3) \\ q_+(1) & q_+(2) & q_+(3) \end{bmatrix} + \frac{\delta_2}{3} \cdot \begin{bmatrix} q_-(1) & q_-(3) & q_-(2) \\ q_-(1) & q_-(3) & q_-(2) \\ q_-(1) & q_-(3) & q_-(2) \end{bmatrix} \quad (3.16)$$

Where ,

$$q_+(i) = \cos[(3\omega_o + \omega_i)t + 3\theta_o - (i - 1) 2\pi/3]$$

$$q_-(i) = \cos[(3\omega_o + \omega_i)t + 3\theta_o - (i - 1) 2\pi/3]$$

$i = 1,2,3$

$$\delta_1 + \delta_2 = -\frac{1}{3} \cdot \frac{V_o}{V_i}$$

Considering the current continuity constraints in equation 3.12, the complete solution becomes [27]:

$$[m(t)] = \frac{1}{3}[I] + [m]_A + [m]_B + [m]_C \quad (3.17)$$

Y_1, Y_2, δ_1 and δ_2 maximize the transfer ratio $\frac{V_o}{V_i}$ keeping existence

constraints in equation 3.12 in consideration:

$$Y_1 = -\frac{1}{6\sqrt{3}} \cdot \frac{V_o}{V_i}$$

$$Y_2 = \frac{7}{6\sqrt{3}} \cdot \frac{V_o}{V_i}$$

$$\delta_1 = -\frac{1}{6} \cdot \frac{V_o}{V_i}$$

$$\delta_2 = -\frac{1}{6} \cdot \frac{V_o}{V_i}$$

The modulation strategy for each switching period then yields:

1. $\beta_1, \beta_2, \gamma_1, \gamma_2, \delta_1$ and δ_2 scale coefficients are calculated for the input and output voltage ratio.
2. Using a look-up table, sinusoidal values of the modulation are calculated
3. $[m(t)]$, the modulation function values can then be calculated
4. Switches 1-9 are selected to turn on for the period $t_i = m_i(t)\Delta t$.

3.3 Controlled Single-Ended AC/DC Rectifier using Matrix Converter

To operate as AC-DC rectifier, the switches in MC are reduced from nine bi-directional switches to six. ω_o , the frequency at the output, is fixed to zero while the phase angle θ_o from the voltage at the output is fixed at 30° . The three phases at the output are seen to be at their maximal, minimal and zero level as shown in Figure 3.5. A $1.5 \times V_{in(peak)}$ can be then achieved for DC output voltage [27].

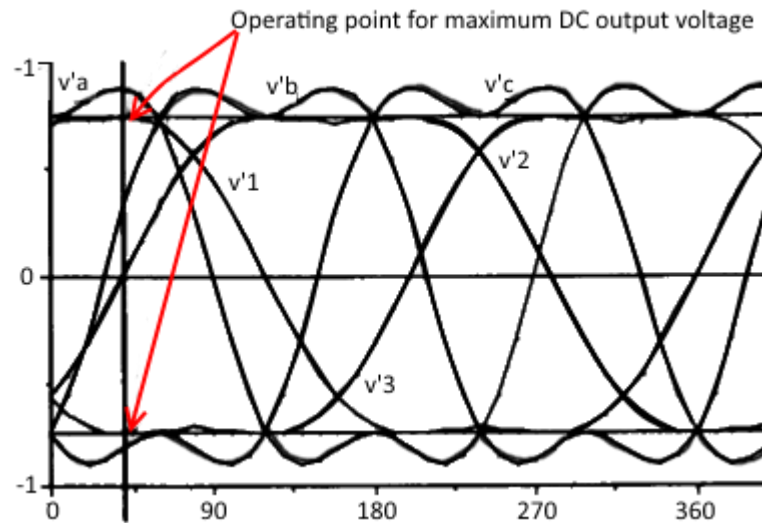


Figure 3.5: Operation of MC as a rectifier [27].

The target output voltage, $[V_o(t)]$ and the MC modulation function $[m(t)]$ is reduced to [27]:

$$[V_o(t)] = \begin{bmatrix} V_o \cdot \cos 30^\circ + \frac{V_o}{2\sqrt{3}} \cdot \cos(3\omega_i t) \\ zero + \frac{V_o}{2\sqrt{3}} \cdot \cos(3\omega_i t) \\ -V_o \cdot \cos 30^\circ + \frac{V_o}{2\sqrt{3}} \cdot \cos(3\omega_i t) \end{bmatrix} \quad (3.18)$$

$$[m(t)] = \begin{bmatrix} m_{11}(t) & m_{12}(t) & 1 - m_{11}(t) - m_{12}(t) \\ m_{21}(t) & m_{22}(t) & 1 - m_{21}(t) - m_{22}(t) \\ m_{31}(t) & m_{32}(t) & 1 - m_{31}(t) - m_{32}(t) \end{bmatrix} \quad (3.19)$$

Where the six expressions in the equations below gives the switch ON timings of the $S_1, S_2, S_3, S_7, S_8, S_9$ switches as shown in Figure 3.2, while $S_4, S_5,$ and S_6 are left to conduct for rest of the switching period Δt [27]:

$$m_{11}(t) = \frac{2}{\sqrt{3}} \cdot \frac{V_o}{V_i} \cdot \left\{ \frac{1}{2} \cos(\omega_i t) + \frac{7}{36} \cos(2\omega_i t) - \frac{1}{36} \cos(4\omega_i t) \right\} + \frac{1}{3} \quad (3.20)$$

$$m_{12}(t) = \frac{2}{\sqrt{3}} \cdot \frac{V_o}{V_i} \cdot \left\{ \frac{1}{2} \cos(\omega_i t - 2\pi/3) + \frac{7}{36} \cos(2\omega_i t + 2\pi/3) - \frac{1}{36} \cos(4\omega_i t - 2\pi/3) \right\} + \frac{1}{3} \quad (3.21)$$

$$m_{21}(t) = \frac{2}{\sqrt{3}} \cdot \frac{V_o}{V_i} \cdot \left\{ \text{zero} + \frac{7}{36} \cos(2\omega_i t) - \frac{1}{36} \cos(4\omega_i t) \right\} + \frac{1}{3} \quad (3.22)$$

$$m_{22}(t) = \frac{2}{\sqrt{3}} \cdot \frac{V_o}{V_i} \cdot \left\{ \text{zero} + \frac{7}{36} \cos(2\omega_i t + 2\pi/3) - \frac{1}{36} \cos(4\omega_i t - 2\pi/3) \right\} + \frac{1}{3} \quad (3.22)$$

$$m_{31}(t) = \frac{2}{\sqrt{3}} \cdot \frac{V_o}{V_i} \cdot \left\{ -\frac{1}{2} \cos(\omega_i t) + \frac{7}{36} \cos(2\omega_i t) - \frac{1}{36} \cos(4\omega_i t) \right\} + \frac{1}{3} \quad (3.23)$$

$$m_{32}(t) = \frac{2}{\sqrt{3}} \cdot \frac{V_o}{V_i} \cdot \left\{ -\frac{1}{2} \cos(\omega_i t - 2\pi/3) + \frac{7}{36} \cos(2\omega_i t + 2\pi/3) - \frac{1}{36} \cos(4\omega_i t - 2\pi/3) \right\} + \frac{1}{3} \quad (3.24)$$

This new algorithm grants precise control over the modulation and voltage at the output. Switches S_4, S_5 and S_6 may not be physically implemented for achieving the reduced AC-DC matrix converter, reducing the computational load. The switches implementation can be seen in the Figure 3.6 where 12 unidirectional switches are used, two switches are in back-to-back connection to make one bidirectional switch. The bidirectional AC-DC matrix converter with one DC output configuration among many other configurations is chosen to be modelled in this research work.

This configuration as shown in Figure 3.6 allows regeneration capability as the six switches ($S_1, S_2, S_3, S_7, S_8, S_9$) are bidirectional without the need for dead time between each switching sequence [27]. The reduced modulation function in equation 3.19 is used in this work after reduction to:

$$[m(t)] = \begin{bmatrix} m_{11}(t) & m_{12}(t) & 1 - m_{11}(t) - m_{12}(t) \\ m_{31}(t) & m_{32}(t) & 1 - m_{31}(t) - m_{32}(t) \end{bmatrix} \quad (3.25)$$

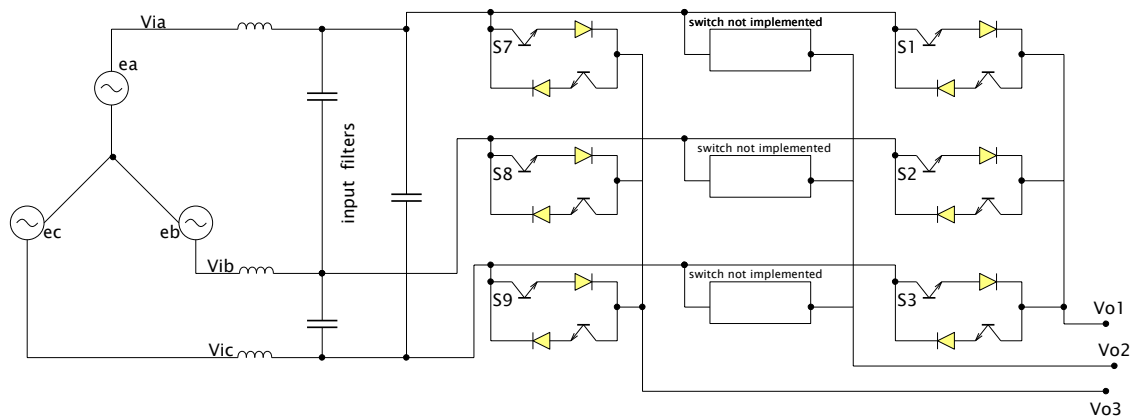


Figure 3.6: Bi-directional AC-DC matrix converter with one DC output [27].

3.4 Space-Vector Pulse Width Modulation (SVPWM)

Matrix converter uses a direct conversion AC-AC stage as compared to two stages for the rectifier/inverter solution. Many modulation techniques and mathematical models have been considered by researchers over the years for matrix converters including Venturini first method [54] [55], Venturini optimum method [44] [56] and scalar modulation method [57] [58].

The Space vector Pulse Width Modulation (SVPWM) has advantages over the commonly used PWM technique where its output voltage is 15.5% greater than conventional PWM technique. By injecting selected harmonics into the sinusoidal wave, a modulating signal can be generated. This results in flat topped waveform, amount of over modulation is reduced and it gives an increased fundamental amplitude and less distorted output voltage [59]. Phase variables from the three input voltages and currents from the AC side can be expressed in space vectors [7].

SVPWM takes a sinusoidal voltage as a amplitude vector that rotates at a constant angular frequency, ω . This vector is represented in dq plane denoting real and imaginary axes. SVPWM aims to approximate the reference voltage V_{ref} from the switching sequences. Selected vectors that are stationary can provide the desirable phase shift between input current and voltage that needs a selection of switching vectors and calculation of the vector time intervals are required in the modulation process. Zero vectors and active vectors are the vectors presented in the SVPWM. Implementation of the SVPWM can be made by calculating V_d, V_q, V_{ref} , and angle (α) as

well as the time intervals, duty cycles d_γ, d_δ, d_0 and switching time of each IGBT switches ($S_1, S_2, S_3, S_7, S_8, S_9$).

3.4.1 Indirect SVM for Rectifier

Figure 3.7 shows a space vector diagram with sectors created by switching states that the rectifier is capable of generating. The input currents I_a, I_b and I_c , the output voltage V_{dc} , the input current space vector I_{IN} (I_1 - I_6) and input voltage space vector V_{IN} (V_1 - V_6) can be represented as:

$$\begin{bmatrix} I_a \\ I_b \\ I_c \end{bmatrix} = \begin{bmatrix} S_1 & S_7 \\ S_2 & S_8 \\ S_3 & S_9 \end{bmatrix} \cdot \begin{bmatrix} I_{DC+} \\ I_{DC-} \end{bmatrix} \quad (3.26)$$

$$\begin{bmatrix} I_a \\ I_b \\ I_c \end{bmatrix} = \begin{bmatrix} m_{11}(t) & m_{31}(t) \\ m_{12}(t) & m_{32}(t) \\ 1 - m_{11}(t) - m_{12}(t) & 1 - m_{31}(t) - m_{32}(t) \end{bmatrix} \cdot \begin{bmatrix} I_{DC+} \\ I_{DC-} \end{bmatrix} \quad (3.27)$$

$$\begin{bmatrix} V_{DC+} \\ V_{DC-} \end{bmatrix} = \begin{bmatrix} S_1 & S_2 & S_3 \\ S_7 & S_8 & S_9 \end{bmatrix} \cdot \begin{bmatrix} V_a \\ V_b \\ V_c \end{bmatrix} \quad (3.28)$$

$$I_{IN} = \frac{2}{3} (I_a + I_b \cdot e^{j2\pi/3} + I_c \cdot e^{j4\pi/3}) \quad (3.29)$$

$$V_{IN} = \frac{2}{3} (V_a + V_b \cdot e^{j2\pi/3} + V_c \cdot e^{j4\pi/3}) \quad (3.30)$$

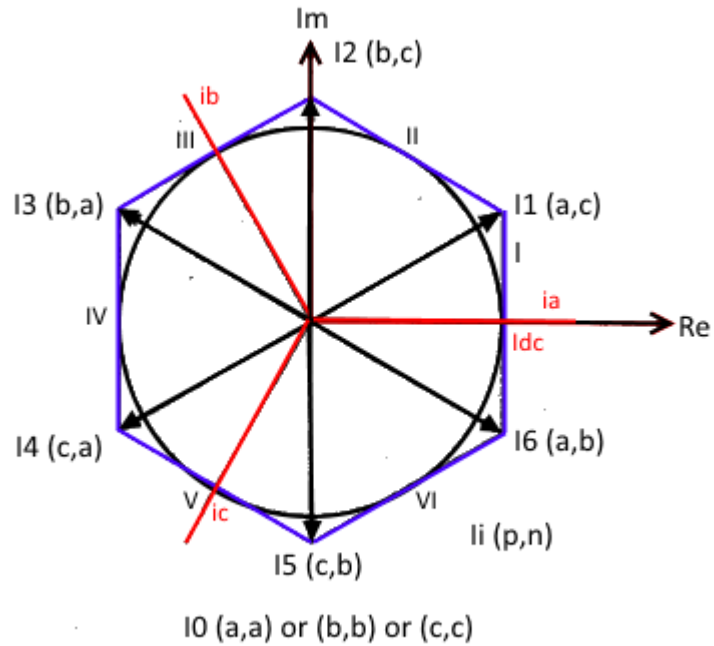


Figure 3.7: Space vector diagram for rectifier current with sectors [45].

The six active, three zero vectors and the possible switch states are represented in the Table 3.2 [28]:

Table 3.2: Commutation combinations of the converter [28].

Commutation States (N)	V_{DC}	Phase Currents			$\begin{bmatrix} S_1 & S_2 & S_3 \\ S_7 & S_8 & S_9 \end{bmatrix}$	Vector	States
		I_a	I_b	I_c			
1	V_{ac}	I_{DC+}	0	I_{DC-}	$\begin{bmatrix} 1 & 0 & 0 \\ 0 & 0 & 1 \end{bmatrix}$	$I_1[ac]$	I_1
2	V_{bc}	0	I_{DC+}	I_{DC-}	$\begin{bmatrix} 0 & 1 & 0 \\ 0 & 0 & 1 \end{bmatrix}$	$I_2[bc]$	I_2
3	$-V_{ab}$	I_{DC-}	I_{DC+}	0	$\begin{bmatrix} 0 & 1 & 0 \\ 1 & 0 & 0 \end{bmatrix}$	$I_3[ab]$	I_3
4	$-V_{ac}$	I_{DC-}	0	I_{DC+}	$\begin{bmatrix} 0 & 0 & 1 \\ 1 & 0 & 0 \end{bmatrix}$	$I_4[ac]$	I_4
5	$-V_{bc}$	0	I_{DC-}	I_{DC+}	$\begin{bmatrix} 0 & 0 & 1 \\ 0 & 1 & 0 \end{bmatrix}$	$I_5[bc]$	I_5
6	V_{ab}	I_{DC+}	I_{DC-}	0	$\begin{bmatrix} 1 & 0 & 0 \\ 0 & 1 & 0 \end{bmatrix}$	$I_6[ab]$	I_6
7	0	0	0	0	$\begin{bmatrix} 1 & 0 & 0 \\ 1 & 0 & 0 \end{bmatrix}$	$I_7[aa]$	I_7
8	0	0	0	0	$\begin{bmatrix} 0 & 1 & 0 \\ 0 & 1 & 0 \end{bmatrix}$	$I_8[bb]$	I_8
9	0	0	0	0	$\begin{bmatrix} 0 & 0 & 1 \\ 0 & 0 & 1 \end{bmatrix}$	$I_9[cc]$	I_9

For example, if vector $I_6[ab]$ magnitude needs to be calculated, this indicates that the input phase a is connected to the positive rail of V_{DC+} , and the input phase b is connected to the negative rail V_{DC-} so the vector I_6 can be calculated with reference to these phases using equation 3.29 as:

$$\begin{aligned} I_6 &= \frac{2}{3} (I_a + I_b \cdot e^{j2\pi/3} + I_c \cdot e^{j4\pi/3}) \\ &= \frac{2}{3} (I_{DC} - I_{DC} \cdot e^{j2\pi/3} + 0 \cdot e^{j4\pi/3}) \\ &= \frac{2}{\sqrt{3}} I_{DC} \cdot e^{-j\pi/6} \end{aligned}$$

Figure 3.7 shows the space vectors in a complex plane. It is necessary to have a zero vector in between each switching state to create dead times and prevent accidental short circuit. This follows with the representation of converter states in Figure 3.8 showing switches sequences, optimum sequence of step and ON state of switches in each state. It can be seen from both these Figures 3.7 and 3.8 that each switching period is for $-30^\circ < \omega_i t < 30^\circ$.

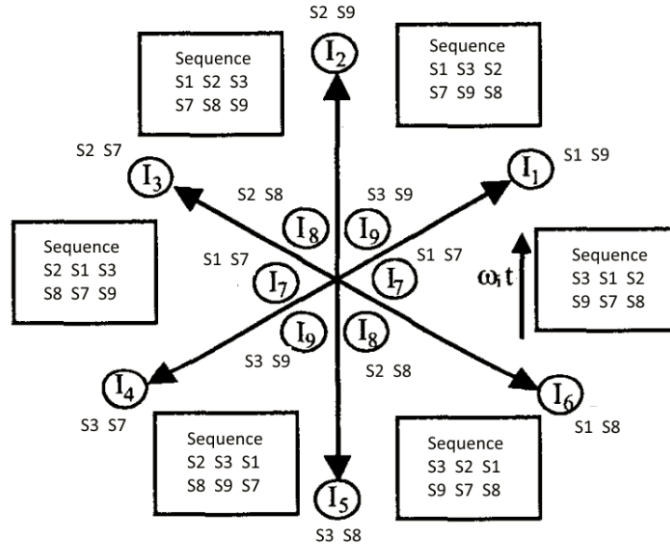


Figure 3.8: Depiction of the converter states [28].

Once the active vectors are determined, the duty cycles d_γ , d_δ , d_0 are calculated.

The Figure 3.9 shows the reference current vector:

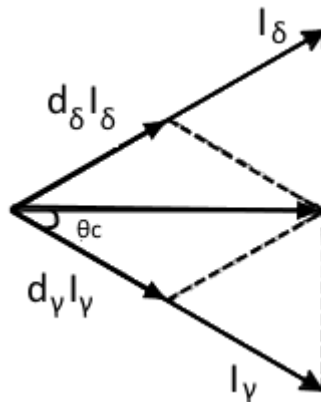


Figure 3.9: Reference current vector

Considering constant input currents during switching interval T_S , the reference current vector and the duty cycles for the active cycles can then be calculated:

$$I_i^* = d_Y \cdot I_Y + d_\delta \cdot I_\delta \quad (3.30)$$

$$d_Y = \frac{T_Y}{T_S} = m_C \cdot \sin\left(\frac{\pi}{3} - \theta_C\right) \quad (3.31)$$

Where, m_C is the current modulation index and θ_C is the angle of the reference current vector.

$$d_\delta = \frac{T_\delta}{T_S} = m_C \cdot \sin(\theta_C) \quad (3.32)$$

$$d_0 = \frac{T_0}{T_S} = 1 - d_Y - d_\delta \quad (3.33)$$

Duty cycles define the switches ON time; a symmetric sequence principle is used to achieve this where the switching period is halved and the duty cycles are mirrored for the remaining cycle to complete a full switching period. The switching transitions are

doubled this way but there is a reduced THD. There are seven number of commutations in one sampling period.



Figure 3.10: Basic Switching Sequence Principle

Safe control of the four-quadrant switches is used to obtain the gating signals of the six switches. This is required to avoid open and short circuits in the converter. Independent control of the current in both directions is possible, allowing for bi-directionality feature of the MC. For the AC-DC matrix converter, three four-quadrant switches are connected to the same output phase (and three switches in the lower are connected to same output phase) and can allow 15 switch state combinations as expressed in Table 3.3.

Table 3.3: Four-quadrant switches state combinations [28].

State	S ₁₊	S ₁₋	S ₂₊	S ₂₋	S ₃₊	S ₃₋	Current sign
1	1	1	0	0	0	0	← ⁻ + ⁻ →
2	0	0	1	1	0	0	← ⁻ + ⁻ →
3	0	0	0	0	1	1	← ⁻ + ⁻ →
4	1	0	0	0	0	0	+ →
5	0	1	0	0	0	0	← ⁻
6	0	0	1	0	0	0	+ →
7	0	0	0	1	0	0	← ⁻
8	0	0	0	0	1	0	+ →
9	0	0	0	0	0	1	← ⁻
10	1	0	1	0	0	0	+ →
11	0	1	0	1	0	0	← ⁻
12	0	0	1	0	1	0	+ →
13	0	0	0	1	0	1	← ⁻
14	1	0	0	0	1	0	+ →
15	0	1	0	0	0	1	← ⁻

Chapter 4 System Modelling

4.1 Three-Phase IGBT Rectifier System Modelling

A three-phase, 2-level with six switches topology is implemented for each rectifier modelling. An ideal IGBT is connected with anti-parallel diode to make one unit. SPWM technique is used in the control system to generate the pulses which are used as gate signals for the six IGBT switches. Switching frequency of the carrier is 1620 Hz resulting in 27 operations of ON-OFF in each cycle. Switches 1 and 4 are connected to phase A, 3 and 6 are connected to phase B and switches 2 and 5 are connected to phase C respectively as shown in Figure 4.1.

The switches in the same phase have complementary gate signals to prevent short circuit across the output of the rectifier. RC snubber circuit is formed as part of the anti-parallel diode to reduce the rate of change of voltage during the switch ON time of the IGBTs. The snubber values are estimated for the system that optimize the system and reduce the voltage and current stresses in the IGBTs. Two DC capacitors of 5000 μF connected in series across the DC terminals are required to maintain the output voltage (V_{dc}) in the system. System parameters used in system modelling are provided in Appendix A, where the battery is depicted as a constant voltage source assuming ideal conditions with no power losses. The modelling of the full EV battery with its specifications (Matlab model in Appendix B) is beyond the scope of this thesis work.

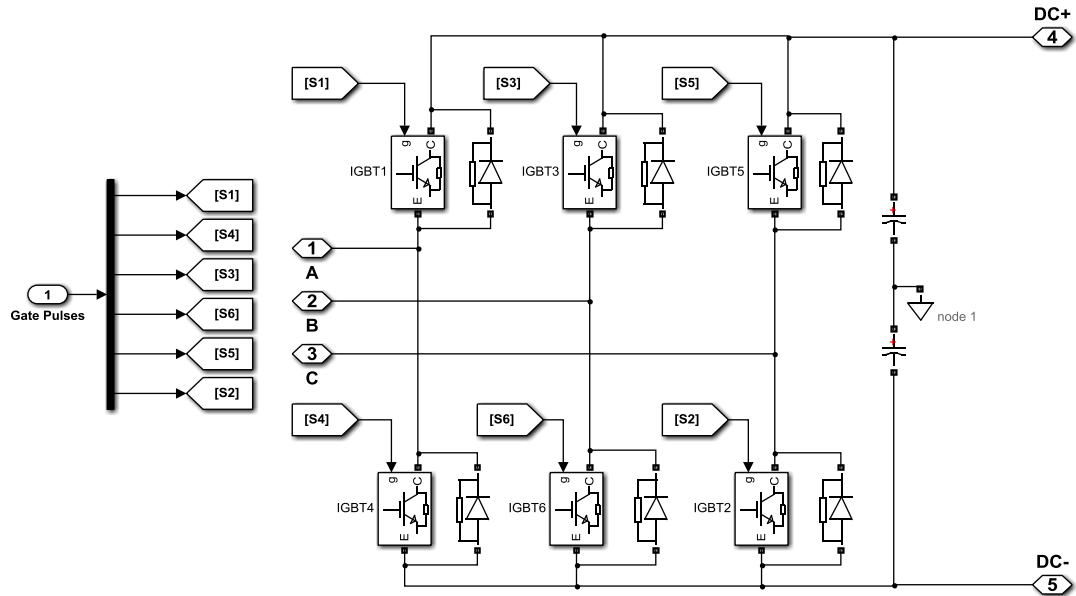


Figure 4.1: IGBT Rectifier Model

Figure 4.2 depicts comparison of a triangular wave with the modulated sine waveforms for generating gate pulses for the six switches. As mentioned in section 2.5.1, SPWM method is implemented for this model where the modulation index is as given by equation 2.28. $V_{Control}$ (V_{abc}) is the amplitude of the three modulating sine waveforms at 60 Hz each 120 degree phase shifted and the V_{tri} is the amplitude of the triangular waveform. The triangular waveform frequency determines the rectifier switching frequency and is kept constant. The three switches of the upper leg of the rectifier

receive the PWM trigger signals and the lower leg switches receives the complementary gate signals in order to operate two switches in the same leg for the same phase.

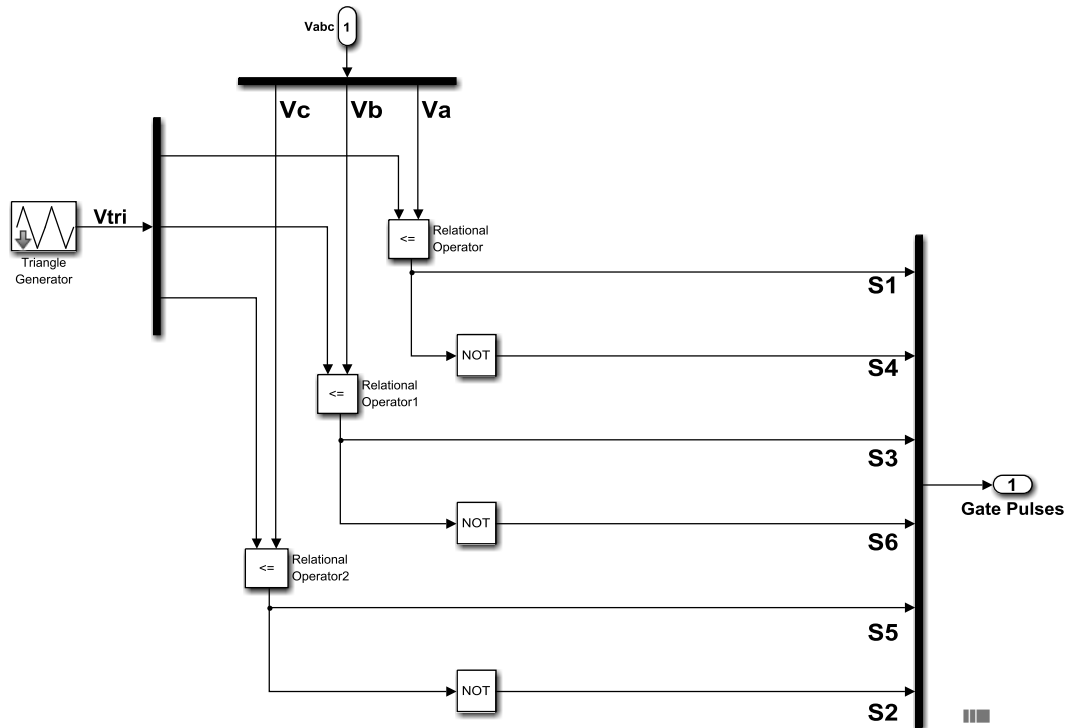


Figure 4.2: SPWM Generator.

Phase locked loop (PLL) is used to detect the phase difference between the input voltage signals V_{abc} and voltage d-q components (i.e v_d , v_q). A PID controller is used for controlling the phase difference between the axes such that it is held constant, and uses this signal as a feedback for the PLL, making it a negative feedback system. The voltage

d-q components are calculated using Park's transformation. This method is used to transform three phase system abc to synchronously rotating two phase dq –reference frame using [60]:

$$\begin{bmatrix} v_d \\ v_q \end{bmatrix} = \frac{2}{3} \begin{bmatrix} \cos \omega t & \sin \omega t \\ \cos(\omega t - 120^\circ) & -\sin(\omega t - 120^\circ) \\ \cos \omega t + 120^\circ & -\sin(\omega t + 120^\circ) \end{bmatrix}^T \cdot \begin{bmatrix} v_a \\ v_b \\ v_c \end{bmatrix} \quad (4.1)$$

Figure 4.3 shows the model for the decoupling operation of active and reactive power. Two PI regulators are used as inner current control loops to decouple and control the d and q components of the current. One outer loop PI regulator is used for controlling the output voltage (V_{dc}). The I_d component from the abc/dq transformation is used to control the active power and I_q component is used for controlling the reactive power. The reference current I_{qref} is set to zero in order to have the reactive power set to zero in dynamic response of the system to achieve unity power factor. I_{dref} is set by the outer voltage control loop to maintain the output voltage (V_{dc}). The two inner current control loops use PI controller for controlling the DC components of the current and reducing the error of the fundamental components to zero. Resonant controllers are also employed to reduce computation and noise in the system [36].

The power factor is calculated using:

$$PF = \frac{P}{S} \tag{4.4}$$

Where P is the real power of the system and S is the apparent power of the system

$$S^2 = P^2 + Q^2 \tag{4.5}$$

Where Q is the reactive power of the system

The complete system model can be seen in Figure 4.4.

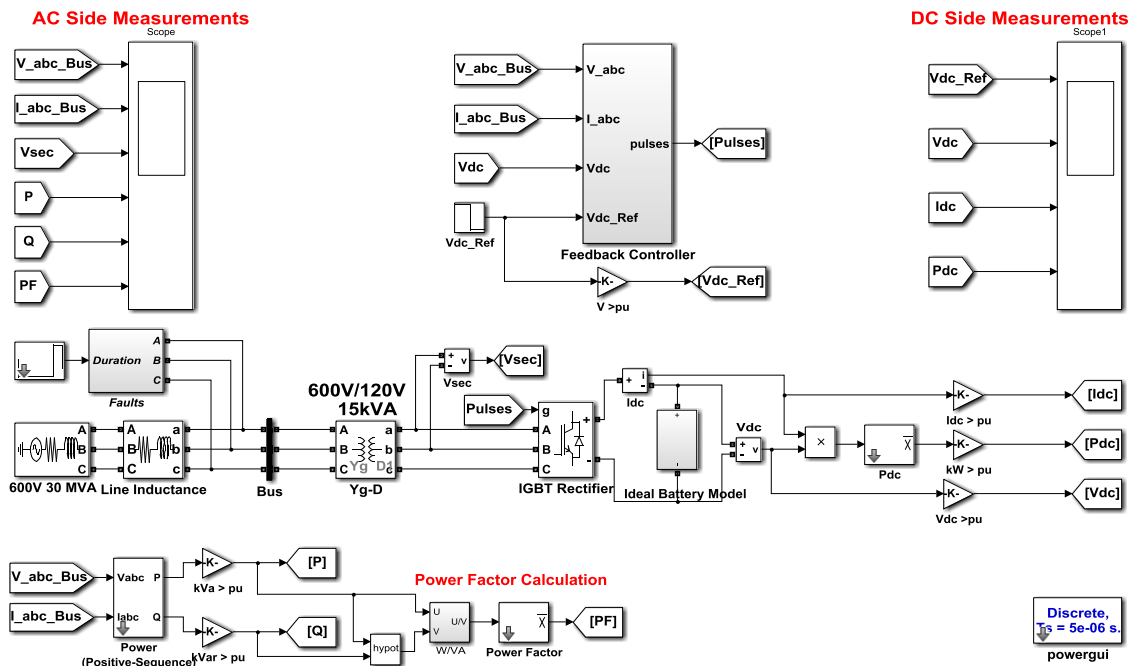


Figure 4.4: Three-Phase IGBT Rectifier System Model.

4.2 Three-Phase AC-DC Matrix Converter System Modelling

Similar to section 4.1, but in this case two ideal IGBTs are connected back-to-back with anti-parallel diodes to make one unit. This gives the matrix converter capability of bi-directionality power flow. SVPWM technique as discussed in Chapters 3.4 and 3.4.1 is used in the control system to generate the pulses for the 6 IGBT switches. The other switches are used for feeding the power back to the grid. Switches S1 (+ and-) and S7 (+ and -) are connected to phase A, S2 (+ and-) and S8 (+ and-) are connected to phase B and switches S3 (+ and-) and S9 (+ and-) are connected to phase C respectively as shown in Figure 4.5. . System parameters used in system modelling are provided in Appendix A, where the battery is considered as a constant voltage source assuming ideal conditions with no power losses. The modelling of the full EV battery with it specifications (Matlab model in Appendix B) is beyond the scope of this thesis work.

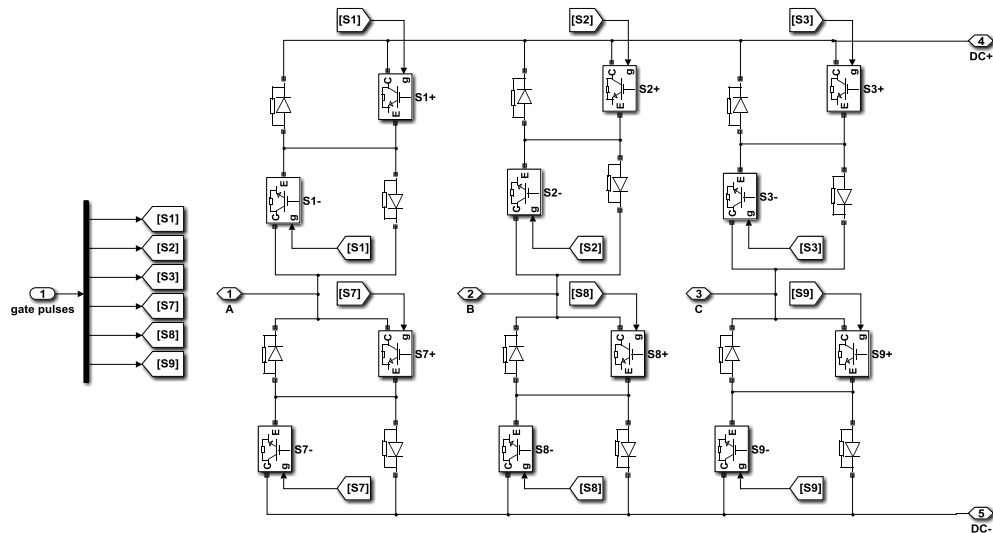


Figure 4.5: Matrix Converter Rectifier Block

As mentioned in Chapters 3, SVPWM method is used to generate gate pulses for the six switches in the matrix converter model. The three switches of the upper leg of the rectifier receive the PWM trigger signals and the lower leg of the switches receive the complementary gate signals in order to operate two switches in the same leg for the same phase. Figure 4.6 shows the developed model for SVPWM in MATLAB Simulink.

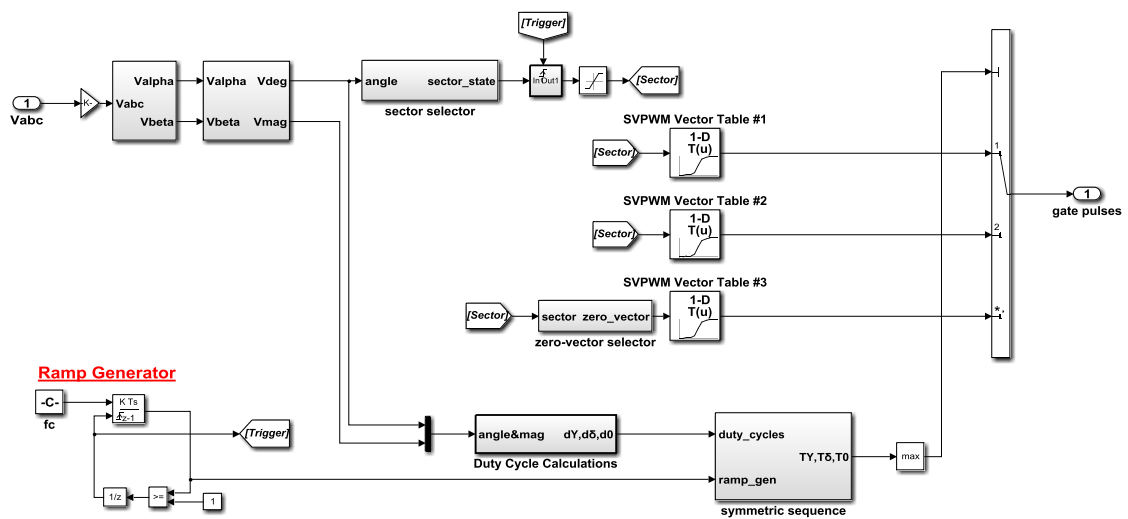


Figure 4.6: SVPWM Generator.

The three phase voltages (V_{abc}) from the sine generator are taken as reference voltages and converted to V_{α} and V_{β} components using Clarke's (abc to $\alpha\beta$) transformation:

$$v_{abc}(t) = \frac{3}{2} \begin{bmatrix} \frac{2}{3} & 0 \\ -\frac{1}{3} & \frac{\sqrt{3}}{3} \\ -\frac{1}{3} & -\frac{\sqrt{3}}{3} \end{bmatrix} \begin{bmatrix} v_{\alpha}(t) \\ v_{\beta}(t) \end{bmatrix} \quad (4.6)$$

The magnitudes and angles of the resultant voltages are found using Cartesian to Polar transformation. This angle in degrees (between -180° and 180°) is used to generate sectors from 1 to 6 as shown in Figure 4.7.

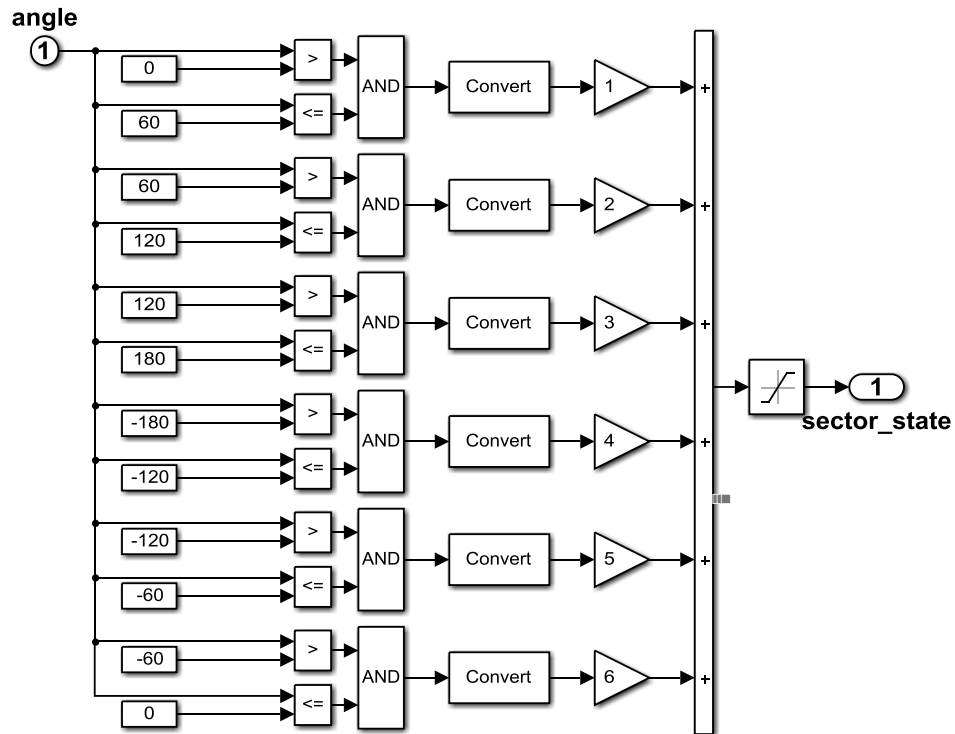


Figure 4.7: Selection of Sector State.

The timing vectors for the duty cycles are calculated using Equations 3.32 to 3.34 and its model is shown in Figure 4.8.

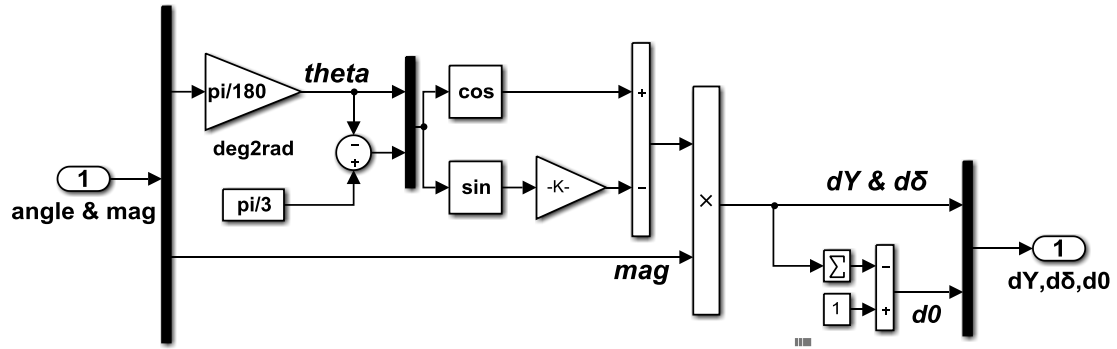


Figure 4.8: Duty Cycle Calculator.

These duty cycles are used in symmetric sequence as explained in section 3.4.1 and compared with a ramp signal to obtain the timing sequence for the vectors that can be seen in Figure 4.9.

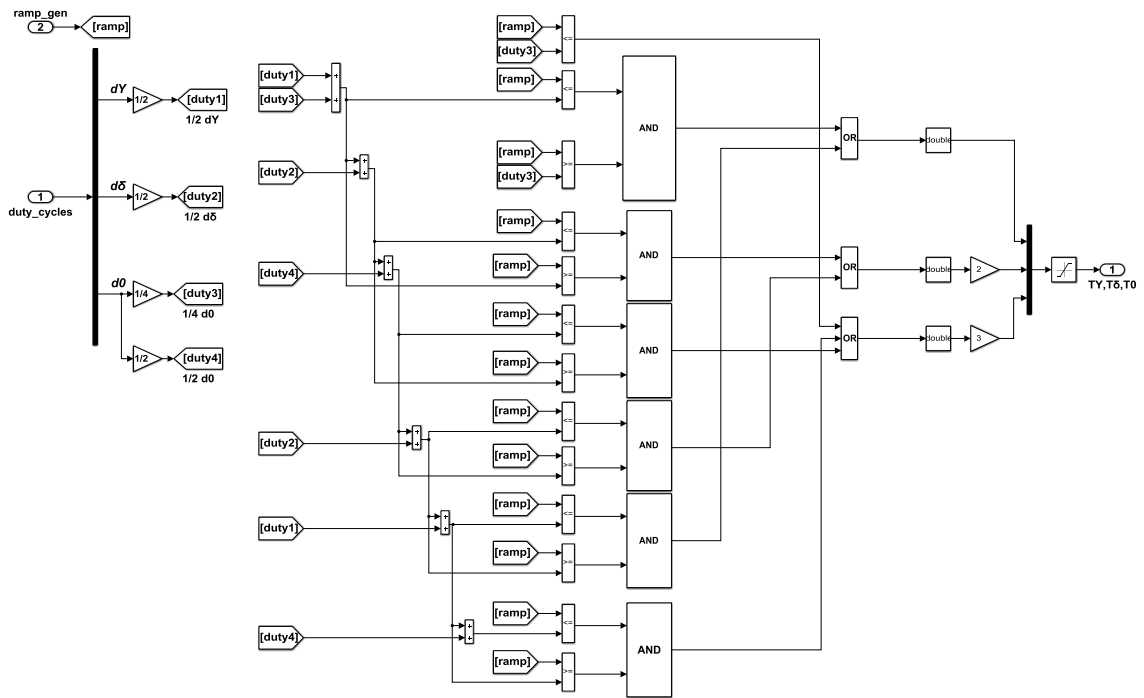


Figure 4.9: Symmetric Sequence for Switch Timings.

A look-up table modelled in Figure 4.6, developed from Table 3.2, is then referred to generate gate signals for the six IGBT switches in the Matrix converter. Between each active sector there is a zero vector state as shown in Figure 4.10 to create a dead time between each sector state, preventing short circuit. The complete system model is shown in Figure 4.11 where the battery is depicted as a constant voltage source as the modelling of the full EV battery with its specifications is beyond the scope of this thesis.

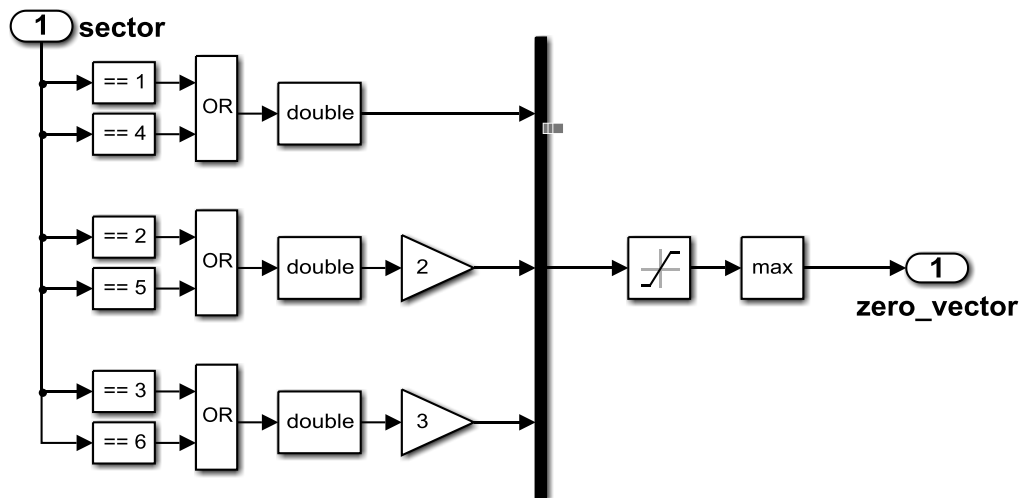


Figure 4.10: Zero Vector sector.

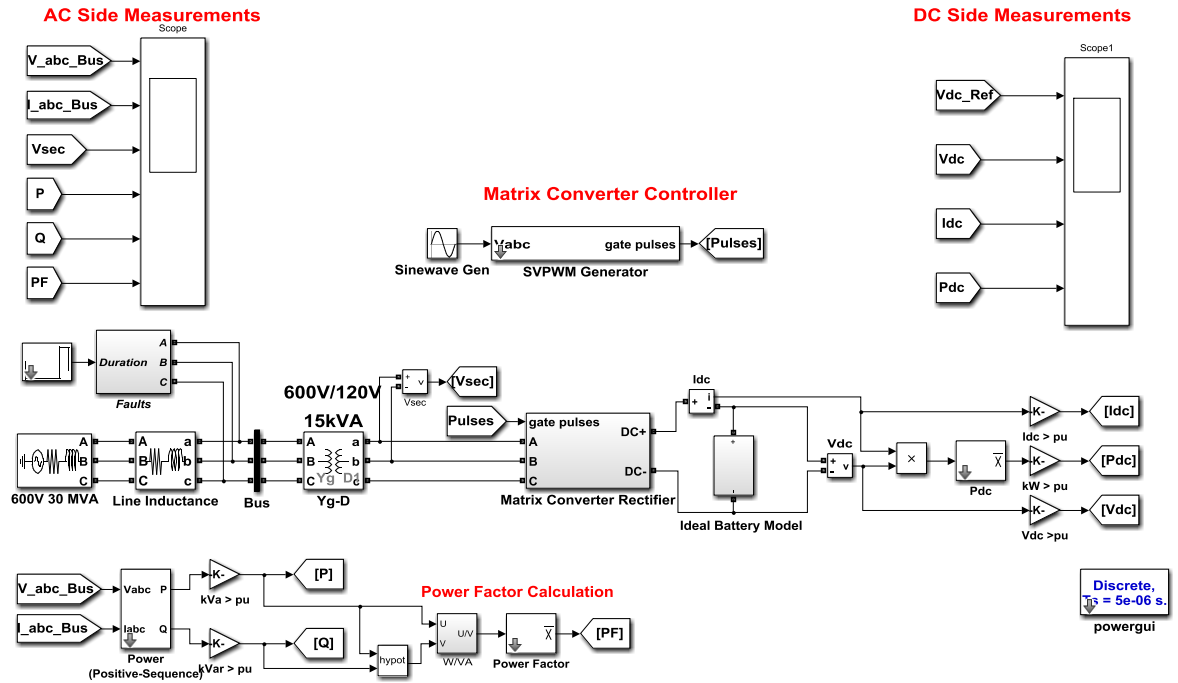


Figure 4.11: Three-Phase Matrix Converter Rectifier using SVPWM.

Chapter 5 Simulation Results and Analysis

5.1 Introduction

In this chapter, the performance assessment of each type of rectifier under steady state and dynamic condition is studied. In case of the IGBT rectifier configuration dynamic response of the system is simulated where a step change is applied to the output voltage V_{dc} . In case of the MC rectifier configuration, the dynamic response of the system is simulated where a step change is applied on the modulation index m , to control the amplitude of the output voltage V_{dc} . System parameters of the simulated models can be seen in Appendix A.

5.2 Steady State Analysis

The steady-state analysis is carried out on both system models considering various operating conditions and reference values of the system parameters. The entire system parameters are set to per unit (pu) values; the calculations can be seen in Appendix B.

5.2.1 Three-Phase IGBT Rectifier

Figure 5.1(a-d) presents the steady state response of the system using three phase IGBT rectifier. AC line voltages (V_{abc}) are shown in Figure 5.1 (a) respectively. Active power P of about 0.13 pu flows from the grid to the rectifier side as shown in Figure 5.1 (b). The reactive current component I_q is set to zero to keep the reactive power maintained at zero, thus achieving steady state within 0.1 s as seen in Figure 5.1 (c). Input power factor (PF) reaches steady state within 0.15 s after transient response at start-up. System start-up transient responses are due to the gains used in PI controllers and can be fine-tuned to reduce the overshoot responses and reach steady state faster. Soft switching techniques such as ZVS and ZCS can also be used to improve transient overshoots at system start-ups and reduce switching losses.

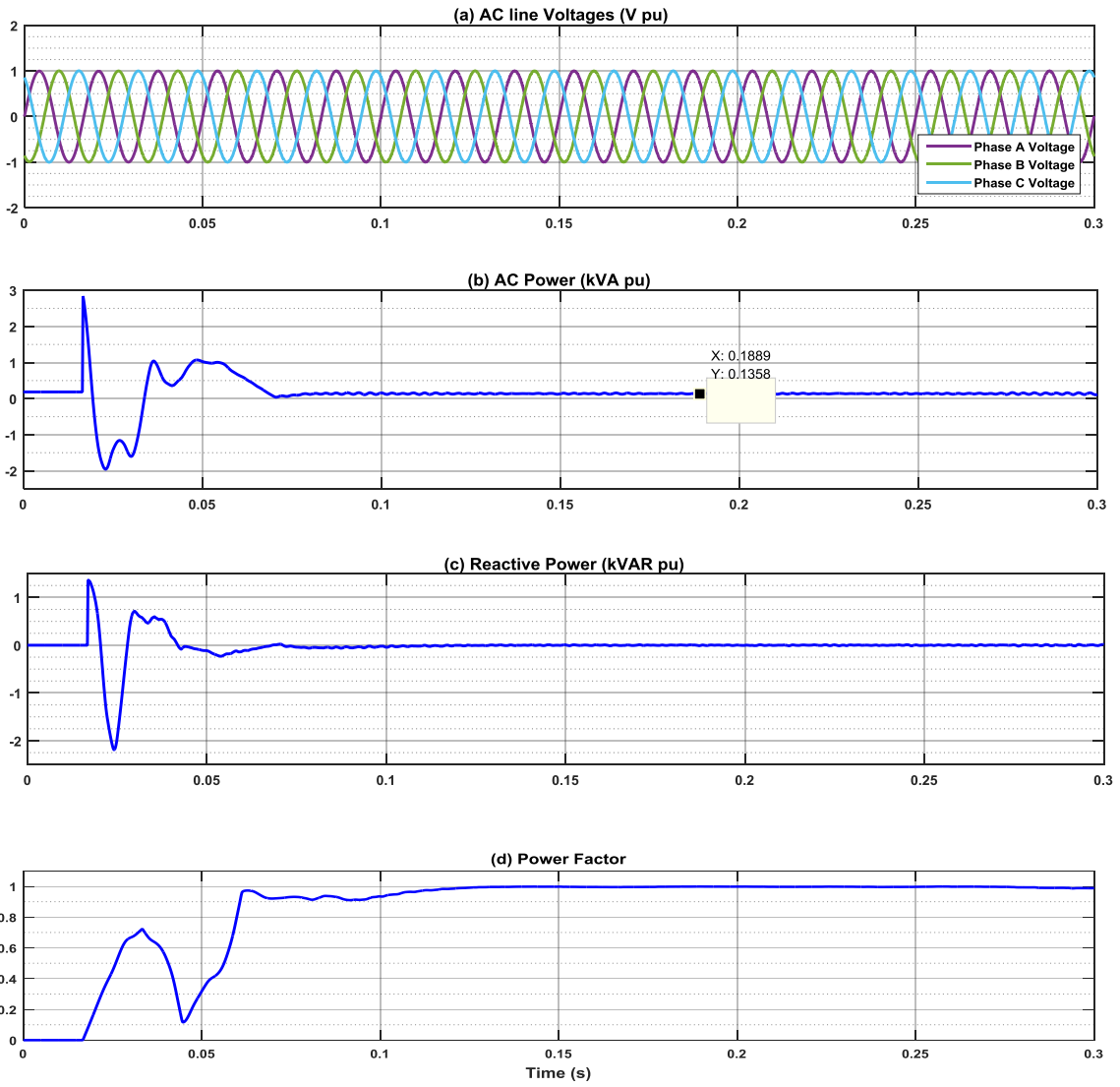


Figure 5.1 (a-d): Steady state response of the system at the AC side with three phase IGBT rectifier.

At the DC side, the output voltage V_{dc} , output current I_{dc} and output power P_{dc} are maintained at 1 pu as shown in Figure 5.2 (a-c). The system AC power P , reactive power Q , V_{dc} , I_{dc} and P_{dc} shows initial transient responses in the start-up but reach nominal operating values within 0.1 s.

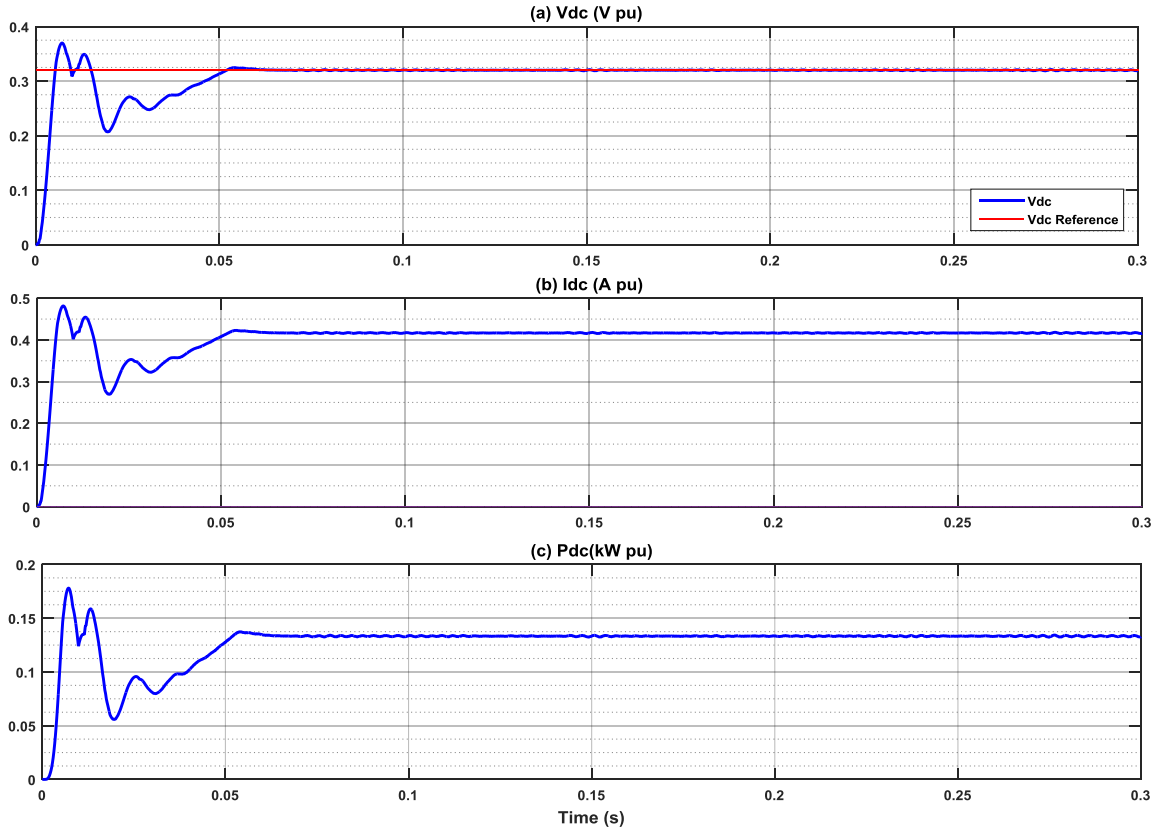


Figure 5.2 (a-c): Steady state response of the system at the DC side with three phase IGBT rectifier.

5.2.2 Three-Phase Matrix Converter

Figure 5.3 (a-f) presents the system results for MC as a rectifier. Active power P of about 0.16 pu flows from the grid to the rectifier side and a reactive power of -0.09 pu flows in the system as there is no control designed for the reactive power as shown in Figure 5.3 (d-e) respectively. This reactive power is indicative of the capacitance present at the input side of the grid and is supplying the reactive power.

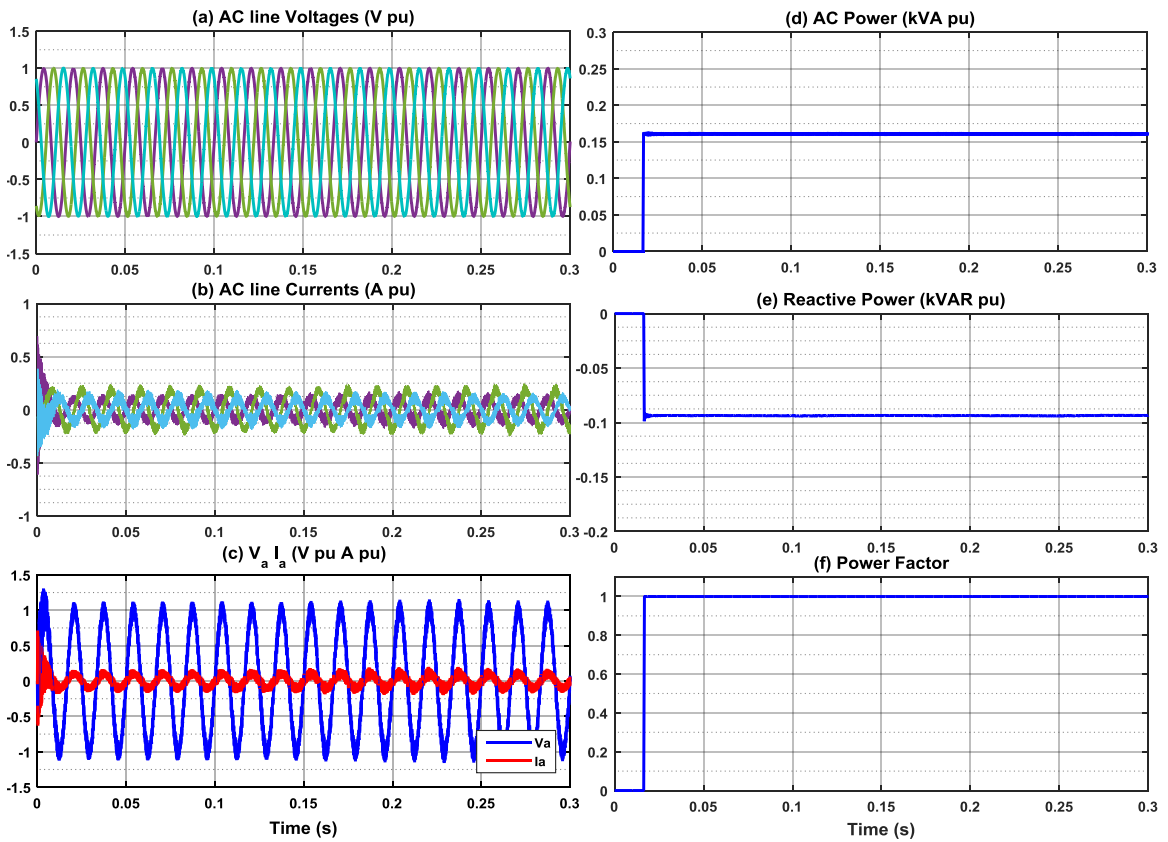


Figure 5.3 (a-f): Steady state response of the system at the AC side with three phase MC rectifier.

At the DC side, the output voltage (V_{dc}), output current I_{dc} , and power P_{dc} , are maintained at nominal values, allowing charging of the battery as shown in Figure 5.4 (a-c). The system AC power P , reactive power Q , V_{dc} and I_{dc} have transients in the start-up that reaches reference values within 0.02 s.

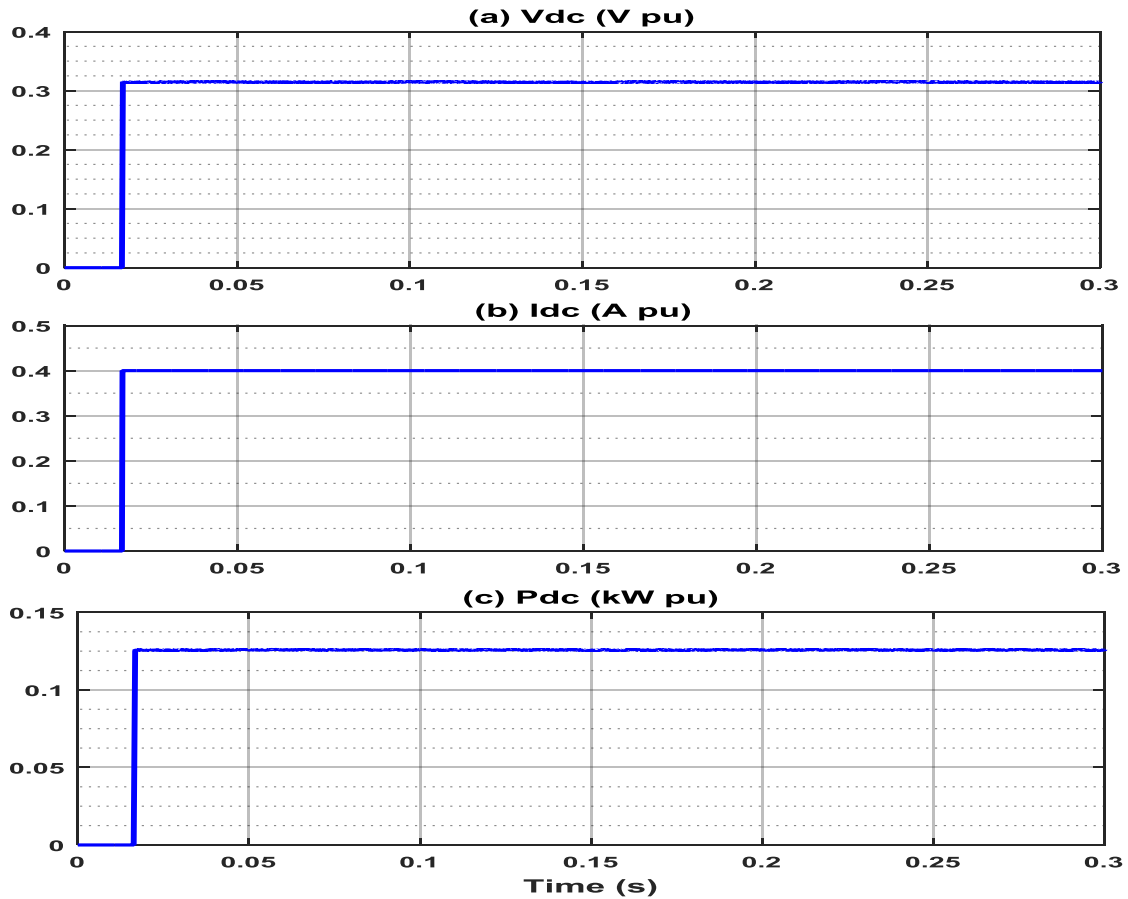


Figure 5.4 (a-c): Steady state response of the system at the DC side with three phase MC rectifier.

The bi-directional capability for V2G operation is evident in in Figure 5.5 (a), where a -0.4 pu I_{dc} shows the V_{dc} is maintained at nominal value (0.32pu) achieving a full battery power flowing back to the grid as shown in Figure 5.5 (c). The bi-

directionality of the system can be useful according to the system operating conditions and requirements.

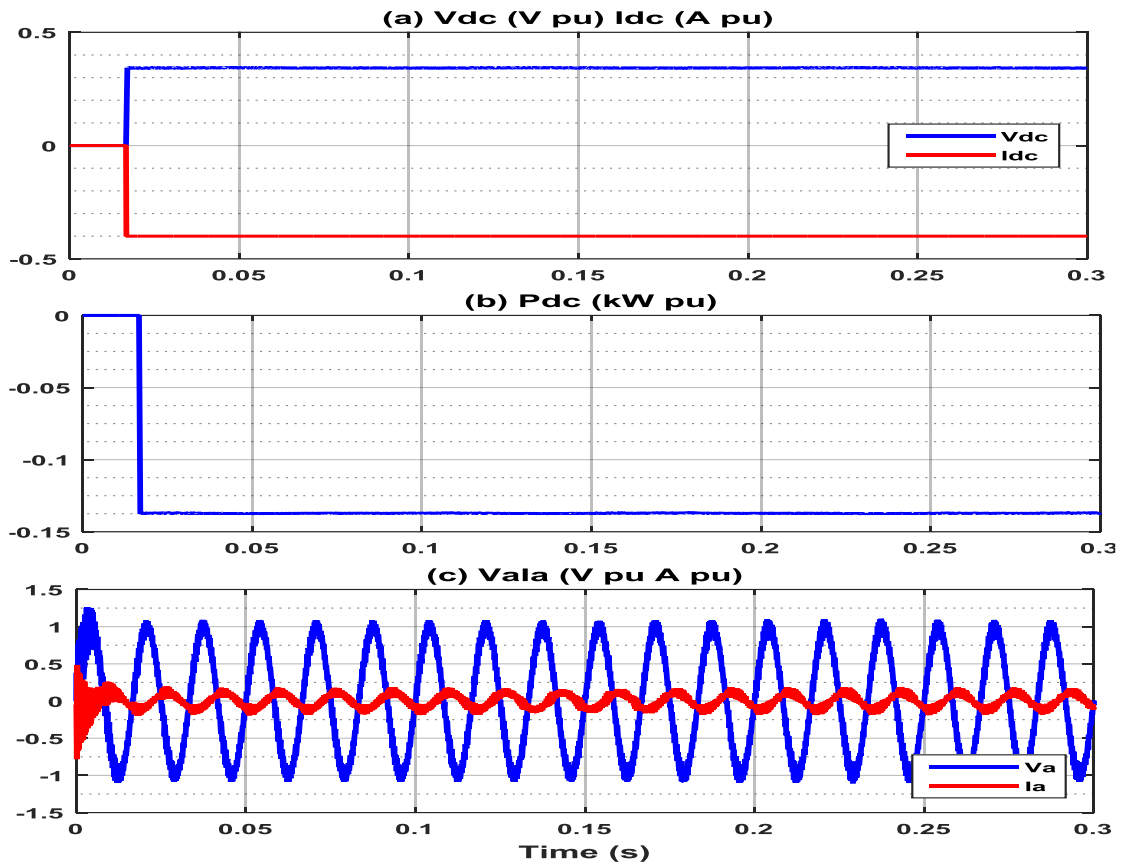


Figure 5.5 (a-c): Bi-directional power flow response of the system with three-phase MC based rectifier.

5.3 Dynamic Analysis

5.3.1 Three-Phase IGBT Rectifier

In this scenario, step changes are implemented on output voltage V_{dc} , output power P_{dc} and input power P . Applying the steps in these variables separately at different times, the system recovery capability from these disturbances are evaluated.

5.3.1.1 Step Change in DC Output Voltage

As seen in Figure 5.6, the system reaches reference value after transient within 0.1 s. A step change of 0.18 pu (step up from 48 V to 75 V) is applied on V_{dc} from 0.3 s to 0.6 s as shown in Figure 5.6 (a). This is done to show the system response to suit the battery with varying capacity. The actual V_{dc} follows reference value closely and settles in less than 0.05s. This affects the I_{dc} that follows the change in V_{dc} . The power demand is increased (about 17%) as well during the step change and is evident in the Figure 5.6 (d). Disturbance in AC power is seen at instances when the output voltage (V_{dc}) is changed. AC power goes up to 1 pu during the sudden step change due to increase in current and power demand of the load and goes down during the step down because the current and power demand of load decreases until it reaches steady state. The reactive power is maintained at zero as set by the current component i_q in the controller as shown in Figure 5.6 (e). The power factor (PF) shows minor disturbance of 0.01 at 0.3 s when the step change is applied and quickly recovers back to unity PF. When the step is removed,

due to sudden drop in active power the PF drops down to about 0.8 and recovers back to unity within 0.05 s after the step change is removed as shown in Figure 5.6 (f). The instant when the voltage is stepped down at the end 0.6 s, depicts the system response to a possible voltage sag that may occur due to a dead cell in the battery pack. In practice, this is not expected to happen, however this test shows that the controller for this system is robust to handle sudden changes in set-points of the battery.

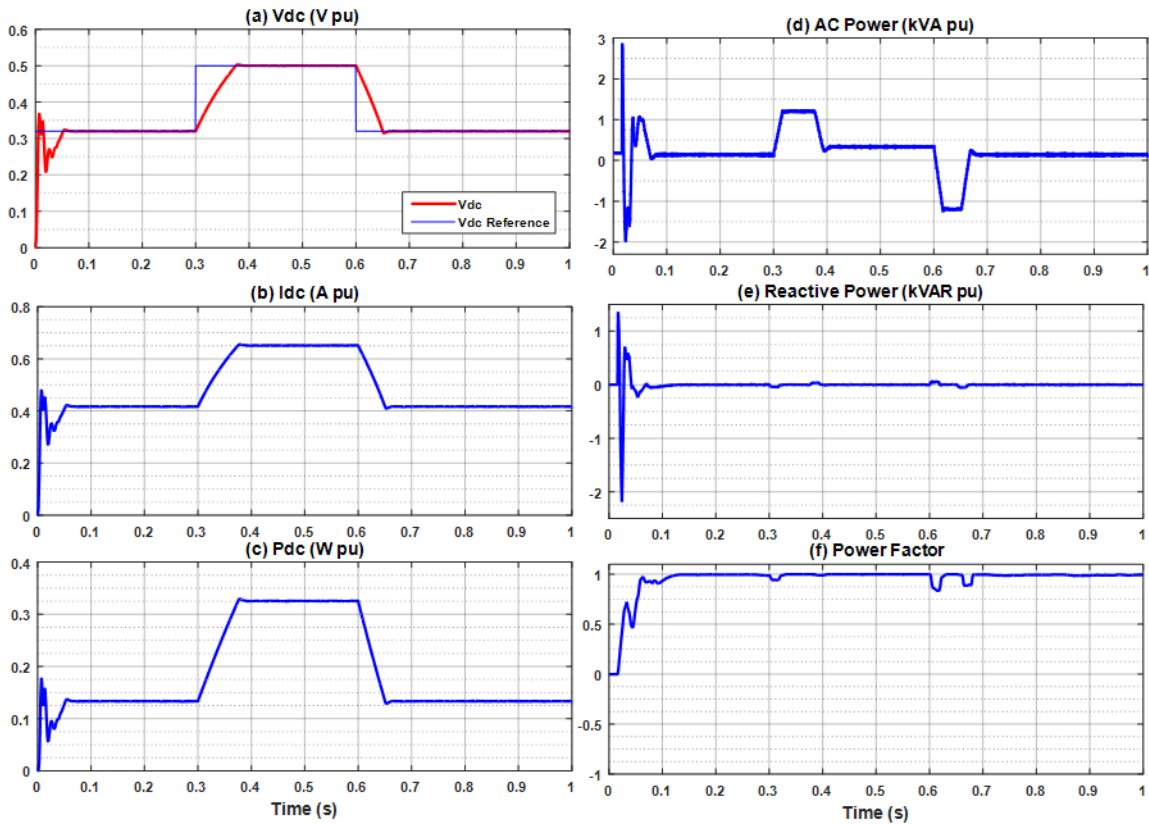


Figure 5.6 (a-f): System response to a step change applied to DC output voltage.

5.3.1.2 Step Change in Output Power

In Figure 5.7 (a-f), the system reaches reference value after transient in 0.05 s. A step change of about 0.13 pu is applied on P_{dc} at 0.3 s. This is to represent the system can meet more power demand in case the battery capacity is increased. Instead of changing the entire charging system to meet another vehicle battery specifications, this system is designed to provide up to maximum of 15 kW of power if the battery specifications are upgraded. The actual V_{dc} shows a very slight drop in the voltage and quickly recovers back to 1 pu within 0.05 s and is expected as the battery is set to constant voltage of 0.32 pu. This change in power affects the I_{dc} that responds with following the change in P_{dc} to meet system load power demand. This increase in load power demand results in an active power transient. The load demand is met by the AC power side which increases by 17% after the step change occurs. These results confirm the decoupled feature of the reactive power at the supply side as the reactive power remained constant at 0 pu as regulated by the reactive current control loops and can be seen in Figure 5.7 (e). The power factor (PF) shown in Figure 5.7 (f) have a transient response and goes below unity by 1% in response to the step change due to sudden change in active power. The transition is observed as very rapid and power factor settles back to unity within less than 0.05 s.

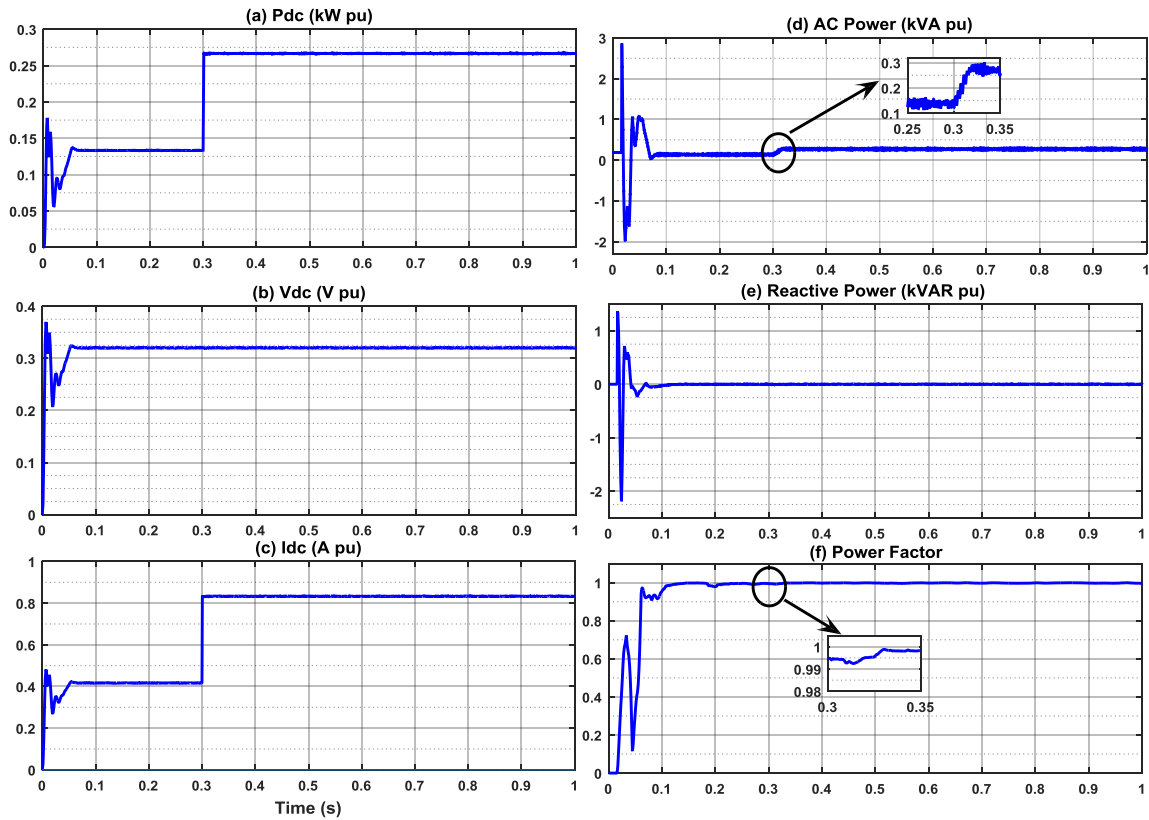


Figure 5.7 (a-f): System response to a step change applied to the DC output Power.

5.3.1.3 Step Change in Reactive Power

Next, as seen In Figure 5.8 (a-f), the system reaches reference values after transient within 0.1 s. A step change in reactive power is applied from 0.3s to 0.6 s. The active power is seen to be constant at 0.13 pu and shows no response to the change in reactive power confirming decoupling operation as shown in Figure 5.8 (a-b). P_{dc} , V_{dc} and I_{dc} results as shown in Figure 5.8 (c-e) are almost unaltered as expected and confirm the decoupled operation of the active and reactive loops. The power factor (PF) response

goes from unity to almost 0.2 depicting capacitive power factors before returning back to unity at the end of the step change. This is in response to the step change due to sudden increase in system's reactive power.

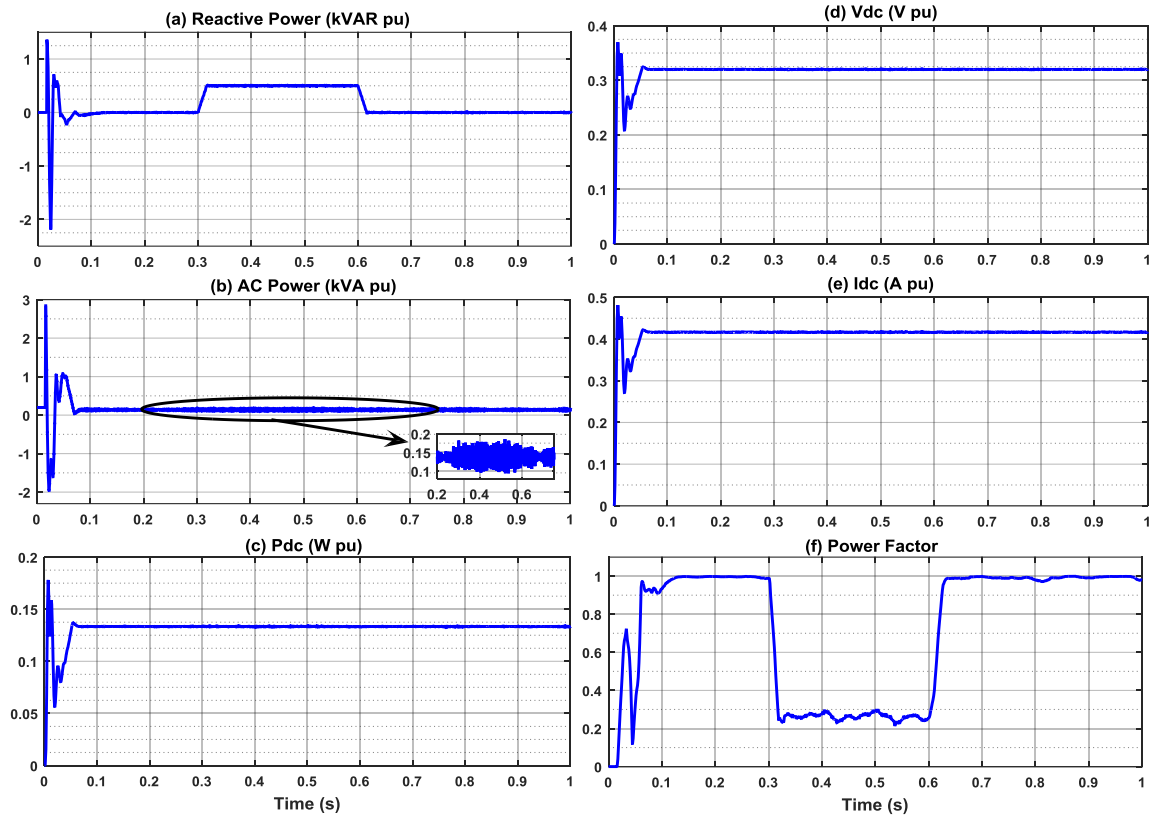


Figure 5.8 (a-f): System response to a step change applied to the reactive power Q.

5.3.2 Three-Phase Matrix Converter

In the case of matrix converter, step changes are applied in the output voltage (V_{dc}) and current (I_{dc}) as well as current reversal is carried out to depict the bi-directionality power flow functionality of the MC. The system's ability to recover from these disturbances are also studied in this chapter.

5.3.2.1 Step Change in Output DC Voltage

As seen in Figure 5.9 (a-d), output DC voltage (V_{dc}) gradually is stepped up from 0 pu to 1 pu in steps of 0.1 s in response to change in modulation index m , from 0 to 0.866. The response is almost linear showing that an increase in modulation index increases the output voltage (V_{dc}). The range of output voltage that can be achieved is wide, from 0 pu (0V) to 1 pu (150V). This comparison between the modulation index and the output voltage for matrix converter is also validated for single phase matrix converter simulation results carried out in [68]. There is no change in DC current I_{dc} as it is kept constant and settles down from transient state to 1 pu (40A) in less than 0.02 s. For The input phase A voltage and current $V_a I_a$, it is seen that the phase A voltage remains constant at 1 pu but the current shows response to change in V_{dc} . This change occurs as the output load demand tracks the V_{dc} that is reduced in steps, the AC current reduces as well in similar pattern to provide lower power from the utility grid in order to meet the required output power demand. This test shows close similarity to the simulation results carried out in [21], confirming that during charging at constant

current, the battery voltage increases and in order to meet the increased power demand, the currents at the grid side will increase as well.

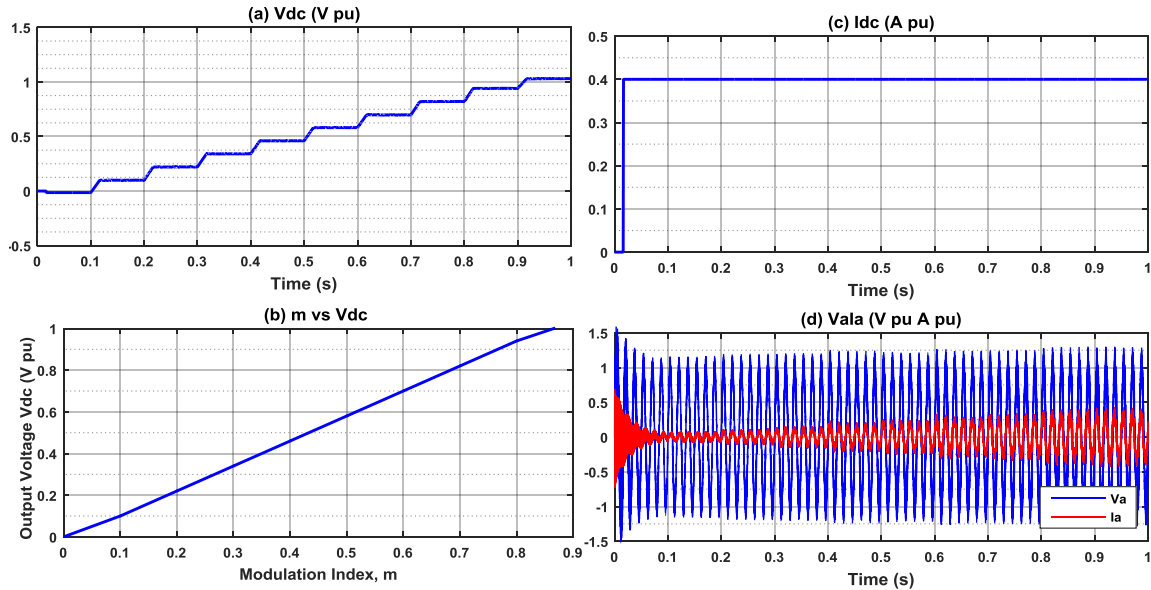


Figure 5.9 (a-d): System response to a step change applied to DC output voltage.

5.3.2.2 Step Change in Output DC Current

As shown in Figure 5.10 (a-d), initially the output current I_{dc} is set to minimum 0 pu (0A) and is increased to 1 pu (100 A) in steps of 0.1 s. The V_{dc} is kept constant at 1 pu and remains constant throughout the step change as set by the modulation index. The effect on the PF is not significant when the output current I_{dc} is increased, MC tries to maintain the PF close to unity as shown in Figure 5.10 (b). The step change in I_{dc} affects the angle between the AC input voltage and current resulting in delayed angle between them causing reduction in the displacement factor. A PF correction circuit can be

implemented to calculate this delay angle beforehand and applied to the input current in order to correct the displacement angle between the input phase voltage and current to be in phase for a unity PF. This test validates the practical implementation of three-phase AC-DC matrix converter which was built and tested in [27].

Again, it is seen that for V_a, I_a in Figure 5.10 (d), that the phase A voltage remains constant at 1 pu but the current shows response to change in I_{dc} as expected. This change occurs as the output load demand tracks the I_{dc} that is increased in steps, the AC current increases as well to provide higher power from the utility grid in order to meet the required output power demand. This step response of the current closely relates to the simulation results carried out in [21] to show that input current I_a increases or decreases with battery current still managing to maintain the PF close to unity. Though, in practical work, this change in battery current is not expected and is performed to show the system is very robust without any feedback control loops and can handle sudden variations in output current.

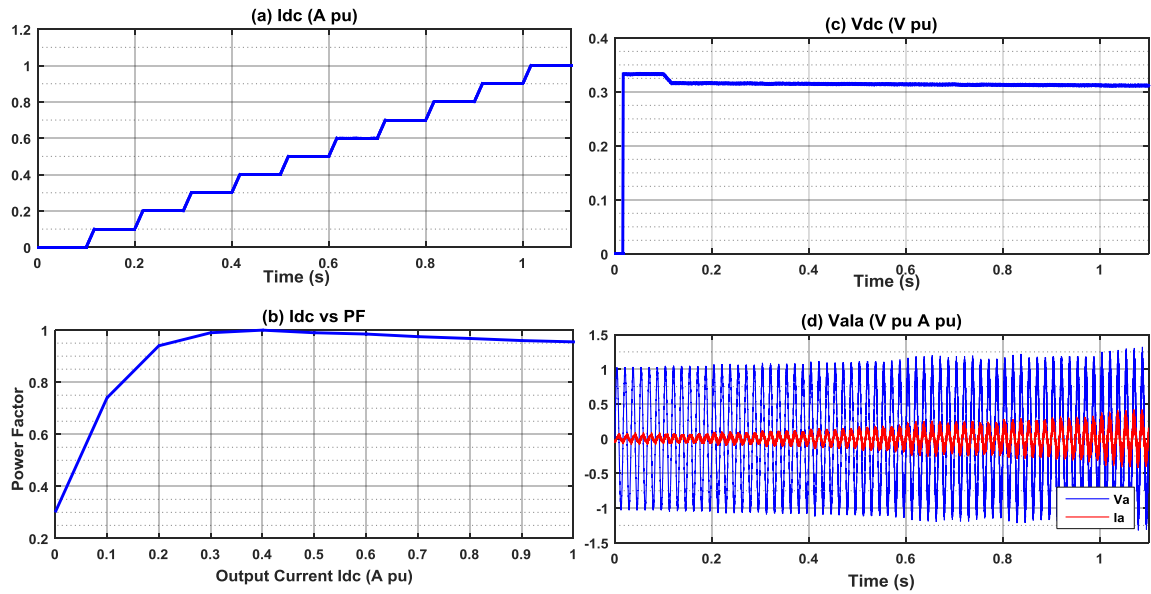


Figure 5.10 (a-d): System response to a step change applied to DC output current.

5.3.2.3 Vehicle to Grid (V2G) Operation

As discussed earlier, the MC is capable of bi-directional power flow in the system because of the two back-to-back connected IGBT in its configuration. The performance of the system during power transfer back to the grid is studied by providing a negative step in I_{dc} of -0.4 pu at 0.3 s and the system response is studied as represented in Figure 5.11 (a-f).

The V_{dc} quickly reaches nominal value of 0.32 pu after short period of transient response and at 0.3 s there is a slight increase in V_{dc} in response to the negative I_{dc} . This response is also reflected in the output power where the power demand goes from

positive to negative as well to show there is a power flow reversal and the bidirectional switches in MC are used to feed back the power back to the grid. The negative output DC current (I_{dc}) step response and the shift of 180° between the input phase A voltage and current (V_{a1a}) confirms that the power is flowing from the battery back to the grid as shown in Figure 5.11 (d)).

Active power responds similarly to meet the required demand for the output in the charging condition before the current becomes negative. The negative response in the active power shows the power is flowing back to the grid. The power factor of the system is maintained at unity until the step in the output current I_{dc} is applied. The PF goes down to almost 0.7 when the power flows back to the grid. The reduced PF when the power flow is reversed is due to presence of input filter capacitors. The bi-directionality power flow of the matrix converter is confirmed with simulations results in [21] and further varified by experimental results in [27].

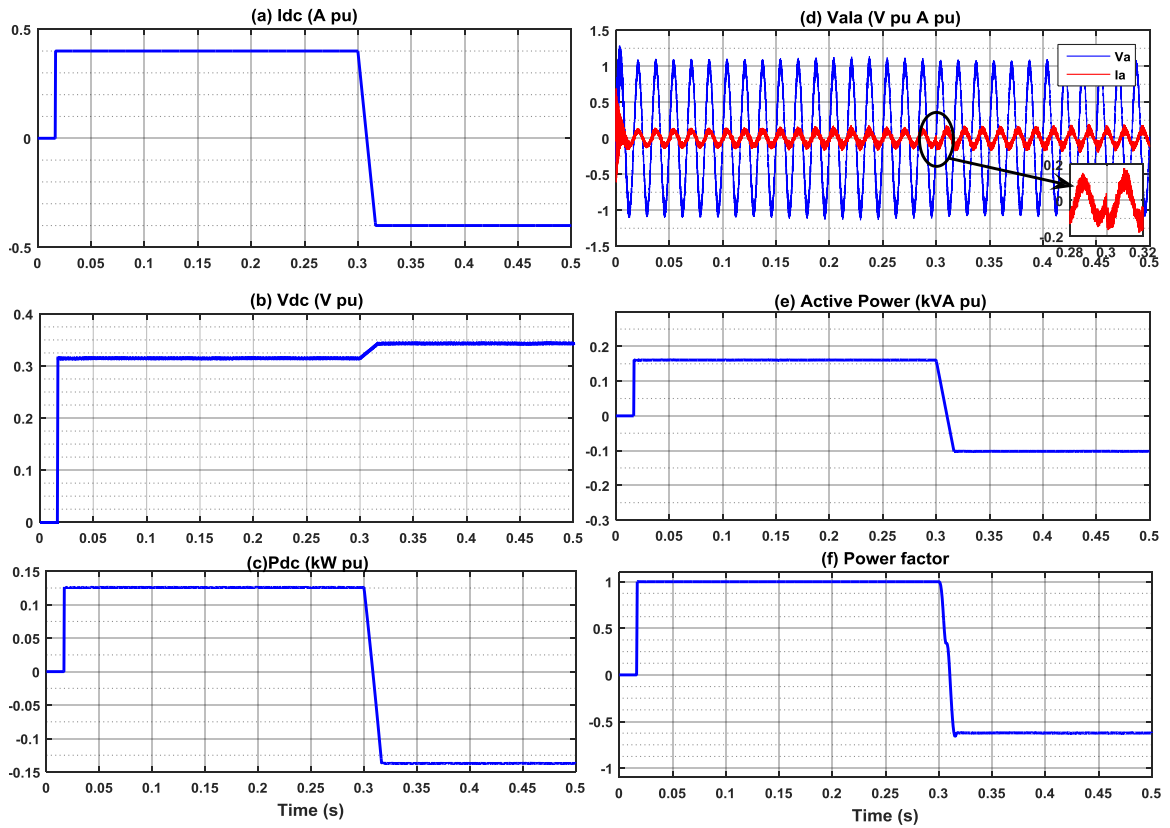


Figure 5.11 (a-f): V2G operation using MC based rectifier configuration.

5.4 Harmonic Analysis

Harmonics are sinusoidal voltages and currents that have frequencies that are whole multiples of the system frequency (60 Hz). The presence of voltages at other frequencies needs to be avoided for systems to have minimum harmonic contents. The effects of harmonics include system malfunctions, losses, overheating, overloading the power distribution network and poor input power factor. The designed converters add harmonic content in the system and are analyzed.

The Figure 5.12 (a-b) presents the harmonic spectrum of the three phase IGBT rectifier at the secondary side of the transformer and the output DC voltage (V_{dc}). The voltage harmonic spectrum shows a total harmonic distortion (THD) of 65.28 %, adding very high harmonic content to the grid.

The voltage harmonic spectrum for the output DC voltage adds a THD of 18 % making this system a source of high harmonic content that would affect the battery of the EV.

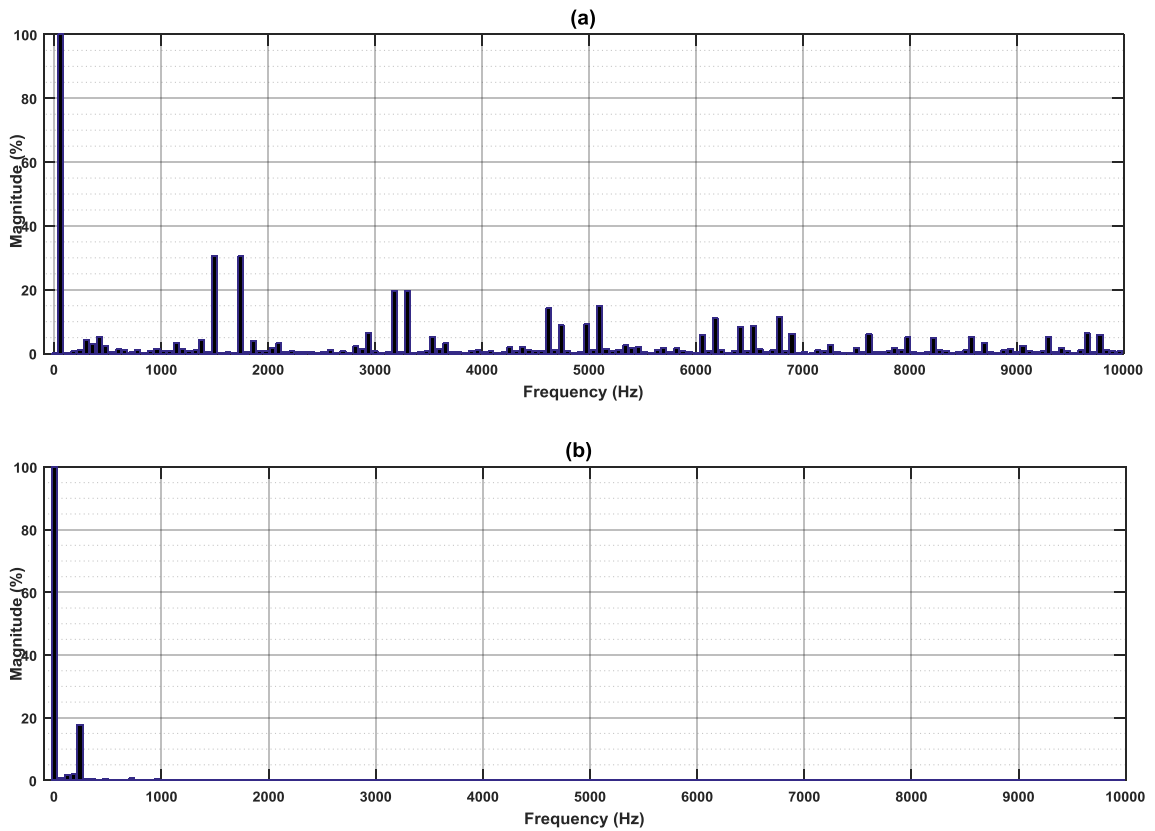


Figure 5.12 (a) & (b): Harmonic spectrum of V_{sec} (Voltage at the secondary side of the transformer) & V_{dc} (Output DC voltage) for IGBT rectifier respectively.

In contrast, the voltage harmonic contents added by the MC based rectifier to the grid shows a THD of 3.88 % at the secondary side of the transformer as shown in Figure 5.13 (a-b). The SVPWM uses high switching frequency to reduce the harmonics in the system without much bulky filters.

The output DC voltage harmonic content is 11.6%, adding to the THD but is comparatively less than IGBT based rectifier configuration. This result match the theoretical and experimental work carried out in [26]. The significant harmonic components are around the switching frequency and almost no low-order harmonics. However, the converter designed for the system would have higher harmonic content compared to the one tested in [26] as there are no RC filters present in the system.

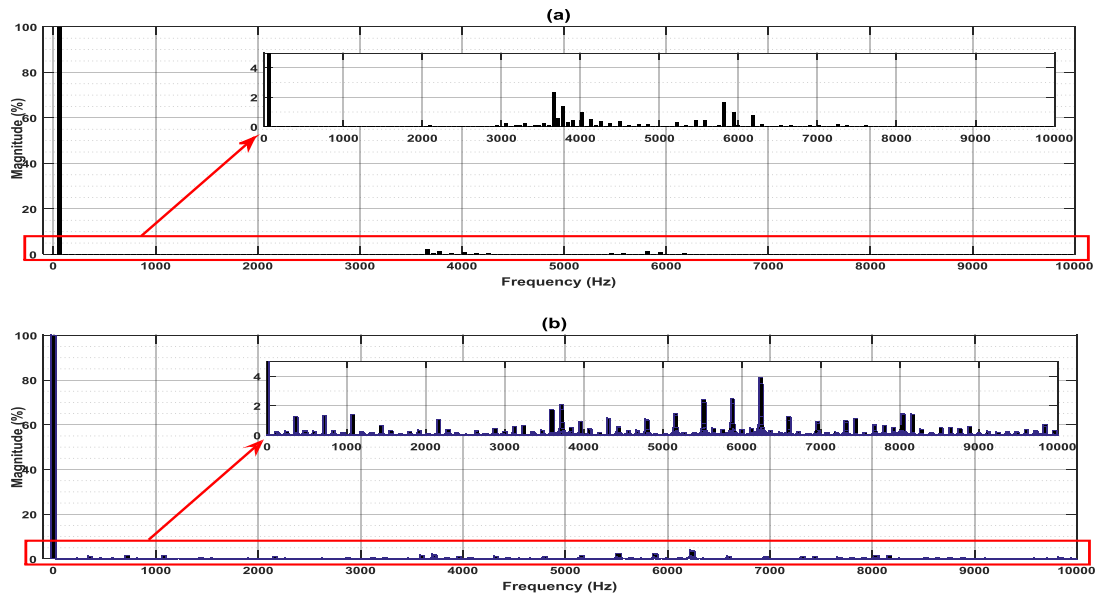


Figure 5.13 (a) & (b): Harmonic spectrum of V_{sec} (Voltage at the secondary side of the transformer) & V_{dc} (Output DC voltage) for MC rectifier respectively.

Chapter 6 Fault Analysis

6.1 Introduction

Power systems operate in stressful conditions and its reliability is of paramount importance to maintain integrity in the network and stability through the power system. In order to have a stable power system, the system is tested under fault conditions and the results are analyzed to know whether the system can clear the fault and return back to normal working conditions without human intervention. Events like lightning strikes, equipment failures can cause faults in the system to experience voltage sags, overshoots in voltages and currents and momentary interruptions. The system designed to be protected against these situations can increase reliability of the power system. If the faults are not cleared quickly, many equipment in the system can permanently be damaged due to high surges of currents and voltages and can significantly add to the cost of maintenance.

Balanced faults include three-phase faults and three-line-to-ground (TLG) faults. Unbalanced faults include single-line-to-ground (SLD) fault, line-to-line (LL) fault and double-line-to-ground (DLG) fault. Studies of the system performance under these faults are a very important part of the system analysis. Momentary interruption is one of the fault conditions, applied on the system for short intervals and the two modelled systems

in this thesis are put under number of interruption faults and the system response is studied.

6.2 Three-Phase IGBT Rectifier

Momentary interruptions occurs when any input phase voltages goes below 10% of the magnitude between 0.5 cycles to 3 s. SLG, DLG and TLG faults are simulated in MATLAB Simulink and the system response and recovery is observed. For implementation, starting conditions are set for active power of 0.13 pu, the reactive power is fixed at zero and the DC output voltage (V_{dc}) is fixed at 0.32 pu. The analysis is conducted for AC voltages and currents (V_{abc} and I_{abc}), active and reactive power (P and Q), DC output voltage (V_{dc}) and DC output current (I_{dc}) as well as the power factor (PF).

6.2.1 Single-Line-to-Ground Fault

A SLG fault in phase A is introduced at 0.5 s for 6 cycles (100 ms). Figure 6.1 (a-b) shows phase A voltage and current for this fault durations. During the fault, input phase A voltage becomes almost zero and high amplitude fault current flows which oscillates during the fault. Both voltage and current settles down almost immediately to nominal values after the fault is removed.

At 0.5 s, when the fault is introduced, AC Power shows transient overshoots between 0.4 pu and -0.3 pu and recovers to reference value within 3 cycles when the fault is removed as shown in Figure 6.1 (c). Similarly reactive power shows maximum

transient overshoot between 0.25 pu and -0.1 pu before returning back to zero in 3 cycles after the fault is removed.

The output voltage V_{dc} , current I_{dc} and power P_{dc} all responds to the fault and oscillates continuously until the fault is removed and the reference values are attained within 3 cycles as shown in Figure 6.1 (e-g). The DC voltage V_{dc} goes between 0.34 pu and 0.3 pu with a mere 2% overshoot when the fault is applied. I_{dc} oscillates during the fault between 0.44 pu and 0.4 pu with an overshoot of 4% before settling to rated value. P_{dc} overshoots to about 2.5% of nominal value and oscillates before reaching nominal value. The system power factor goes down to less than 0.5 as there is a sudden drop in AC power and recovers back to nominal value within 4 cycles after the fault is cleared. SLG fault affects the system momentarily and the system responds well under this type of fault.

The tests were carried out for various numbers of cycles, all showing results similar to the SLG fault test for 6 cycles.

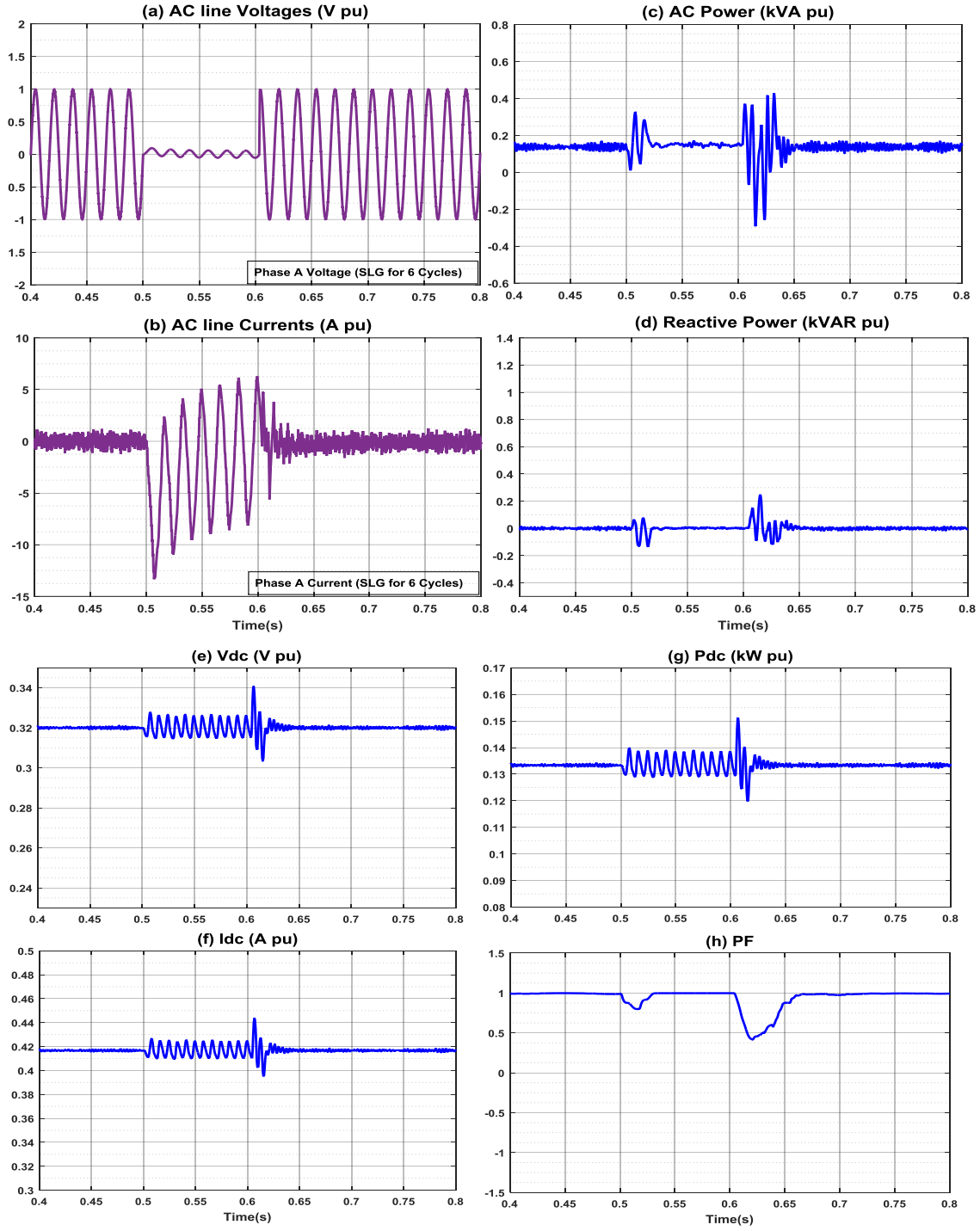


Figure 6.1 (a-h): System response to SLG fault introduced for 6 cycles with IGBT based rectifier.

6.2.2 Double-Line-to-Ground Fault

A DLG fault is introduced in phases A and B at the AC input at 0.5 s for 6 cycles.

The momentary interruption bring down the AC voltages for phase A and B to about 5.5% of the rated value and high currents oscillates until the fault is cleared as shown in Figure 6.2 (a-b). Figure 6.2 (c) shows the AC power at start of the fault goes between 0.35 pu to about -0.1 pu and as the fault is cleared AC Power shows transient overshoots between 0.55 pu and -0.4 pu and tries to recover to reference value within 4 cycles once the fault is removed. Similarly, reactive power in Figure 6.2 (d) shows transient response between 0.3 pu and -0.2 with overshoot of 30% before returning back to zero in 4 cycles. Reactive power is decoupled from the active power whilst during or after the fault the system tries to recover the reactive power back to zero.

At the DC side, V_{dc} oscillates maximum between 0.35 pu to 0.3 pu with an overshoot of 3% as shown in Figure 6.2 (e). The V_{dc} returns back to rated value after the fault is removed within 3 cycles. I_{dc} and P_{dc} follows similar response to V_{dc} until the fault is removed as shown in Figure 6.2 (f-g). I_{dc} oscillates during the fault and overshoots between 0.45 pu and 0.39 pu with an overshoot of 5% before settling to rated value within 0.05 s. P_{dc} overshoots to about 4% of nominal value and oscillates before reaching nominal value. The power factor drops down to 0.4 before returning to 1 within 4 cycles of fault removal.

The tests were carried out for various numbers of cycles, all showing results similar to the DLG fault test for 6 cycles.

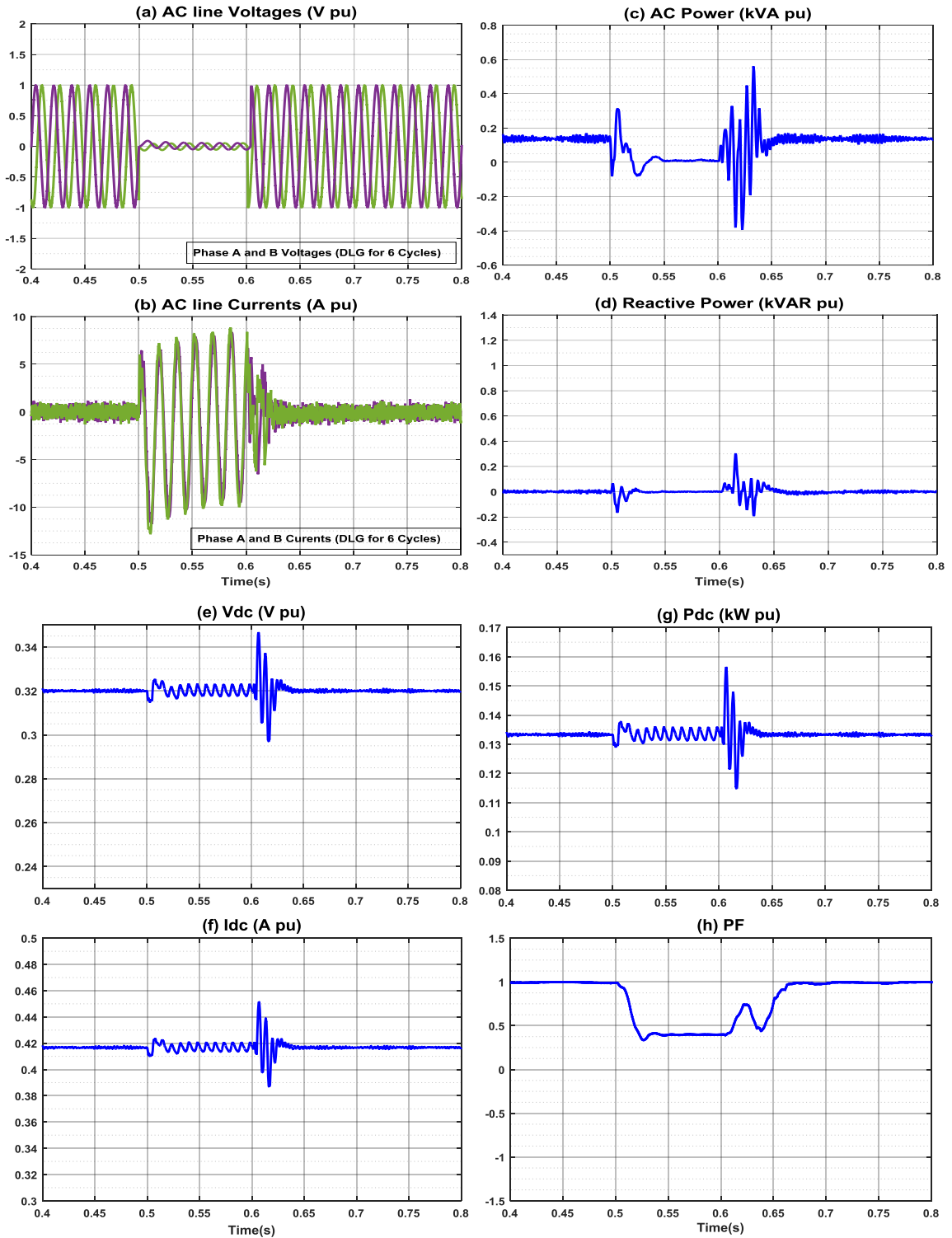


Figure 6.2 (a-h): System response to DLG fault introduced for 6 cycles with IGBT based rectifier.

6.2.3 Triple-Line-to-Ground Fault

A TLG fault is introduced in all phases A, B and C at the AC input at 0.5 s for 6 cycles and 12 cycles respectively. Figure 6.3 (a-h) represents the AC voltages, AC currents for all three phases, system active and reactive power (P and Q), DC output current I_{dc} and DC output voltage V_{dc} as well as power factor response during this fault. The momentary interruption results in the AC voltages for all phases to reduce down to about 5.5% of the rated value and high currents are observed that oscillates until the fault is cleared. The system behaves as a shock absorber for protection under this fault and the voltages and currents are seen as more stable with minimum oscillations. Input AC power at start of the fault responds with transient response between 0.2 pu to about -0.15 pu and as the fault is cleared the AC power settles down to rated value within 6 cycles after transient overshoots of 0.75 pu and 0.6 pu in response to fault clearing after 6 cycles and 12 cycles respectively. Reactive power during and after the fault tries to follow the system set response of 0 pu after a transient response. This transient response has a peak value of 0.3 pu for 6 cycles and 1.3 pu for 12 cycles when the fault takes place. When the fault is cleared for 6 cycles the system tries to recover the reactive power back to zero within 4 cycles but when the fault is cleared for 12 cycles test, the system takes 8 cycles to recover back to nominal value.

At the DC side, for 6 cycles duration of fault, V_{dc} decays down from 0.32 pu to 0.285 (48 V to 42.75 V) before returning back to nominal value after a transient overshoot of 3.5% within 3 cycles after fault removal. During 12 cycles of fault period,

V_{dc} decays down to 0.265 pu and recovers back to 0.32 pu within 3 cycles after the fault is cleared as shown in Figure 6.3 (f). The decay response is similar for I_{dc} , 0.37 pu during 6 cycles and 0.35 pu during 12 cycles of introducing the fault. I_{dc} responds with a minor disturbance overshoot of 1% before the fault is cleared and recovers back within 3 cycles. After the fault is introduced, P_{dc} decays down to 0.105 pu for 6 cycles fault duration and 0.085 pu for 12 cycles fault duration. The power goes to nominal value within 3 cycles after the fault is cleared during both cycles as shown in Figure 6.3 (g). The system input power factor is affected and drops down to almost 0.1 during both fault durations before returning to nominal value within 8 cycles of fault removal. The system response during 6 cycles and 12 cycles are different in some parameters during TLG fault. All phases experience disturbances and the system parameters recover within 8 cycles after the fault is cleared.

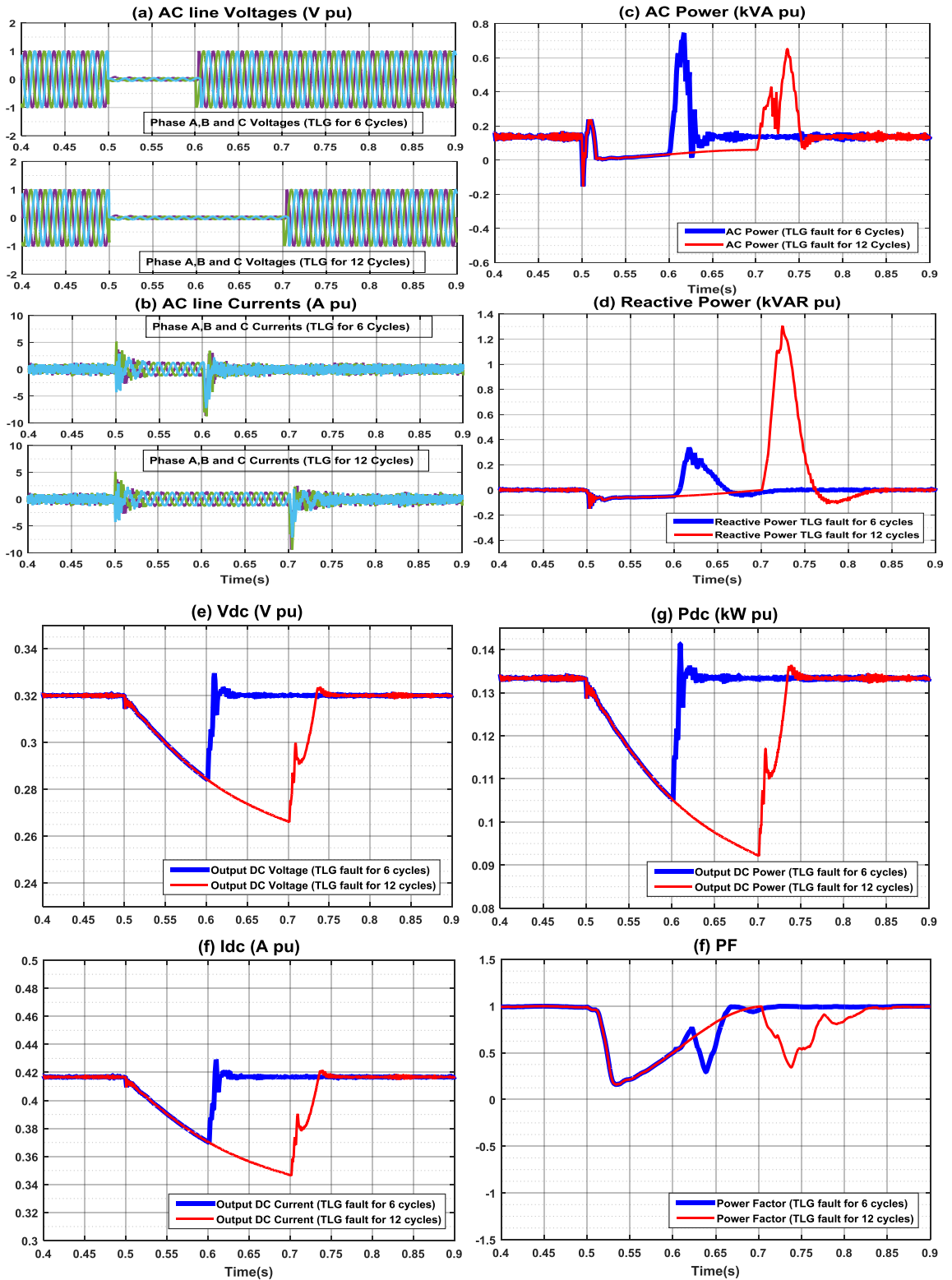


Figure 6.3 (a-f): System response to TLG fault introduced for 6 cycles and 12 cycles with IGBT based rectifier.

6.3 Three-Phase AC-DC Matrix Converter

Momentary interruptions occurs when any input phase voltages goes below 10% of the magnitude between 0.5 cycles to 3 s. SLG, DLG and TLG faults are simulated in MATLAB and the system response and recovery is noted. For implementation, starting conditions are set for active power of 0.13 pu, the DC output current I_{dc} and DC output voltage V_{dc} are fixed at 1 pu. The analysis is conducted for AC voltages and currents (V_{abc} and I_{abc}), active and reactive power (P and Q), output DC voltage (V_{dc}) and output DC current (I_{dc}) as well as power factor.

6.3.1 Single-Line-to-Ground Fault

A SLG fault is introduced in phase A at the AC input at 0.5 s for 6 cycles. Figure 6.4 (a-h) represents the AC voltages, AC currents for all three phases, system active and reactive power (P and Q), DC output current (I_{dc}) and DC output voltage (V_{dc}) as well as power factor response during this fault for 6 and 12 cycles. The momentary interruption results in the AC voltages for all phases to reduce down to about 5.5% of the rated value and high currents are observed that oscillates until the fault is cleared. The system behaves as a shock absorber for protection under this fault and the voltages and currents are seen as more stable with minimum oscillations.

AC power at start of the fault responds with a very high transient overshoot and decays in oscillations until the fault is removed for 6 cycles. Power shows negative transient response before returning to nominal value of 0.13 pu within 3 cycles. As there

is no control over reactive power for the system with MC based rectifier, reactive power (Q) is zero until the fault is introduced. When the fault occurs, Q shoots to 50 pu as there is no reactive power control designed for this system. As soon as the fault is removed after 6 cycles (at 0.6 s), Q value goes back to zero within 3 cycles as shown in Figure 6.4 (d).

At the DC side V_{dc} decays down from 0.32 pu to 0.15 pu (17% reduction) before returning back to nominal value within 3 cycles after fault removal. No overshoot response is seen in V_{dc} and P_{dc} . I_{dc} goes down to 0.2 pu from 0.4 pu during the fault and recovers back to normal value within 3 cycles after the fault is removed. P_{dc} decays down to 0.06 pu during the fault and ramps back to nominal value after the fault is removed within 3 cycles. Power factor of the system is affected and drops down to zero during fault before returning to nominal value within 3 cycles of fault removal. All parameters recover back to nominal values within 3 cycles of fault removal.

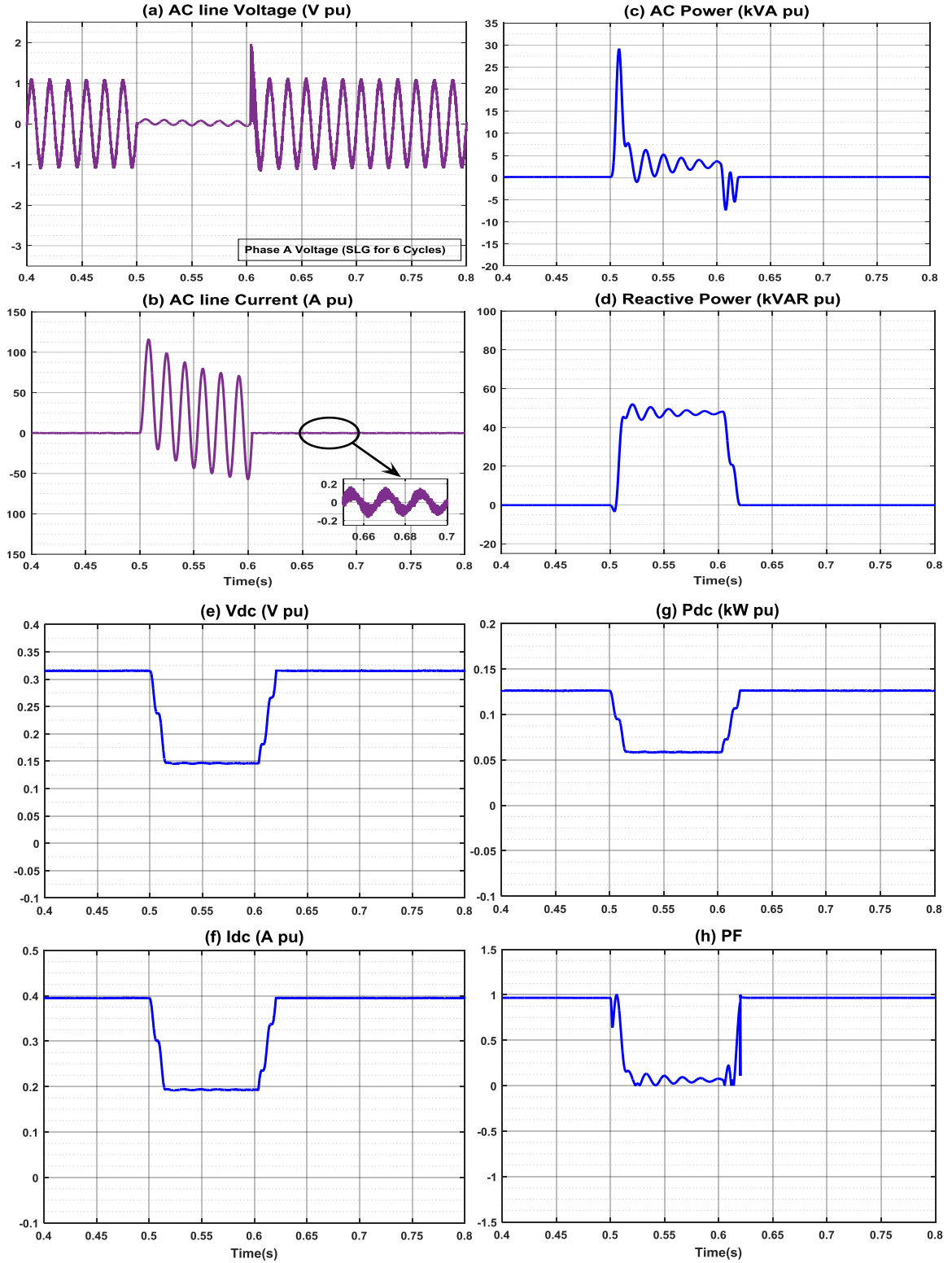


Figure 6.4 (a-h): System response to SLG fault introduced for 6 cycles with MC based rectifier.

6.3.2 Double-Line-to-Ground Fault

A DLG fault is introduced in phases A and B at the AC input side at 0.5 s for 6 cycles. Figure 6.5 (a-h) represents the AC voltages, AC currents for all three phases, system active and reactive power, DC current and voltage (I_{dc} and V_{dc}) as well as power factor response during this fault for 6 cycles. A momentary interruption results in the AC voltages for phases A and B to reduce down to about 5.5% of the rated value and high currents are observed that oscillates until the fault is cleared.

AC power at start of the fault responds with very high transient overshoot and decays in oscillations until the fault is removed for 6 cycles. Power shows negative transient response before returning to nominal value of 0.13 pu within 3 cycles. As there is no control over reactive power for the system with MC based rectifier, reactive power (Q) is zero until the fault is introduced. When the fault occurs, Q overshoots to 100 pu as there is no control over the reactive power. As soon as the fault is removed after 6 cycles (at 0.6 s), Q value goes back to zero within 3 cycles.

At the DC side, for 6 cycles and 12 cycles fault durations, V_{dc} decays down from 0.32 pu to -0.01 pu before returning back to nominal value within 3 cycles after fault removal. No overshoot response is observed in DC output voltage V_{dc} and power P_{dc} . However, the system does not try to recover back to its nominal value until after the fault is removed. I_{dc} shows a similar response as V_{dc} in Figure 6.5 (f), decaying from 0.4pu to -0.01 pu before recovering to nominal value within 3 cycles of removing the fault. P_{dc} also decays down to 0 pu for the duration of the fault and ramps back to nominal value

after the fault is removed within 3 cycles. Power factor of the system is affected and drops down to zero during the fault before returning to nominal value within 3 cycles of fault removal. All parameters recover back to nominal values within 3 cycles of fault removal in both fault durations.

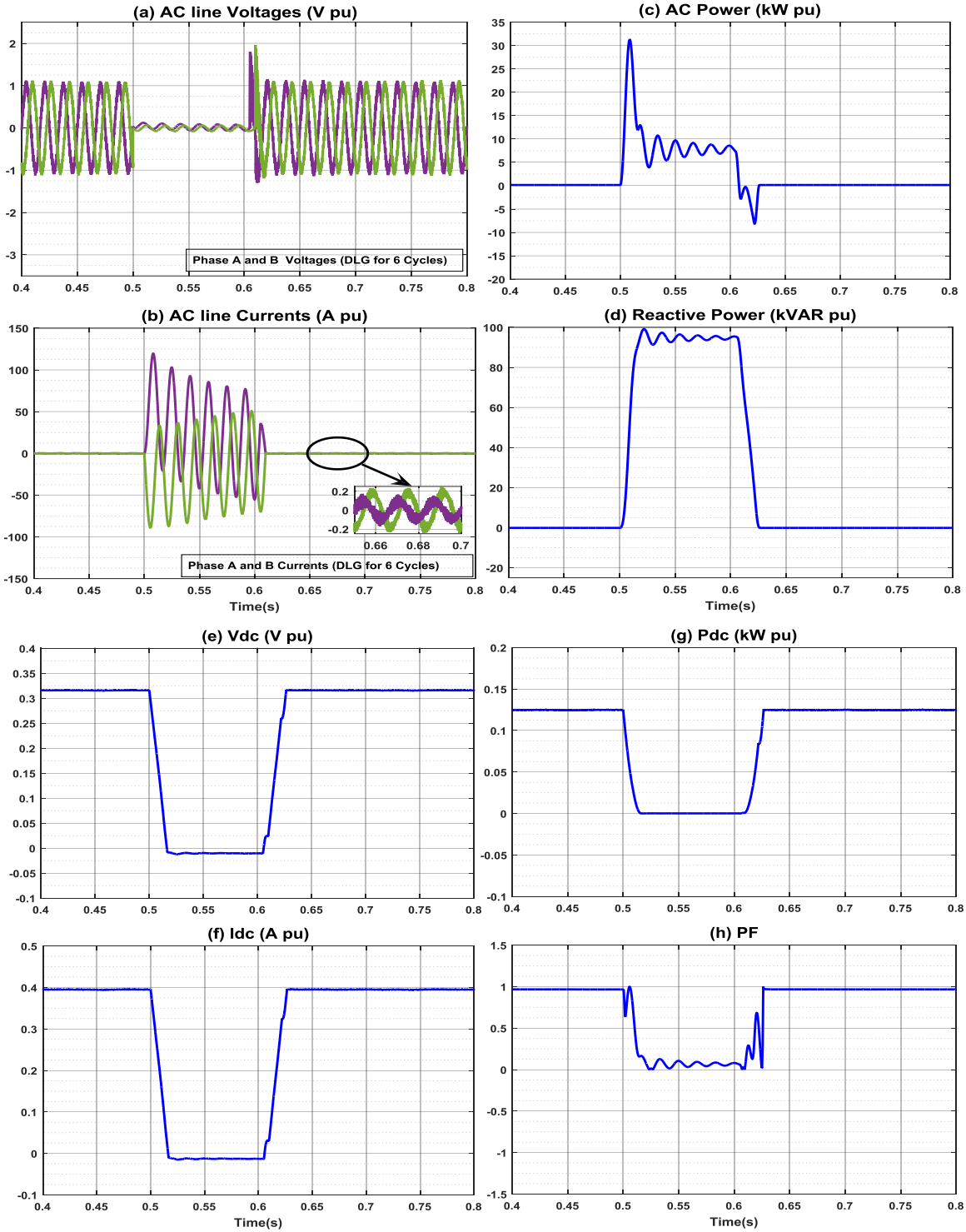


Figure 6.5 (a-h): System response to DLG fault introduced for 6 cycles with MC based rectifier.

6.3.3 Triple-Line-to-Ground Fault

A TLG fault is introduced in all phases A, B and C at the AC input at 0.5 s for 6 cycles and 12 cycles respectively. Figure 6.6 (a-h) represents the AC voltages, AC currents for all three phases, system active and reactive power, DC current and voltage (I_{dc} and V_{dc}) as well as power factor (PF) response during this fault for the two durations. A momentary interruption results in the AC voltages for all phases to reduce down to about 5.5% of the rated value and high currents are observed that oscillates until the fault is cleared.

AC power at start of the fault responds with very high transient overshoot and decays while oscillating until the fault is removed after 6 cycles. Power shows negative transient response before returning to nominal value of 0.13 pu within 3 cycles. Fault introduced for 12 cycles shows a similar response until the fault removal at 0.7 s where the power transient response is as seen in Figure 6.6 (c) and recovers back to nominal value within 3 cycles. As there is no control over reactive power for the system with MC based rectifier, reactive power (Q) is zero until the fault is introduced. When the fault occurs, Q shoots to 100 pu as there is no control over the reactive power. As soon as the fault is removed after 6 cycles (at 0.6 s), Q value goes back to zero within 3 cycles. During 12 cycles of fault, Q remains at 100 pu and comes back to zero after the fault is removed within 3 cycles.

At the DC side, for 6 cycles and 12 cycles fault durations, V_{dc} decays down from 1 pu to 0 pu before returning back to nominal value within 3 cycles after fault removal. No

overshoot response is seen in DC output voltage and power (V_{dc} and P_{dc}). I_{dc} goes down to 0 pu after the fault is introduced for both durations and recovers to nominal value within 3 cycles of fault removal. In fault durations of 6 cycles and 12 cycles, P_{dc} decays also dips down to 0 pu for each duration cycle. The power ramps back to nominal value after the fault is removed within 3 cycles. Power factor of the system is affected and drops down to zero during both fault durations before returning to nominal value within 3 cycles of fault removal. System with MC shows the response to TLG fault in two duration cycles. Except power factor, the TLG fault response is similar to DLG fault suggesting the system with MC based rectifiers can be controlled to respond well to all phases experiencing fault conditions. All parameters recover back to nominal values within 3 cycles of fault removal in both fault durations.

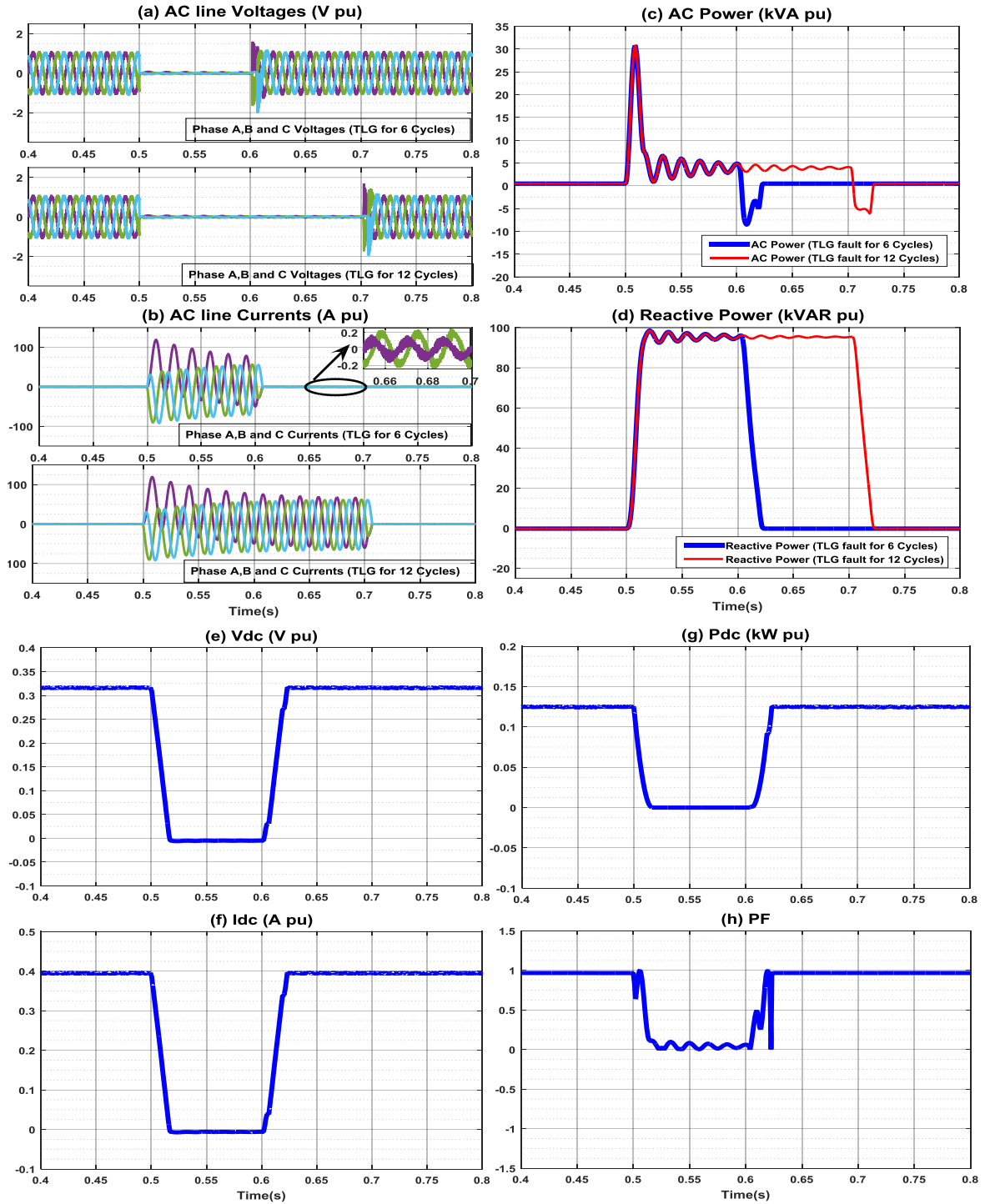


Figure 6.6 (a-h): System response to TLG fault introduced for 6 cycles and 12 cycles with

MC based rectifier.

Chapter 7 Conclusion and Future Work

7.1 Conclusion

With the rising demand of EVs, an increase in the number of EVs charging stations is expected in the near future. EVs charge by using rectifiers that convert AC into DC. This conversion process produces distortion in currents and voltages that are reflected in the distribution system. Major impacts on the voltage and current of the power grid are expected. In order to construct improved charging stations that reduce negative impacts on the power grid and improve economic efficiency, the harmful effects of EV charging stations on the power grid need to be studied and viable solutions must be proposed.

The major contributions of this thesis are;

- Design of a grid connected 3-phase IGBT based rectifier with unity PF feedback control loop that can be used in Level 2 EV chargers, simulated in MATLAB Simulink and studied the system performance responses under steady, dynamic states and fault conditions.
- Development of a detailed model of a three-phase, two-level, single ended bidirectional MC based rectifier which can be used in Level 2 EV charging stations offering attractive benefit of V2G capability.

- Generation of gate pulses through implementation of SVPWM technique in order to minimize switching losses, reducing the THD (<4%), and offer better use of DC bus in comparison with conventional PWM techniques.
- Design and implementation of the three-phase MC based rectifier with connection to the grid in MATLAB Simulink to understand the performance response of the designed rectifier under steady state, dynamic state and fault conditions.

The simulation results for the IGBT based rectifier model show that the system active and reactive power can be controlled independently using vector control. The system response is of the order **0.1 s**, and is well controlled under steady state and dynamic conditions. During dynamic testing, where a step change is applied to the DC output voltage (V_{dc}), DC output power (P_{dc}) and reactive power (Q), shows that the system response is fast. Change in reactive power shows no response in active power confirming the decoupled operation of the two power components. The input PF is maintained at unity under these conditions.

Under fault conditions, the system behavior is tested during 6 and 12 cycle faults respectively. System responds well under SLG faults, with slight changes in active and reactive power as they are well controlled. Oscillations occurs in DC output voltage (V_{dc}), DC output current (I_{dc}) and DC output power (P_{dc}) during SLG and DLG faults which recovers quickly within **3 cycles and 4 cycles** respectively after the fault is cleared. Power factor is affected more during SLG fault compared to DLG and TLG fault conditions.

Under TLG fault, less oscillations in the output voltage, current and power are noticed owing to the fact that the system is acting as a shock absorber to minimize the effect of this fault on the system performance. However, longer decay times occur for these parameters when TLG fault is applied for 12 cycles as compared to 6 cycles suggesting a detrimental effect on the system when this fault is introduced for longer period. The system recovers within **8 cycles** (maximum) for all of the fault types described above.

On the other hand, using three-phase MC based rectifier model, the simulation results show a faster response for the system of the order of **0.02 s** in comparison. Under steady state, the system response is fast and the V2G capability delivers unity power factor indicating minimum power losses in the system. The harmonic spectrum showed less than 4% THD showing a promising response of MC in improving the THD without the need of bulky filter requirements, reducing the overall cost and bulk of the system. Dynamic response is fast for the system and step changes are applied to output DC voltage (V_{dc}) and current (I_{dc}) to show full voltage and current range that is available. The wide range of output current and voltage availability would benefit in reducing the overall system size as one converter can perform the voltage step-up or step-down depending on the system power flow without the need for separate DC-DC converters as used in conventional EV chargers. The system confirms that changing the modulation index in the system affects the DC output voltage (V_{dc}). The change in output voltage and current shows the system is robust and can manage changes in battery set-points without detrimental effects on the system. Unity PF is achieved for the system

considering the input current from the grid is in phase with the input voltage through reduced modulation function matrices used in the algorithm for AC-DC matrix converter. A reduced PF resulting from a change in output current can be improved using PFC circuit in the system. The inherent bi-directionality feature of MC is tested and confirmed under dynamic response and is recognized as one of the key benefit of using MC in EV charger topology without much system complexity.

Under fault conditions, the system is introduced to SLG, DLG and TLG faults of 6 and 12 cycles duration respectively. Under all these faults, initial high AC currents occur and the system shows a high transient response in the active power as well as a high reactive power response with some decaying oscillations as the system has no control over the active and reactive power. The PF for these faults goes to zero during the fault occurrence but recovers quickly, within **3 cycles**, after the fault is removed. The output voltage and power drops down with no oscillations during SLG fault showing good control of output voltage and power. During DLG and TLG fault conditions, output voltage and power is affected dropping below zero with no oscillations. The system response has no detrimental effects when the faults are introduced for longer periods (6-12 cycles).The system recovers within **3 cycles** (maximum) for all the three types of faults introduced in this system.

7.2 Future Work

This research work has covered some key knowledge of using MC in a rectifier configuration. This converter shows promising use in EV chargers as it offers V2G capability among many other benefits and needs further investigation.

For future research work,

- A feedback system can be introduced to improve voltage regulation in the system. Feedback controllers can also be used to control the active and reactive power of the system to reduce power losses in the system and maintain unity PF.
- A Power factor correction circuit can be implemented to maintain unity power factor with respect to output current.
- Passive/active input filters can be implemented for further realization of the system to improve THD of the system.
- Changing frequencies can be applied to systems using MCs in rectifiers that can be grid integrated with renewable energy sources like solar and wind farms.
- Soft switching can be employed in the PWM technique s reduce switching losses, improve overall system efficiency and reducing high voltage transient responses to protect the system.
- As this thesis work has considered the system with ideal switches and system parameters for simulation purposes, the system needs to consider power density of the system, efficiency, cost of the components, as well as battery at the load

with its full specification as used in EVs for further realization of the system in practical applications.

- Experimental work needs to be carried out to further validate the system responses to SLG, DLG and TLG fault conditions as well as other power line faults.
- Further validation of the overall system at the grid connection and the battery as the load can be carried out to improve and benefit commercial and residential charging stations by considering

References

- [1] H. Bai, C. Mi, *Transients of Modern Power Electronics*, Wiley, 2011.
- [2] N.A. Owen, O.R. Inderwildi, D.A. King, "The status of conventional world oil reserves - hype or cause for concern?," *Energy Policy*, vol.38, no.8, pp.4743-4749, 2010.
- [3] Iqbal Husain, *Electric and Hybrid Vehicles Design Fundamentals*, CRC Press, 2003.
- [4] M. Abul Masrur, David Wenzhong Gao, Chris Mi, *Hybrid Electric Vehicles Principles and Applications wit Practical Prospectives*, Wiley, 2011.
- [5] Hiott, Andrea, *Thinking Small: The Long, Strange Trip of the Volkswagen Beetle*, Random House LLC., 2012
- [6] B. Black, *Nature and the environment in twentieth-century American life*. Westport, Conn. Greenwood Press, 2006.
- [7] J. I.Leon, L. G. Franquelo, J. Rodriguez, B. Wu, " The Essential Role and the Continuous Evolution of Modulation Techniques for Voltage Source Inverters in Past, Present and Future Power Electronics," *IEEE Transaction on Industrial Electronics*, vol.PP, no.99, 2016.
- [8] N. Howe, *Owning Model S: The Definitive Guide to Buying and Owning the Tesla Model S.*, 2014
- [9] *SAE Electric Vehicle and Plug-in Hybrid Electric Vehicle Conductive Charge Coupler*, SAE Standard J1772, Jan. 2010.
- [10] M. C. Falvo, D. Sbordone, I. S. Bayram, M. Devetsikiotis, "EV Charging Stations and Modes: International Standards," *International Symposium on Power Electronics, Electrical Drives, Automation and Motion*, pp. 1134-1139, 2014.
- [11] R.Antao, T. Goncalves, R.E. Martins, "Modular Design of DC-DC Converters for EV battery fast-charging," *International Conference on Renewable Energies and Power Quality (ICREPQ'13)*, 2013.
- [12] N. Mohan, T. Undeland and W. Robbins, *Power electronics*. New York: Wiley, 1995.
- [13] S.W. Hadley, "Evaluating the impact of Plug-in Hybrid Electric Vehicles on regional electricity supplies," *Bulk Power System Dynamics and Control - VII. Revitalizing Operational Reliability, 2007 iREP Symposium*, pp. 1-12, 2007.
- [14] M. Yilmaz and P. Krein, "Review of Battery Charger Topologies, Charging Power Levels, and Infrastructure for Plug-In Electric and Hybrid Vehicles", *IEEE Transactions on Power Electronics*, vol. 28, no. 5, pp. 2151-2169, 2013.
- [15] V. Monteiro, J. G. Pinto, B. Exposto, H. Goncalves, J. C. Ferreira, C. Couto, J. L. Afonso, C. Algoritmi, "Assessment of a battery charger for electric vehicles with reactive power control," *IECON 2012 - 38th Annual Conference on IEEE Industrial Electronics Society*, pp. 5142-5147, 2012
- [16] R.J.Rei, F.J.Soaes, P.M.R.Almeida, J.A.P. Lopes, "Grid Interactive Charging Control for Plug-in Electric Vehicles," *13th International IEEE Conference on Intelligent Transportation Systems* pp.386-391, 2010.

- [17] K.Clement, E.Haesen, J.Driesen, "Coordinated charging of multiple plug-in hybrid electric vehicles in residential distribution grids," *PSCE Power Systems Conference and Exposition*, pp. 1-7, 2009.
- [18] V. Monteiro, J. C. Ferreira, J. G. Pinto, B. Exposto, D. Pedrosa, J. L. Afonso, "Comparison of Charging Systems for Electric Vehicles and Their Impact on Electrical Grid," *Annual Seminar on Automation, Industrial Electronics and Instrumentation 2012 - SAAEI'12*, pp. 440-445, 2012.
- [19] Z.Yang, P.C.Sen, "Recent developments in high power factor switch mode converters," *IEEE Canadian Conference on Electrical and Computer Engineering*, vol. 2, pp. 477-480, 1998.
- [20] J. A. Orr, A. E. Emanuel, D. J. Pileggi, "Current Harmonics, Voltage Distortion, and Powers Associated with Electric Vehicle Battery Chargers Distributed on the Residential Power System," *IEEE Trans. on Industry Applications*, vol. IA-20, no. 4, 1984.
- [21] H. S. Krishnamoorthy, P. Garg, P.. N. Enjeti, "A Matrix Converter-Based Topology For High Power Electric Vehicle Battery Charging and V2G Application," *IECON 2012 - 38th Annual Conference on IEEE Industrial Electronics Society*, pp. 2866-2871, 2012.
- [22] R. Liu, L. Dow, E. Liu, "A Survey of PEV Impacts on Electric Utilities," *IEEE PES Innovative Smart Grid Technologies Conference*, pp. 1-8, 2011.
- [23] T. Soeiro, T. Friedli, J. W. Kolar, "Three-phase high power factor mains interface concepts for Electric Vehicle battery charging systems.," *Applied Power Electronics Conference and Exposition (APEC) 2012 Twenty-Seventh Annual IEEE*, pp.2603-2610, 2012.
- [24] M. Kang, P. N. Enjeti, I. J. Pitel, "Analysis and design of electronic transformers for electric power distribution system," *Power Electronics, IEEE Transactions*, vol. 14, no. 6, pp. 1133-1141, 1999.
- [25] D. Chapman, D. James, C.J. Tuck, "A high density 48 V 200 A rectifier with power factor correction-an engineering overview," *Telecommunications Energy Conference, INTELEC '93 15th International*, vol. 1, pp. 118-125, 1993.
- [26] D. G. Holmes, T. A. Lipo, "Implementation of a Controlled Rectifier Using AC-AC Matrix Converter Theory," *IEEE Transactions on Power Electronics*, vol. 7, no. 1, pp. 240-250, 1992.
- [27] R. Garcia-Gil, J. M. Espi, E. J. Dede, E. Maset, "An All-Digital Controlled AC-DC Matrix Converter with High-Frequency Isolation and Power Factor Correction," *2004 IEEE International Symposium on Industrial Electronics*, vol. 2, pp. 1075-1080, 2004.
- [28] E. Sanchis-Kilers, J.A. Carrasco, R. de la Calle, J. M. Espi J.B. EJE, "High-Frequency Bi-directional Three-Phase Rectifier With Power Factor Correction," *IEEE*, pp. 1303-1308, 2001.
- [29] N. Li and M. Huang, "Comparison among Chargers of Electric Vehicle Based on Different Rectifiers," in *North China Electric Power*, No. 1, 2011.
- [30] *Durham Strategic Energy Alliance Electric Vehicle Charging Station Demonstration Project Final Report*, Sponsored by LDC Tomorrow Fund and Ontario Power Generation, 2012
- [31] B. Francois, *Hybrid Vehicles from components to system*, Editions Technip, 2013.
- [32] W. Shepard, L. Zhang, *Power Converter Circuits*, Marcel Dekker, Inc., 2004.
- [33] S.Varghese, S. George, "Analysis of AC-DC Converter Based on Power Factor and THD," *International Journal of Emerging Technology and Advanced Engineering*, vol. 3, no. 2, pp. 350-356, 2013.
- [34] Zahra Ameli Ali Akbar Motie Birjandi, "Three Phase Controlled Rectifier Study in Terms of firing angle variations," *ACEEE Int. J. on Electrical and Power Engineering*, vol. 03, no. 02, pp. 25-28, 2012.
- [35] Muhammad H. Rashid (ed), *Power Electronics Handbook: Devices, Circuits, and Applications, Third Edition*, Butterworth-Heinemann, 2011.

- [36] R. Krishnan, F. B. Marian, P. Kazmierkowski, *CONTROL IN POWER ELECTRONICS. Selected Problems*. California, USA, Academic Press, Elsevier Science, 2002.
- [37] L. P. Gyugyi, *Static Power Chargers, Theory, Performance and Application*, John Wiley & Son Inc, 1976.
- [38] A. Hasim, M. Hamzah, M. Omar R. Baharom, "A New Single-Phase Controlled Rectifier Using Single-Phase Matrix Converter," *IEEE International Power and Energy Conference*, pp. 453-458, 2006.
- [39] M. K. Hamzah, R. Baharom, N. V. Dahlan S. Z. Mohammad Noor, "A New Single-Phase Inverter with Bidirectional Capabilities Using Single-Phase Matrix Converter," *IEEE Power Electronics Specialists Conferenc*, pp. 464-470, 2007.
- [40] S. Z. M. Noor, M. K. Hamzah, A. F. Abidin, "Modelling and Simulation of a DC Chopper Using Single Phase Matrix Converter Topology," in *IEEE Sixth International Conference PEDS*, 2005.
- [41] P.W. Wheeler, J. Rodrguez, J.C. Clare, L. Empringham, and A.Weinstein, "PWM-rectifier/voltage-source inverter without dc -link components for induction motor drive," *Matrix converters: a technology review*, vol. 49, pp. 276-288, 2002.
- [42] P. Nielsen, F. Blaabjerg, J.K. Pedersen, "New protection issues of a matrix converter: design considerations for adjustable-speed drives," *IEEE Trans. Ind. Applic.*, vol. 35, pp. 1150-1161, 1999.
- [43] M. Venturini, A. Alesina, "Solid-state conversion: A fourier analysis approach to generalized transformer synthesis," *IEEE Transactions on Circuits and Systems*, vol. CAS-28, no. 4, pp. 319-330, 1981.
- [44] M. Venturini, A. Alesina, "Analysis and design of optimum-amplitude nine-switch direct AC-AC converters," *IEEE Transactions on Power Electronics*, vol. 4, no. 1, pp. 101-112, 1989.
- [45] D. Borojevic, L. Huber, "Space Vector Modulated Three-phase to Three-phase Matrix Converter with Input Power Factor Correction," *IEEE TRANSACTIONS ON INDUSTRY APPLICATIONS*, vol. 31, no. 6, pp. 1234-1246, 1995.
- [46] P. Nielsen, F. Blaabjerg, J.K. Pedersen, "New protection issues of a matrix converter: design considerations for adjustable-speed drives," *IEEE Trans. Ind. Applic.*, vol. 35, pp. 1150-1161, 1999.
- [47] J.W. Kolar, M. Baumann, F. Schafmeister, H. Ed, "Novel three-phase AC-DC-AC sparse matrix converter," *Proc. Conf. Rec. IEEE APEC*, vol. 2, pp. 777-791, 2002.
- [48] C. Klumipner, F. Blaabjerg, , "A new generalized two-stage direct power conversion topology to independetly supply multiple ac loads fromi mutltiple power grids with adjustable power loading," in *Proc. of PESC'04*, 2004.
- [49] K. Shinohara, R. Ueda, Y. Minari, "PWM-rectifier/voltage-source inverter without dc -link components for induction motor drive," *IEE Proceedings-B - Electric power applications*, vol. 140, pp. 363-368, 1993..
- [50] K. Shinohara, O. Tarumi, Z. Fu, M. Muroya, K. limori, "New current-controlled PWM rectifier-voltage source inverter without DC link components," *Proc. Conf. Rec. PCC*, vol. 2, pp. 783-786, 1997.
- [51] K. Shinohara, K. limori, H. Sako M. Muroya, "Four-step commutation strategy of PWM rectifier of converter circuit without DC link components for induction motor drives," *Proc. Conf Rec. IEEE IEMDC*, pp. 770-772, 2001.
- [52] L. Huber, D. Borojevic, "Space vector modulated three-phase to three-phase matrix converter with input power factor correction," *IEEE Trans. Ind. Applic.*, vol. 31, pp. 1234-1246, 1995.
- [53] L. Wei , T.A. Lipo, H. Chan, "Matrix converter topologies with reduced number of switches," *33d Proc. Conf. Rec IEEE PESC*, 2002.

- [54] P. D. Ziogas, S. I. Khan, M. H. Rashid, "Analysis and design of forced commutated cycloconverter structures with improved transfer characteristics," *IEEE Trans. Ind. Electron*, vol. IE-33, pp. 271-280, Aug 1986.
- [55] L. Huber, D. Borojevic, N. Burany, "Voltage space vector based PWM control of forced commutated cycloconvertors," *Proc. IEEE IECON'89*, pp. 106-111, 1989.
- [56] M. Venturini, A. Alesina, "Intrinsic amplitude limits and optimum design of 9-switches direct PWM AC-AC converters," *Proc. IEEE PESC'88*, pp. 1284-1291, 1988.
- [57] G. Roy, L. Duguay, S. Manias, G. E. April, "Asynchronous operation of cycloconverter with improved voltage gain by employing a scalar control algorithm," *Conf. Rec. IEEE-IAS Annu. Meeting*, pp. 889-898, 1987.
- [58] G. Roy, G. E. April, "Cycloconverter operation under a new scalar control algorithm," *Proc. IEEE PESC'89*, pp. 368-375, 1989.
- [59] J.Karpagam, A.N. Kumar, V.K. Chinnaiyan, "Comparison of Modulation Techniques for Matrix Converter," *IACSIT International Journal of Engineering and Technology*, vol. 2, no. 2, pp. 189-195, 2010.
- [60] M. Milosevic, "Decoupling control of d and q current components in three-phase voltage source inverter," pp. 1-11.
- [61] Tremblay, O., Dessaint, L.-A. "Experimental Validation of a Battery Dynamic Model for EV Applications." *World Electric Vehicle Journal*. Vol. 3 - ISSN 2032-6653 - © 2009 AVERE, EVS24 Stavanger, Norway, May 13 - 16, 2009.
- [62] A. Lindemann, "A new IGBT with reverse blocking capability," *Proc. Conf Rec. EPE*, 2001.
- [63] K. Shinohara, & R. Ueda Y. Minari, "PWM-rectifier/voltage-source inverter without dc-link components for induction motor drive," *IEEE Proceedings-B - Electric power applications*, vol. 140, pp. 363-368, 1993.
- [64] K. Shinohara, K. Iimori, and H. Sako M. Muroya, "Four-step commutation strategy of PWM rectifier of converter circuit without DC link components for induction motor drives," *Proc. Con. Rec. IEEE IEMDC*, pp. 770-772, 2001.
- [65] T.A. Lipo, and H. Chan L. Wei, "Matrix converter topologies with reduced number of switches," *33rd Proc. Conf. Rec IEEE PESC*, p. 7, 2002.
- [66] Marian P. Kazmierkowski Mariusz Cichowlas, "Comparison of current control techniques for PWM rectifiers," *IEEE*, pp. 1259-1263, 2002.
- [67] M.Yilmaz, P.T. Krein, "Review of benefits and challenges of vehicle-to-grid Technology," *ECCE IEEE*, pp. 3082-3089, 2012.
- [68] B.K.Sachin, S.Madhu, G.K. Vijay, K. N. Sunil, "Simulation of buck or boost rectifier using single phase matrix converter with reduced switch count," *International Conference on PACE*, pp.361-365,2015.

Appendix A

Table A: Parameters of the system model [30].

System Parameters	Rating
System power	15kVA
Frequency	60 Hz
Transformer Primary voltage	600 V
Transformer Secondary voltage	120 V
DC Capacitor	5000 μ F
Line Inductance	20 μ H
Battery charging Current	40A
Battery Charging Voltage	48 V
Battery Power	2 kW
Simulation Time Step	5 μ s

Appendix B

B.1 Per-Unit System Calculation

The system based on the two rectifier configurations modelled in this thesis is converted to per unit. These per unit conversion calculations are as follows:

Nominal three-phase apparent power of the AC network = $S_{base} = 15 \text{ kVA}$

Nominal peak phase voltage of the AC network = $V_{base} = \sqrt{\frac{2}{3}} V_{LL(RMS)}$

Where $V_{LL(RMS)}$ is the line to line RMS voltage.

$$V_{LL(RMS)} = 600 \text{ V}$$

$$V_{base} = 489.9 \text{ V}$$

Nominal peak phase current = $I_{base} = \frac{2}{3} \frac{S_{base}}{V_{base}} = 20.41 \text{ Amps}$

Base AC impedance = $Z_{base} = \frac{V_{base}}{I_{base}} = 24 \text{ } \Omega$

Base angular frequency = $\omega_{base} = 377 \text{ rad/sec}$

At the DC side, per unit calculations are achieved as follows:

Nominal base power of the DC network = $P_{dcbase} = 15 \text{ kW}$

Nominal base voltage of the DC network = $V_{dcbase} = 150 \text{ V}$

Base DC current = $I_{dcbase} = \frac{P_{dcbase}}{V_{dcbase}} = 100 \text{ Amps}$

B.2 Battery Model

The battery of the EV considered for the models designed in this thesis consider an ideal battery with no power losses, maximum efficiency with no internal capacitances, resistances and other components. However, in practical applications various battery characteristics needs to be considered. The detailed model of the lithium-ion battery model that can be adapted for the charger has a typical equivalent circuit as shown below in Figure B.1.

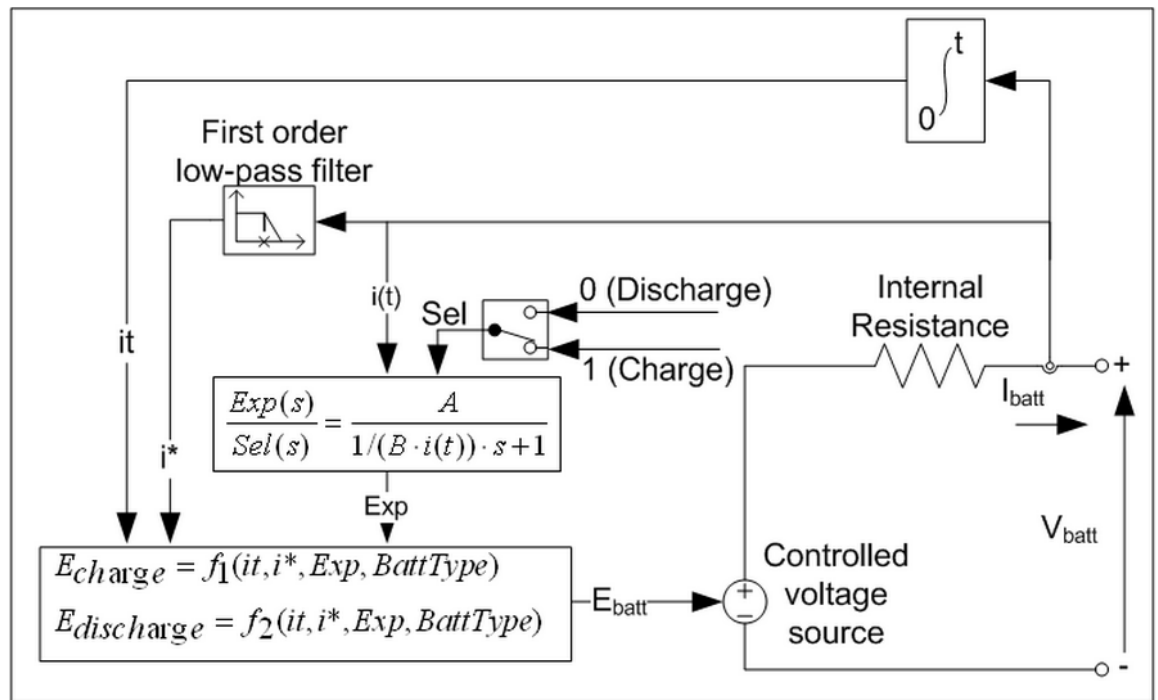


Figure B.1: Equivalent circuit of a battery [61].

Where,

E_{Batt} = Nonlinear voltage (V)

E_0 = Constant voltage (V)

Exp(s) = Exponential zone dynamics (V)

Sel(s) = Represents the battery mode. Sel(s) = 0 during battery discharge,

Sel(s) = 1 during battery charging.

K = Polarization constant (Ah⁻¹) or Polarization resistance (Ohms)

i* = Low frequency current dynamics (A)

i = Battery current (A)

it = Extracted capacity (Ah)

Q = Maximum battery capacity (Ah)

A = Exponential voltage (V)

B = Exponential capacity (Ah)⁻¹

Model for battery discharging (i* > 0) is represented by:

$$f_1(it, i^*, i) = E_0 - K \cdot \frac{Q}{Q-it} \cdot i^* - K \cdot \frac{Q}{Q-it} \cdot it + A \cdot \exp(-B \cdot it) \quad (\text{B.1})$$

Model for battery charging (i* < 0) is represented by:

$$f_2(it, i^*, i) = E_0 - K \cdot \frac{Q}{it+0.1 \cdot Q} \cdot i^* - K \cdot \frac{Q}{Q-it} \cdot it + A \cdot \exp(-B \cdot it) \quad (\text{B.2})$$

This equivalent circuit can be modified to suit different battery types based on their discharge characteristics. Typical charge characteristics of the Li-ion battery when the battery current is negative is shown in Figure B.2

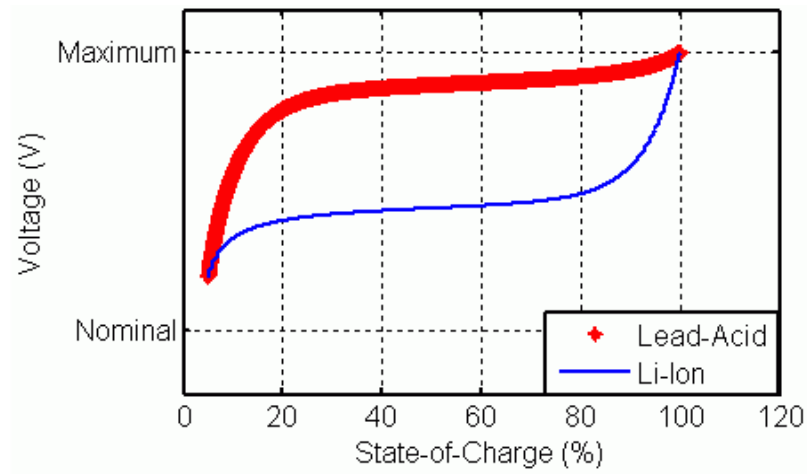


Figure B.2: Typical charge characteristics of a Li-ion battery [61].

The various parameters like nominal voltage (V), rated capacity (Ah), initial state-of-charge (%), maximum capacity (Ah), fully charged voltage (V), nominal discharge current (A), internal resistance, capacity (Ah) at nominal voltage and exponential zone [Voltage (V), Capacity (Ah)] are a few practical consideration that be considered for detailed battery modelling. The data sheets for the battery can be used to extract these parameters for the battery. This detailed modeling for the battery can be done in MATLAB Simulink software where the model is available in its library under some assumed considerations.